SHAFT CAPACITIES OF CLOSED END PILES UNDER LOAD REVERSALS IN SAND

RICHARD HANKE

SHAFT CAPACITIES OF CLOSED END PILES UNDER LOAD REVERSALS IN SAND

by

©Richard Hanke

A thesis submitted to the
School of Graduate Studies
in partial fulfillment of the
requirements for the degree of
Master of Engineering

Faculty of Engineering and Applied Science
Memorial University of Newfoundland

November, 2001

St. John's Newfoundland Canada

Abstract

Since a wide range of opinions exists on axially loaded friction piles in sand a further evaluation and determination of the mechanisms involved with pile shaft capacities has been undertaken. A series of model pile load tests have been carried out in a geotechnical centrifuge to determine the effects of continuous load reversals. Axial compression and tension tests were performed on closed end pipe piles in a medium to dense dry silica sand. Both the end bearing and the total pile capacity were simultaneously measured to enable direct calculation of the shaft capacity. Pile loads and displacements were measured, as was the pile's inclination off vertical. With this information and the soil properties obtained within the laboratory, back calculations were performed using various methods to theoretically determine the pile shaft capacities. The theoretical values were then compared with the pile model data at prototype scale. This comparison has revealed the lack of reliability of design procedures of full displacement-type friction piles in sand and has yielded recommendations for the further experimental testing of pile models, which may ultimately lead to recommendations to existing design guidelines.

The study demonstrated that pile shaft capacities in non-cohesive soils can be both underestimated and dangerously overestimated by following conventional analytical design procedures. Pile inclination was determined to have a great affect on shaft capacity. Furthermore, the mobilization of pile end bearing was observed to have a distinct influence on compressive shaft resistances. Test results revealed a significant

reduction in tensile shaft resistance after the first few load cycles and a continued reduction with an increasing number of load reversals. Conversely, an increase in the total pile compressive resistance after several cycles was observed and thought to be due to granular crushing and material densification at the zone of end bearing. Similar to the end bearing response, the compressive shaft resistance initially reduced with load reversals but a trend reversal did become apparent. As the end bearing began to increase with continuous load cycling, so did the compressive shaft resistance. Focussing on an individual load cycle, the observed tensile shaft resistances were approximately equal to the compressive resistances before the end bearing was mobilized. Beyond this point the compressive shaft resistances increased to values of 2 to 3 times that of the corresponding tensile capacities. The increase in compressive shaft resistance was observed to be proportional to the simultaneous increase in end bearing capacity.

It is believed that a pressure bulb is generated at the pile base that in turn increases the lateral confining stresses along the lower portion of the pile shaft. The study has shown that as soon as the end bearing is activated, the formation of a pressure bulb can dominate the frictional behaviour of relatively short piles.

Acknowledgments

Financial support to assist in completion of this research was provided by the Natural Sciences and Engineering Research Council of Canada (NSERC).

I would like to acknowledge the assistance and guidance provided by my supervisors; Dr. Jack Clark and Dr. Ryan Phillips of C-CORE at the Memorial University of Newfoundland and Dr. Dieter Eigenbrod of Lakehead University. Acknowledgment must also be given to the technical support staff of the C-CORE Centrifuge Centre.

Table of Contents

List of Figures

List of Tables

Nomenclature

Greek Symbols

$\Delta\sigma'_{rd}$	Radial dilatant stress
δ, δ_{max}	Sand-steel interface friction angle
δ_{cv}	Sand-steel interface friction angle at constant volume
ϕ, ϕ'	Sand internal angle of friction
ϕ_{cv}	Sand internal angle of friction at constant volume
γ_{max}, γ_{min}	Unit weight
η	Dimensionless coefficient
μm	Micrometre (micron)
ν, ν_s	Dynamic viscosity
θ	Angular dimension (radians)
ρ, ρ_s	Material density
σ_3	Principal stress
σ'_h	Effective horizontal stress
σ_n	Normal stress
σ'_{rc}	Equalized radial effective stress
σ'_{rf}	Ultimate shaft stress
σ'_v, σ'_{vb},	Effective vertical stress
σ_{vm}, σ_{vp}	Vertical stress
υ, υ_m, υ_p	Velocity
ω	Angular velocity

Lower Case

a	Asperity depth
a,a_c,a_m,a_p	Acceleration
b	Pile diameter
cm	Centimeter
c_v, c_{vm}, c_{vp}	Coefficient of consolidation
d	Sand particle diameter
d, d_m, d_p	Drainage path length
d_{10}	Effective grain size
d_{50}	Mean grain size
e	Void ratio
f_s	Shaft skin stress (friction)
g	Gravity
h, h_i, h_m, h_p	Linear measure of depth
i, i_m, i_p	Hydraulic or pressure gradient
k, k_m, k_p	Coefficient of permeability

kN	Kilonewton
kPa	Kilopascal
m	Metre
mm	Millimeter
m_m, m_p	Mass
n	Stress ratio
psi	Pounds per square inch
q_c, q_{ca}, $\bar{q_c}$	CPT tip resistance
q_p	Pile unit toe stress
q_s	Shaft skin stress (friction)
rpm	Revolutions per minute
r, r_o	Radius
r_c	Height of failure zone above pile tip
r_o, r_u	Stress ratios
t_m, t_p	Time
z	Measure of depth

Upper Case

A	Dimensionless coefficient
A	Area
A_p	Area of pile tip
A_s	Pile shaft area
$ASTM$	American Society for Testing and Materials
B	Dimensionless coefficient
C	Dimensionless coefficient
C	Pile circumference
C_1, C_2	Dimensionless coefficients
$CLRL$	Critical level of repeated loading
CPT	Cone penetrometer test
CNS	Constant normal stiffness
C_u	Coefficient of uniformity
D	Dimension
DAS	Data acquisition system
D_b	Pile embedment length into dense strata
D_f	Pile embedment length
DC	Direct current
F_m, F_p	Force
F_v	Viscous force
F_{im}, F_{ip}	Inertial force
G	Shear modulus
G_{max}	Maximum shear modulus
G_s	Specific gravity of soil particles
$HDPE$	High density polyethylene

H_z	Hertz
I_D	Density index
L, L_m, L_p	Length
$LVDT$	Linearly variable displacement transformer
K	Permeability
K	Ratio of effective lateral to effective vertical earth pressure
K	Spring stiffness
K_a	Rankine active earth pressure coefficient
K_F	Force ratio
K_l	Area ratio
K_o	At rest lateral earth pressure coefficient
K_p	Rankine passive earth pressure coefficient
K_t	Time ratio
K_{Fv}	Viscous force ratio
K_{Fi}	Inertial force ratio
M	Mass
MPa	Megapascal
N	Acceleration level or model scale
N	Newton
N	Number of load cycles
N_q	Bearing capacity factor
N^*_q	Modified bearing capacity factor
OCR	Overconsolidation ratio
P	Pressure
P_{atm}	Atmospheric pressure
Q_d	Total axial load
Q_p	Total end bearing load
Q_s	Total shaft load
R	Pile radius
R^*	Modified pile radius
R_t	Centrifuge radius to top of model
R_e	Effective radius
R_{cla}	Pile centreline average roughness
SPT	Standard penetration test
T	Time
T_v	Terzaghi's dimensionless time coefficient
V	Velocity
V	Volt

CHAPTER 1

Introduction

1.1 Background

Piles are foundations intended to transmit loads through an upper level of weaker soil to more suitable soil or rock at a greater depth that can accommodate the load. Piles resist axial loads through pile shaft friction and/or end bearing, while some loading conditions may require these deep foundation types to resist uplift forces.

Since a wide range of opinions exist on the design of pile foundations in cohesionless soil, further evaluation of all aspects of pile design are constantly being reviewed and revised. The theoretical and technological progress of pile capacity analysis has led to conflicting view points and very wide discrepancies with respect to design procedures. The refining state of pile design has led to a lack of standardization between not only design procedures but also with sampling and test procedures giving the soil properties that govern the foundation design.

For a pile in a noncohesive soil body the compressive resistance is considered to be equal to the sum of the base resistance and shaft resistance. The base resistance is the product of the base area and the ultimate compressive resistance of the soil beneath the pile tip.

The shaft resistance is considered to be the product of the pile shaft contact area and the average ultimate shear resistance per unit area of the soil-pile interface. Some controversy exists in determining the ultimate soil resistances, both for end bearing and for side shear (ARGEMA, 1992). Although, it is generally believed that as a pile is loaded (Craig, 1997), initially the upper shaft of the pile carries the applied load and as the load is increased so does the depth of the mobilized skin friction, which is followed by activation of end bearing resistance. At failure it is also believed that the proportion of the load being carried by the pile shaft may reduce slightly due to plastic flow of the soil around the pile tip (Kraft, 1991; De Nicola and Randolph, 1993; Craig, 1997). Conversely, some researchers have reported a pressure or stress bulb generated at the pile toe, that once the end bearing is mobilized, curls upward around the pile shaft and is hypothesized to increase the lateral stresses acting along the pile shaft (Kezdi, 1964).

The tensile resistance of piles in noncohesive soil is generally thought and observed to be less than the shaft resistance in the compressive direction. It is believed that the difference between the two values is due in part to the fact that a downward movement of the pile increases the confinement pressure whereas an upward movement decreases it (Terzaghi and Peck, 1967). The rotation of the principal stress axis can also contribute to this phenomena (Symes *et al.* 1984). As noted earlier, interaction of the pile end bearing and the generation of a stress bulb is also believed to influence the compressive pile shaft resistance. It is hypothesized that as the pile end bearing is mobilized a pressure bulb is generated which increases the lateral confining stresses acting along the pile shaft. The

absence of a pressure bulb during upward displacements (tension) would therefore decrease the lateral stresses acting along the pile shaft and explain why tensile shaft resistances are observed to be consistently less than the associated compressive shaft resistance.

In a cohesionless soil, the shaft resistance of piles is known to degrade with time, either during one-way cyclic loading or load reversals (Poulos and Davis, 1980; Poulos and Chan, 1986). Many parameters are known to influence the magnitude and rate of shaft capacity reduction. The degree of influence and interaction of the relevant parameters is difficult to quantify and is an area of continued research.

1.2 Purpose

The purpose of this study is to investigate the mechanisms involved with pile shaft resistance in a cohesionless soil and the effect of continuous load reversals. The test data from both full-scale field tests and 1*g* laboratory model tests have yielded insight into pile shaft frictional behaviour, even though both methods have limitations. Full-scale field tests of instrumented piles are very costly and due to the time involved with installation and loading a comprehensive test program can not always be implemented. Furthermore, continuous profiles of interaction between end bearing and shaft capacities are difficult if not impossible to obtain. The laboratory tests of pile models within an open testpit at 1*g* have scaling limitations and tests can only be performed at relatively low stress levels. By using a geotechnical centrifuge to model and test pipe piles in sand, additional insight

into axial pile response at high stress levels has been obtained. The scaling laws associated with a centrifuge, as described in Chapter 3, permit a pile model of a convenient size (*1/N*) to simulate the full-scale prototype pile within the field. The centrifuge pile model can be tested at high stress levels representative of the full-scale prototype tests over several load reversals within a short time frame. Pile end bearing and shaft resistances can be recorded continuously with both time and displacement, something difficult to obtain in the field.

The objectives of this study were to analyze the axial capacity of piles in compression and tension and to evaluate the degradation of pile shaft resistance with increasing load reversals. Steps and tasks undertaken to achieve the goal of the study were:

(1) develop a pile model with instrumentation and loading mechanism for centrifuge testing,

(2) determine the effects of load reversals on shaft capacities,

(3) observe the influence of end bearing on shaft resistance,

(4) assess the effects of particle crushing and orientation on pile shaft capacity, and

(5) compile conclusions and recommendations regarding the effects of axial load reversals on stress conditions along the sand-steel interface of a close ended short pipe pile in sand.

The study has given insight into the behaviour of pile shaft resistance during load reversals and the effects of pile end bearing on compressive shaft resistance. The

centrifuge test data complements the data from other investigations and possibly will aid in the further refinement of theoretical design procedures of friction piles in sand.

1.3 Thesis Outline

The thesis is organized into eight chapters that logically follow the sequence of the work performed. Chapter 2 covers the literature review of analytical design procedures of piles in a cohesionless soil and of investigations of the soil behaviour at the soil-pile interface. The centrifuge scaling laws and modelling limitations are outlined in Chapter 3. Chapter 4 describes the test facilities and the laboratory equipment used in the study. Furthermore, the design of the pile model, instrumentation and hydraulic actuator are presented. Chapter 5 describes the experimental procedures for the various tests performed. Chapter 6 contains the centrifuge model test results. Chapter 7 compares and analyzes the test data with commonly accepted analytical design calculations. Particular observations with respect to pile shaft performance during load reversals are evaluated. Chapter 8 concludes the written analysis with a brief summary of the observations and theories developed followed by recommendations to both friction pile design in sand and further development of the analysis of pile shaft capacities with a geotechnical centrifuge. Chapter 8 is followed by a list of references, which concludes the thesis. In place of an appendix, a supplementary compact disc (CD-ROM) may be obtained, which contains all the centrifuge model tests in an indexed graphical format (Hanke, 2001).

CHAPTER 2

Literature Review

2.1 Analytical Design Procedures

2.1.1 Cylindrical Pile in Sand

When a single cylindrical pile is driven, or jacked as in the case of the centrifuge model, the axial resistance is due to both the end bearing and the skin friction. The total resistance (Q_d) may be expressed as

$$Q_d = Q_p + Q_s = q_p A_p + 2\pi R f_s D_f = q_p A_p + C f_s D_f \qquad (2.1)$$

Where q_p = soil bearing resistance at the pile base, A_p = pile end bearing area, C = pile circumference, f_s = average shaft friction per unit area, and D_f = depth of pile. Failure of the soil beneath the pile toe can not occur without some of the bearing soil displacing upwards and outwards as shown in Figure 2.1. If the soil within the depth D_f is more compressible than the material beneath the base the pile displacement would cause very little shear stresses within the depth D_f, therefore the material above the pile tip would only have an influence similar to a surcharge of intensity γD_f and the bearing capacity factor N_q may be utilized (Terzaghi *et al.* 1996). Conversely, if the soil body were homogeneous at and above the pile base, the shear stresses would set up at depths less than D_f. Since shear stresses are usually related to soil friction angle ϕ' and existing

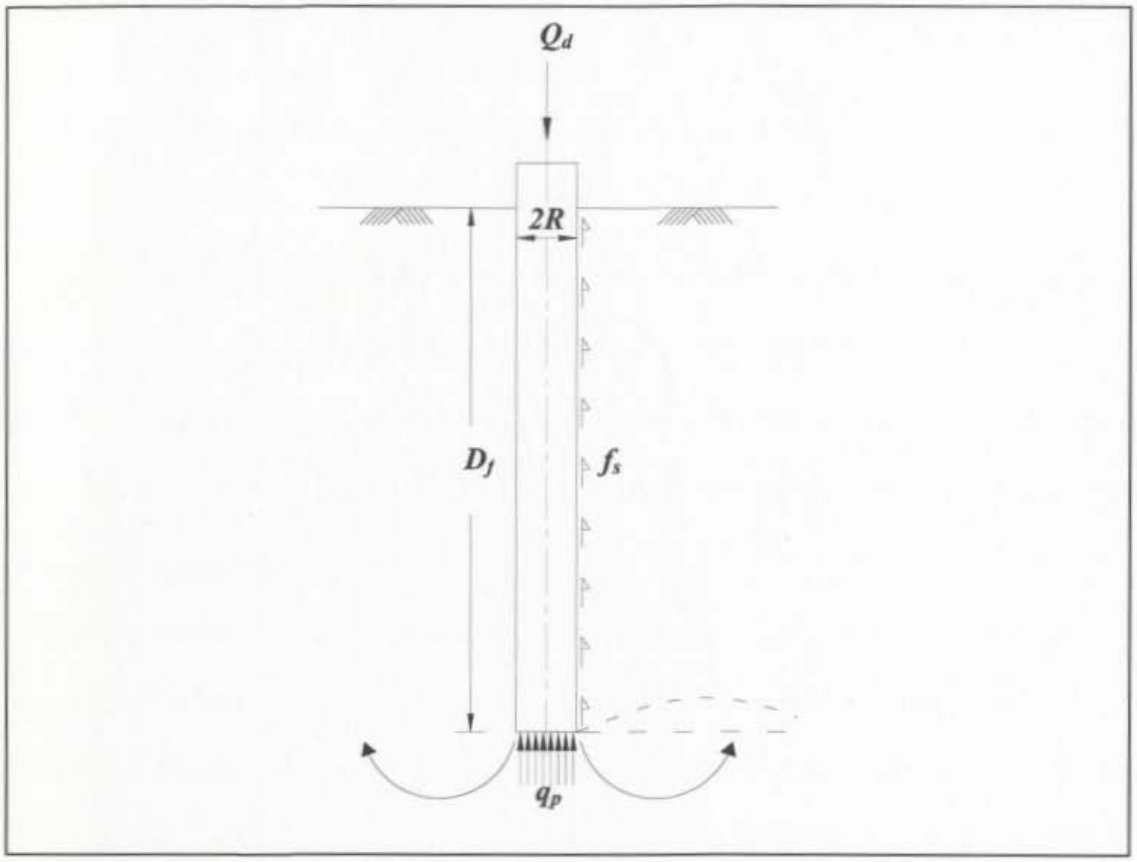

Figure 2.1 Schematic of an axially loaded cylindrical pile (after Terzaghi *et al.* 1996).

normal stresses, the bearing capacity factor N_q would then become a function of both ϕ' and the ratio of $D_f/2R$ (Terzaghi *et al.* 1996). A modified factor N_q^* that considers the above mentioned shear pattern was developed by Berezantzev and presented by Tomlinson (1995).

For a vertical pile the pile skin friction (f_s) is usually considered to be the product of the effective horizontal stress (σ'_h) and the tangent of the sand-pile interface friction angle (δ) as given in the following equation (Johannessen and Bjerrum, 1965; Bozozuk, 1972).

$$f_s = \sigma'_h \tan\delta = K\sigma'_v \tan\delta \qquad (2.2)$$

Where K = ratio of effective lateral to effective vertical stress and σ'_v = the effective vertical stress at depth z. Some design formulations consider K as the at-rest lateral earth pressure coefficient (K_o), where K_o is equal to $1-\sin\phi'$, for low displacement piles. Conversely, up to the 15th edition of API RP2A, the American Petroleum Institute recommended earth pressure coefficients of 0.5 and 0.7 for tension and compression respectively and after 1984 recommended a coefficient of 0.8 for both tensile and compressive f_s computations for low displacement piles. For higher displacement type piles K is normally taken as twice the value of K_o (Canadian Foundation Engineering Manual, 3rd edition) whereas the Foundation and Earth Structure Design Manual 7.2 (1982) and Craig (1997) report values of 1 and 2 for loose and dense sand, respectively. The maximum earth pressure coefficient that may be applied is bounded by the Rankine passive earth pressure coefficient (K_p). Theoretically, the minimum value would be equal to the Rankine active earth pressure coefficient (K_a). On the other hand, Alawneh (1999) reported cases where the average earth pressure coefficient reached a value as low as 0.23, which was below the active Rankine state. For very long piles in loose sand Alawneh recommends a minimum K value of 0.23. Combining Equations (2.1) and (2.2) yields Equation (2.3) that may be used to estimate the total pile resistance as the sum of the end bearing and shaft resistances.

$$Q_d = \sigma'_{vb} N_q^* A_p + C\int_0^D f \, K\sigma'_v \tan\delta \, dz \qquad (2.3)$$

Where σ'_{vb} = effective vertical stress at the pile toe. The tensile pile resistance is generally considered to be less than the compressive shaft resistance. Some design

procedures suggest that the tensile shaft resistance be computed as a ratio of the compressive shaft resistance described above. Terzaghi *et al.* (1996) recommended a tensile to compressive ratio of 0.5 whereas Jardine *et al.* (1998) recommend a ratio of 0.8 to be applied to a portion of the shaft stress, which means that the actual tensile to compressive ratio is considered to be greater than 0.8. The 14th edition of API RP2A suggested the tensile shaft resistance was about 70% of the compressive value by applying separate earth pressure coefficients (Toolan *et al.* 1990). The difference between the two values of shaft friction is due in part to the fact that a downward movement of the pile can cause a volumetric dilation of the sand at the pile interface while an upward movement can cause contractive strains thereby reducing the horizontal stresses acting along the length of the pile shaft. Conversely, Ireland (1957) and others have recommended that the tensile shaft resistance may be considered equal to the shaft resistance in the compressive state. This was added to the 15th edition of API RP2A that recognizes the equivalence of shaft resistance between tensile and compressive loading of open ended pipe piles (Kraft, 1990).

The rotation of the principal stress axis may also explain the lower shaft resistances observed with tensile loading. Laboratory soils tests have shown that shear stress reversals result in a reorientation of the principal stresses (Symes *et al.* 1984; De Nicola and Randolph, 1993; Eigenbrod, 1998). The sand-pile interface friction angles for both tensile and compressive loading may be estimated with a modified direct shear test. Eigenbrod (1998) reported that the interface friction angle (δ) may be as much as 11°

greater in the compressive loading direction than in the secondary or tensile direction. However, tensile pile capacities were sometimes higher than compressive shaft capacities, depending on soil type. This phenomenon possibly explains the observed differences between tensile and compressive pile shaft resistances. Terzaghi *et al.* (1996) point out that the sand-pile interface friction angle is unlikely to be equal to the interface friction angle determined with a modified direct shear test due to the rearrangement and crushing of the sand grains along the pile shaft that result from the driving process.

Researchers have hypothesized that the Poisson's effect in the pile shaft may be a contributing factor to the difference in tensile and compressive shaft resistance. De Nicola and Randolph (1993) suggest that when estimating shaft capacities the ratio of expansion and contraction of the pile during compression or tension must be considered, because the radial effective stress field in the soil surrounding the pile shaft is affected. It is proposed that the ratio of tensile to compressive shaft capacity should be analyzed as a function of the pile's slenderness and stiffness ratios.

Many researchers suggest that a pressure bulb at the pile toe is generated with the mobilization of pile end bearing. The mobilization of end bearing and the ensuing pressure bulb generation are said to influence the lateral stresses acting along the pile shaft (Kraft, 1991; De Nicola and Randolph, 1993; Craig, 1997). It is reported that when a pile is loaded to failure in compression the proportion of shaft resistance will decrease slightly due to the plastic flow of soil near the pile toe, which in turn reduces the lateral

stresses acting on the pile shaft near the base. Kraft (1991) states that during compressive failure the interface soil near the base moves downward with the pile resulting in a reduction in the shaft resistance within that zone. Despite the localized area of reduced shaft stress near the pile toe, the shaft resistance is reported to be greater during compressive failure than the tensile loading condition. Some researchers have observed the generation of a pressure bulb with the mobilization of pile end bearing and believe it has more of an influence on shaft resistance than the small localized area of plastic flow just above the base (Kezdi, 1964; Eigenbrod and Issigonis, 1996). With the end bearing fully mobilized, the pressure bulb is thought to curl up around the pile shaft as much as 9 pile diameters above the base. Within this zone the lateral confining stresses are said to increase with the mobilization of end bearing and reduce during tensile loading due to the absence of the pressure bulb.

Kezdi (1964) performed instrumented model pile tests driven into sand. During pile driving, soil displacements were shown to develop about 2 pile diameters ahead of the advancing pile toe. The lateral displacements started at 2 diameters below the toe and reached a peak of about 3 diameters radially at point about 5 diameters above the pile toe. Above this point 5 diameters above the pile toe the lateral displacements remained at a maximum of 3 diameters. Magnitude of the lateral displacements was observed to decrease with distance from the pile in a hyperbolic fashion to zero at a distance of 3 diameters from the pile axis. The magnitude of soil displacements obviously influences the horizontal stresses acting on the pile shaft. Following the pattern of soil

displacements, Kezdi (1964) shows that even though the shaft stress increases are zero near the pile toe, the maximum shaft stress is found about 3 to 5 pile diameters above the pile toe.

Eigenbrod and Issigonis (1996) drove steel piles through soft sensitive clay into a very dense sand and gravel while monitoring pore-water pressure response. Very small pore pressures and low driving resistances were observed during driving in the soft clay. Conversely, pore-water pressures increased with the increase in driving resistance once the piles penetrated the underlying very dense sand and gravel. It was concluded that the clay layer was loaded from below, once the piles were driven into the sand deposit.

It is suggested that the delineation of the failure zone defining the stress or pressure bulb in a homogenous soil may be defined as a logarithmic spiral (Meyerhof 1951; De Beer 1963; Vesić 1967; Eslami and Fellenius, 1997). The principle of the logarithmic spiral rupture surface around the pile toe is shown in Figure 2.2. The radius of the general shear failure may be estimated with

$$r = r_o e^{\theta \tan\phi} \qquad (2.4)$$

Where r = the radius of the logarithmic spiral, r_o = the radius of the spiral for $\theta = 0$ (assumed to be equal to the pile diameter), θ = angle between a radius and r_o, and ϕ = the soil internal friction angle.

The height of the failure above the pile toe (r_c) may be determined with Equation (2.5).

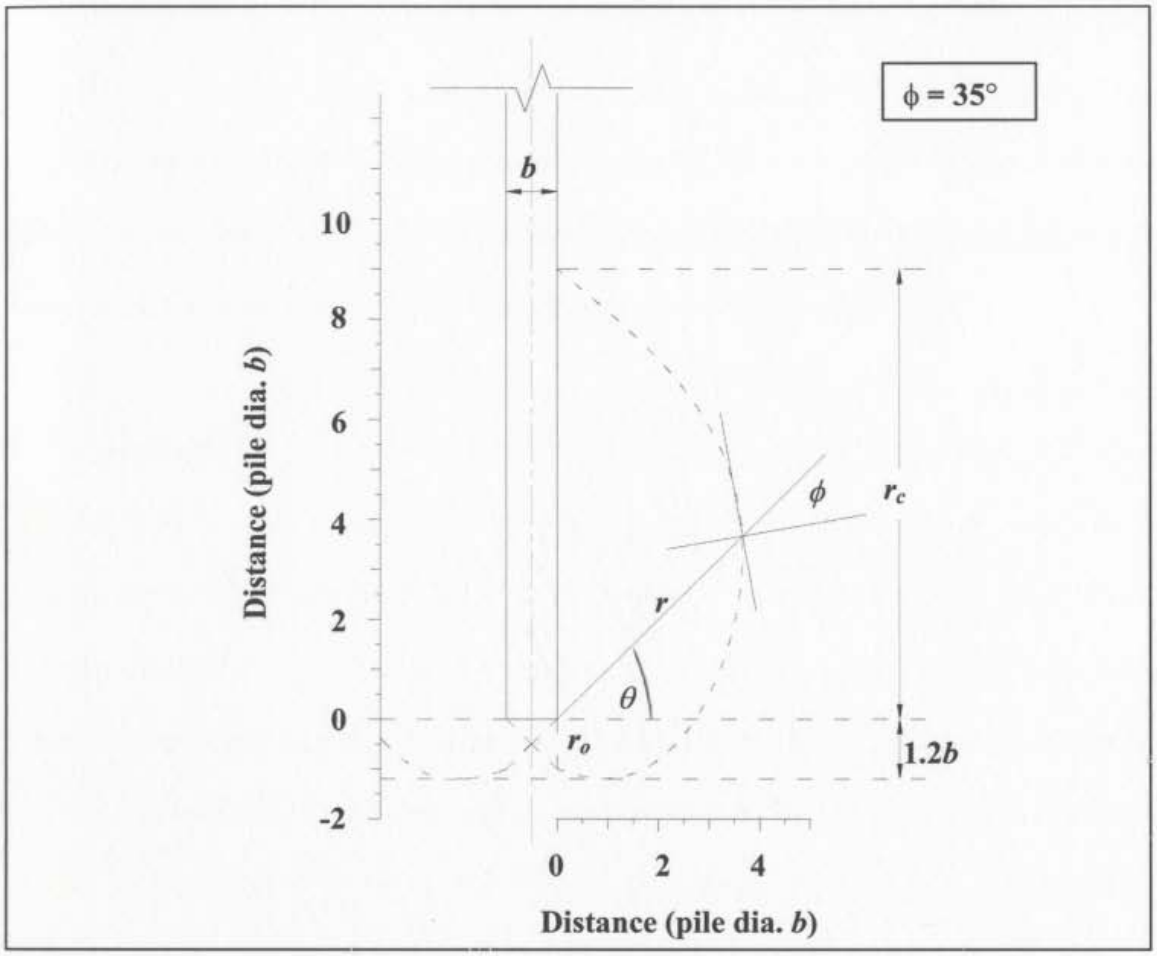

Figure 2.2 Logarithmic spiral failure surface around the pile toe (after Eslami and Fellenius, 1997).

$$r_c = be^{\pi \tan\phi} \tag{2.5}$$

Where r_c = the height of the failure zone above the pile toe, and b = pile diameter.

If Equation (2.3) is used to calculate the ultimate pile capacity in sand, Q_d should increase directly with pile penetration since σ'_v is a function of depth z. Conversely, Vesić (1967) introduced the concept of a *critical depth*. Through model tests and load tests on full-

scale piles it was observed that Q_d increased linearly with depth until a point at which the increases in capacity slowed and became nearly constant. For a cylindrical pile the critical depth was found to be dependent on the pile diameter and the initial relative density of the sand. For initially loose sands the critical depth was reported to appear at depths as shallow as $7b$ (pile diameter), and may exceed $20b$ in dense sand.

The concept of a critical depth at which the ultimate pile capacity is achieved has been a point of debate amongst researchers. Kulhawy (1984) explained that in most sand deposits some extent of overconsolidation is present. Therefore, the at-rest lateral earth pressure coefficient (K_o) is largest near the ground surface and decreases with depth until it reaches a constant level within the normally consolidated range. Furthermore, one may take into account that stress level and increasing depth influence the soil-pile interface friction angle. Kulhawy suggests that the apparent critical depth is just a coincidence, which occurs because the decreasing $K\tan\delta$ term and the increase in depth z cancel each other out and give the illusion of a critical depth. When in actual fact the values of parameters defining f_z continually change with depth. Building on Kulhawy's hypothesis, Kraft (1991) performed a series of cone penetrometer tests that did not give any evidence of a limiting value for neither end bearing nor skin friction. The rate of resistance increase did decrease with increasing depth, but a limiting resistance value was never achieved.

It is a well-known fact that cyclic loading in sand produces pile displacements which will result in degradation of skin friction. Poulos and Chan (1986) report that cyclic displacements in the order of 0.1% to 0.2% of the pile diameter are required for skin friction degradation to occur. For cyclic displacements in the order of about 2% or more of the pile diameter, it is reported that the skin friction could reduce to about half of the initial static value. Cyclic axial pile model load tests performed by Eigenbrod (1998) resulted in compressive skin friction degradation of about 55% and a 40% reduction in tensile skin friction after just four load cycles. Kraft (1990) states that the ultimate shaft resistance under cyclic loading will be about 30 to 40% of the static shaft resistance but does not differentiate between tensile or compressive shaft degradation. After the second load cycle the degradation rates are known to reduce significantly for both the tensile and compressive loading directions. Poulos and Chan (1986) state that the majority of skin friction degradation will occur within the first ten load cycles regardless of the method of pile installation.

2.1.2 Pile Capacity Determination with CPT

Investigations for piled foundations require the measurement of shear strength at sufficient points in the soil column to reasonably define its variation with depth for the computation of preliminary pile capacity. The shear strength is difficult to obtain from samples, considering the sample disturbance and the reduction in confining stresses once brought to the surface (ARGEMA, 1992). To obtain the *in-situ* properties while incorporating the least amount of error, lab testing is replaced by *in-situ* testing. *In-situ*

tests allow both qualitative and quantitative interpretation of the soil profile and soil properties, and generally avoid problems associated with sampling disturbance in laboratory samples (Poulos, 1988). Common *in-situ* test techniques are the pressuremeter test, standard penetration test (SPT) and the cone penetrometer test (CPT).

Because the cone penetrometer test (CPT) has similarities to a pile, it was attempted to estimate pile capacity from CPT results. It has been suggested that the average shaft friction f_s is equal to $\bar{q}_c/200$ for piles in sands and $\bar{q}_c/150$ for piles in non-plastic silts, where $\bar{q}_c$ is the average cone resistance over the embedded length of the pile (Craig, 1997).

More rigorous attempts of correlating cone resistance to pile capacities have been undertaken by many researchers (Horvitz *et al.* 1981; Meyerhof 1983; Eslami and Fellenius, 1997; Jardine *et al.* 1998;). The measurement of skin friction (f_s) acting along the cone sleeve enables a direct correlation of pile skin friction to measured test data. In essence, the advancing sleeve is a cylindrical pile model. Pile shaft skin friction (f_s) calculation is commonly based upon a function of effective vertical stress (σ'_v), lateral earth pressure coefficient (K) and the tangent of the soil-pile friction angle (δ). The cone sleeve can measure f_s directly and alleviate the need for determination of K. Furthermore, the ratio between measured skin friction (f_s) and toe resistance (q_c) can be back calculated to estimate the material internal friction angle (ϕ) and material type along with various

other soil parameters such as liquefaction potential. Together, this gives the ability to estimate pile performance without the need for further laboratory testing.

Meyerhof (1983) presented a general procedure for directly predicting pile end bearing and shaft friction with CPT data. Summarized and presented by Eslami and Fellenius (1997), the procedure estimates the unit toe resistance (q_p) of a driven pile with the following equations.

$$\text{if } b>0.5 \text{ m then} \quad C_1 = \left(\frac{b+0.5}{2b}\right)^n \quad \text{else } C_1 = 1 \tag{2.6}$$

$$\text{if } D_b>10b \text{ then} \quad C_2 = \frac{D_b}{10b} \quad \text{else } C_2 = 1 \tag{2.7}$$

$$q_p = q_{ca} C_1 C_2 \tag{2.8}$$

Where b = pile diameter, q_{ca} = the average CPT toe resistance q_c in a zone $4b$ above the pile toe and $1b$ below, C_1 = scale effect modification factor, C_2 = material density modification factor, n = 1 for loose sand, 2 for medium dense sand, and 3 for dense sand, and D_b = pile embedment (m) into a dense strata.

The average unit shaft resistance (f_s) is determined with

$$f_s = 0.005 q_{ca} \tag{2.9}$$

CPT data has been used to determine both pile shaft and end bearing resistance in a more site specific manner than presented above. Lehane and Jardine (1994) and Jardine *et al.*

(1998) have presented a new design procedure for estimating shaft capacities of offshore piles, driven in sand, with the use of cone penetrometer testing. The design procedure was calibrated with instrumented model piles within the laboratory, full-scale load tests and incorporation of the existing API (America Petroleum Institute) database of offshore pile capacities. The selected database of sands had relative densities (I_D) between 20 to 95% and a mean grain size (d_{50}) between 0.1 to 0.3 mm. This cautious design procedure may only be applied to *in-situ* conditions matching those of the database used to calibrate the model and therefore may not be generally applied as the Meyerhof procedure presented above. This design procedure dissects the pile shaft friction into two components, the equalized radial effective stress (σ'_{rc}) and a dilatant stress component ($\Delta\sigma'_{rd}$). The equalized radial effective stress at any point can be calculated by using the following equations.

$$\sigma'_{rc} = 0.029 q_c \left(\frac{\sigma'_{vo}}{P_{atm}}\right)^{0.13} \left(\frac{h}{R^*}\right)^{-0.38} \quad \text{where } h/R^* \geq 8 \qquad (2.10)$$

$$R^* = (R^2_{inner} - R^2_{outer})^{0.5} \qquad (2.11)$$

Where σ'_{rc} = equalized radial effective stress, σ'_{vo} = effective vertical stress, P_{atm} = atmospheric pressure, h = distance of pile toe to point of consideration, R_{inner} = inner pile radius, R_{outer} = outer pile radius, and R^* = modified pile radius.

The equalized radial effective stress is known to increase with depth but at any fixed point along the pile length the value decreases as the distance of the pile tip below the fixed level increases with continued pile penetration. Once the pile tip passes a given

depth within the soil stratum, continued pile penetration and further development of pile shaft movement past that point will result in a constant reduction of the equalized radial effective stress. This is in accordance with the studies and findings of Toolan *et al.* (1990). Lehane and Jardine (1994) observed that the equalized radial effective stress path with depth closely followed the path of the CPT end bearing resistance (q_c). Analysis of the extensive API database, full-scale pile tests and model tests enabled a correlation of CPT q_c with σ'_{rc}.

It has been observed that during static loading significant net changes in radial stress occurred only after interface slippage. Soil dilation upon shearing is believed to be responsible for the additional component of normal stress at failure. The net dilatant component ($\Delta\sigma'_{rd}$) for any level within the soil stratum can be estimated as

$$\Delta\sigma'_{rd} = \frac{4GR_{cla}}{R} \tag{2.12}$$

The dilatant component is a function of the shear modulus (G), pile radius (R) and the pile's center-line-average roughness (R_{cla}). Jardine *et al.* (1998) state that for a typical steel pile, $R_{cla} \cong 10^{-5}$m. Studies have shown that the change in stress, due to soil dilation, for large piles is relatively small but can dominate the capacities of micro-piles or laboratory scale model piles. Calibrated from a database of pile load tests and CPT investigations, Equations (2.13) and (2.14) are used to calculate the shear modulus (G).

$$\eta = \frac{q_c}{\sqrt{P_a \sigma'_{vo}}} \tag{2.13}$$

$$G = q_c(A + B\eta - C\eta^2)^{-1} \tag{2.14}$$

Where η = dimensionless coefficient, $A = 0.0203$, $B = 0.00125$, and $C = 1.216 \times 10^{-6}$.

Jardine *et al.* (1998) suggest that the equalized radial effective stresses in tension are about 80% of the stress in the compressive state. The ultimate compressive and tensile shaft stresses (σ'_{rf}) at any given point along the pile can be calculated with Equations (2.15) and (2.16) respectively.

$$\sigma'_{rf} = \sigma'_{rc} + \Delta\sigma'_{rd} \tag{2.15}$$

$$\sigma'_{rf} = 0.8\sigma'_{rc} + \Delta\sigma'_{rd} \tag{2.16}$$

Where σ'_{rf} = ultimate pile skin stress, σ'_{rc} = equalized radial effective stress, and $\Delta\sigma'_{rd}$ = change in radial stress due to soil dilation.

2.2 Soil-Pile Interface

Laboratory testing and analyses of cyclic soil-steel interface behaviour have been reviewed. The scope of the review investigates non-cohesive soils and considers the effect of both small strain and large strain cyclic loading.

Many researchers have investigated the interaction of dry and saturated sand on interfaces under cyclic shear. Modified laboratory tests such as the standard direct shear test, simple direct shear, triaxial cells and torsional shear tests have been used to carry out such investigations. Parameters that influence the cyclic and post-cyclic shear response are sand gradation, mineral composition, void ratio, fabric, stress history, strain magnitude and interface roughness.

2.2.1 Pore Water Pressure

Shear along a sand-pile interface is generally considered to occur at drained conditions with no pore water pressure changes. However, Alarcon-Guzman *et al.* (1988) suggest that pore pressure generation due to structural collapse must be considered. Strain-softening behaviour is associated with the fact that the structure of contractive sand is metastable. In this collapsive skeleton, small shear strains are capable of producing a sudden rearrangement of soil particles. The rearrangement of grains and loss of contact points between neighboring grains may account for the contractive behaviour of some sands. In the undrained state, the particle contact points are shifted to water filled voids where this transfer of load will result in a sharp increase in pore water pressure. Subsequently, the shear strength is reduced and large deformations result. Once the sand particles are oriented, steady state conditions are said to follow. With respect to cyclic loading effects, the initiation of strain softening is said to depend on the cyclic amplitude. Larger cyclic deformations result in fewer cycles to reach strain softening regardless of the amplitude and number of cycles. The flow or collapse was observed to consistently occur at a given cumulative shear strain (Alarcon-Guzman *et al.* 1988).

2.2.2 Interface Behaviour

Normal stiffness tests (stress path tests where $dF_N/d\Delta v$ = constant) are considered to well represent the interface shearing behaviour of such structures as retaining walls, pile shafts and pipelines. A shallow foundation may transmit a constant or close to constant normal stress but the soil in contact with these structures has a varying normal stress during events

leading to the initiation of active or passive earth pressures. For a circular pile shaft, the soil within the shear band or interface zone is constrained by the soil beyond this zone; as a result the normal stress acting on this zone varies during shear. When trying to model this behaviour within the laboratory, Airey *et al.* (1992), Evgin and Fakharian (1996) and others found that constant normal stiffness (CNS) tests better represent these events than standard constant normal stress direct or simple shear tests.

For the characteristics of a sand-steel interface, the following assumptions can be made. In the sand surrounding a pile or pier subject to axial loading two distinct regions can be visualized. The first is a very thin cylindrical layer of sand at the contact surface of the steel. Proposed by Swinianski and Sawicki (1991), this region is considered to behave much like that of direct shear conditions, subject to volumetric strains. The second region is a wide band of sand surrounding the first region, which behaves like soil in simple shear test conditions at constant volume.

Similar to Swinianski and Sawicki (1991), Airey *et al.* (1992) describe the sand-pile interface as a very thin shear band along the steel pile surface while the outlying sand is considered to be in an elastic state with a constant shear modulus (G). Airey *et al.* (1992) performed a series of constant normal stiffness (CNS) direct shearbox tests to analyze the degradation of shear stress with respect to cyclic loading. It was attempted to correlate the degradation of stresses in the shearbox to the reduction of the frictional capacities of the pile shaft during cyclic loading. The decrease in pile skin friction was believed to be

associated with a decrease in normal stress resulting from compressive strains in the soil adjacent to the pile surface. CNS direct shear tests were performed on noncemented calcareous sand, which considered the expansion and contraction of the soil near the pile interface upon shear. The effects of expansion and contraction of sand under shear at the soil-pile interface can be reproduced by using a spring with a constant stiffness to apply the appropriate normal load. The model presented by Airey *et al.* (1992) utilized a spring constant (K) described by $K = 4G/b$ where b is the pile diameter and G is the soil shear modulus, assuming that the spring stiffness is a function of pile diameter. It is reported that the shaft friction is dependent on pile diameter with the maximum shear stress decreasing with increasing pile diameter (Airey *et al.* 1992; Turner and Kulhawy, 1994; Tabucanon *et al.* 1995). Because the thickness of the shear band is reasonably constant ($\approx 10 d_{50}$), the volume of soil experiencing volumetric shear strain decreases in proportion to the pile surface area as the shaft diameter increases.

By performing tests with various values of spring stiffness (K) Airey *et al.* (1992) determined the influence of the spring stiffness on shear response with displacement controlled CNS tests. Increasing the normal stiffness on dense dilative sand results in larger normal and shear stresses during the initial static loading whereas the reverse is true for loose contractive sand. Increasing the normal stiffness also results in larger displacements to reach the peak shear strength. As well, the rates of shear stress degradation with cyclic loading were greatest for higher values of K.

2.2.3 *Friction Angle*

Direct shear testing of sand over a rough steel surface with a constant normal stiffness reveals that the interface friction angle (δ) equals the sand internal angle of friction (ϕ) (Kishida and Uesugi, 1987). The shear resistance along a sand-pile interface is dependent on the roughness of the contact surface with respect to the mean grain size of the sand. As the interface roughness increases shearing takes place more within the sand to a point where the sand grains become locked into the depressions within the pile surface and shearing takes place between a sand-sand interface. Whereas over a smooth steel interface the sand particles are sheared at the steel surface thereby making δ the applicable friction angle. Furthermore, the sand particles were found to slip along the smooth steel surface resulting in a much lower mobilized shear stress and giving skin friction angles as low as 10° (Tabucanon *et al.* 1995; Lemos and Vaughan, 2000). Alawneh (1999) recommends the general use of δ values equal to 4° less than the sand internal angle of friction at constant volume (ϕ_{cv}) whereas Craig (1997) generalizes the approach and recommends δ value of 20° for all steel piles in sand.

Orman (1994) undertook direct shear tests of two soil types on a smooth and roughened HDPE interface. The sand mobilized 70% of its full shear strength against both nominally rough and smooth interfaces, as the sand particles were significantly larger than the surface roughness. A silt mobilized its full shear strength against the rough interface, but only 43% against a smooth interface as the silt particle sizes were of the same order as the surface roughness. The effect of surface roughness was quantified by Kishida and

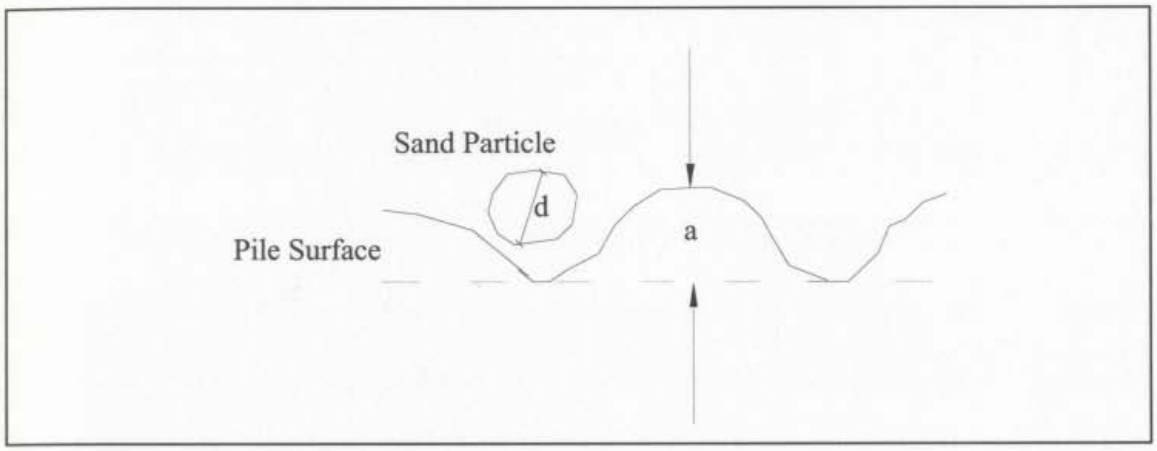

Figure 2.3 Pile surface roughness evaluation.

Uesugi (1987) using a normalized roughness factor as the ratio of the maximum surface asperity depth (a) by the mean particle size (d_{50}) as shown in Figure 2.3. They found from simple shear tests that at a factor of about 0.1 the full sand friction angle was mobilized at the interface, but this resistance decreased fairly linearly to about half that friction for a smooth interface with a (a/d_{50}) factor that approaches 0.

2.2.4 Stress Path

Evgin and Fakharian (1996) undertook investigation of the dependence on stress paths with CNS direct shear tests on both a 2-D and 3-D plane. It was concluded that the magnitudes of the peak principal stress ratio and residual principal stress ratio are independent of the stress paths. The residual stress ratio was found to be independent of the magnitude of the normal stress. It was also determined that the stress paths significantly influence the shear stress tangential displacement and the volumetric behaviour of the interface. In 3-D CNS tests, the shear stress developed in one direction was dependent on the magnitude of the

shear stress developed in the orthogonal direction of the interface plane (Evgin and Fakharian, 1996).

2.2.5 Grading

Lee and Poulos (1987) sheared both uniformly graded (gap graded) calcareous sand and well graded silica sand along a steel pipe surface. The porous uniformly graded calcareous sands exhibited a very rapid decrease in frictional capacity with increased cyclic displacement reaching a state of constant frictional capacity after small values of normalized cyclic displacements. This behaviour was unlike that of the well-graded sands which displayed a gradual decrease in strength over larger values of normalized displacement. Observing the frictional degradation with respect to the number of cycles revealed that the uniformly graded sands decreased in strength quickly after the first few cycles with virtually no degradation beyond 10 cycles. In contrast, the well-graded material displayed a more gradual degradation slope, which continued beyond 10 cycles. Test results also reveal that the rate of degradation decreases with both increasing relative density (I_D) and over consolidation ratio (OCR).

2.2.6 Grain Crushing

Several researchers reported instances of an increase in interface shearing resistance after the first shear cycle. But subsequently the shear resistance decreased together with the normal stress at about a constant stress ratio (τ/σ_n) with continuous load reversals (Uesugi *et al.* 1989; Boulon and Nova, 1990; Tabucanon *et al.* 1995). This phenomenon

is thought to be due to grain crushing of weak calcareous sand particles during cyclic shear testing, although grain crushing has also been observed for siliceous sands. The increase in strength is short term, for with continued cycling the particle crushing may lead to a net compression resulting in a reduction in normal stress significant enough to reduce the shear strength. Particle crushing was shown to increase with both cyclic shear amplitude and normal stress.

2.2.7 Critical Level of Repeated Loading

Turner and Kulhawy (1992) investigated the strength changes along a sand interface following cyclic shear in order to verify that cyclic loading that was not exceeding the static yield strength could affect the shear strength by changes in void ratio (e) and soil fabric. Torsional undrained simple shear tests were performed on loose, medium and dense sands in both a static and cyclic manner, with the cyclic load below the static yield strength. The sand-sand interface of the torsional shear test is thought to be similar to the shear interface of sand sheared over a rough steel surface. When shearing over a rough interface the sand grains become locked into the depressions within the steel surface and shearing will take place between the sand grains alone. Cyclic shear test results on loose sand revealed a reduction in void ratio and an increase in friction angle for samples of loose relative densities (I_D). After 600 shear cycles the static shear strength increased by 8 to 44% from the initial static shear strength prior to cyclic loading. Samples of medium dense relative densities also exhibited contractive behaviour, small reductions in volume, with an increase in friction angle and strength increases ranging from 19 to 44%. The

dense samples exhibited volumetric dilation resulting in a decrease in friction angle. Certain dense samples loaded at a larger cyclic shear stress ratio were observed to fail during cyclic loading. The cyclic shear stress ratio is defined as the ratio of applied cyclic shear stress to the shear stress required for failure prior to cyclic loading. The samples failed at shear stress ratios of n = 0.5 and 0.75 within 250 and 10 cycles respectively. It is reported that when the specimens were loaded above the CLRL (critical level of repeated loading) ultimately the post-cyclic strength corresponded to the critical state friction angle (ϕ_{cs}). The CLRL is the condition at which the soil does not accumulate either strain or excess pore water pressure with additional cycling. It is the cyclic stress level that separates potentially unstable conditions from stable conditions under continued cycling. The CLRL for sands subject to a one-way repeated load is said to be about 30% of the ultimate static capacity while the CLRL is smaller yet for sands under a two-way cyclic load (Swinianski and Sawicki, 1991).

2.3 Literature Review Summary

An extensive literature review has uncovered a lack of consistency between the various design procedures proposed. The calculation of the average pile shaft shear stress may be estimated with analytical formulations or by *in-situ* testing. Either approach could yield vastly different estimates for either end bearing or shaft capacities. Furthermore, the literature review has revealed a lack of computational procedures for the determination of tensile shaft stress. The tensile shaft capacity is generally considered to be less than the compressive and in many cases is expressed as a ratio of the former. As of the 15th

edition of API RP2A, API does not differentiate between tensile and compressive shaft resistances, whereas Terzaghi *et al.* (1996) recommended a ratio of 0.5 and Jardine *et al.* (1998) recommend a ratio slightly greater than 0.8. Conversely, Ireland (1957) suggested that the tensile and compressive shaft capacities are approximately equal.

Further controversy is introduced when deciding which earth pressure coefficient or interface friction angle is appropriate. A wide range of earth pressure coefficients was recommended for driven piles in sand. Some sources suggest a constant coefficient for all driven piles, while others base K on the relative density of the soil and pile diameter. A range of recommended interface friction angles are documented in the literature. Direct measurement of δ may be performed in the laboratory but it is said that this method will yield conservative results.

The apparent cause for greater shaft resistance in the compressive loading direction versus the tensile is another point of discussion. It is generally believed that the downward movement of the pile shaft under compressive axial loading will produce volumetric dilation of the confining soil around the pile, while a tensile displacement will produce contractive strains and therefore a decrease in the lateral stresses acting along the pile length. Rotation of the principle stress axis is believed to be a key factor influencing the volumetric behaviour and subsequently the axial shaft capacity. Researchers have also stated other possible reasons such as the Poisson's effect of the pile. Furthermore, the compressive axial loading and mobilization of end bearing is believed to create a pressure

bulb that curls up around the pile shaft and increases the lateral stresses acting on the lower portion of the pile shaft.

Researchers that have investigated the effects of cyclic axial loading of piles in sand, have reported a negative influence on shaft capacity with an increasing number of cycles or load reversals if the critical level of repeated loading (CLRL) is exceeded. Factors that influenced the cyclic response were found to be the pile diameter, soil relative density, grain size distribution, material composition and the magnitude of cyclic displacement. Shaft stresses were reported to decrease with increasing pile diameter. Initially dense sands are reported to have shaft resistance degradation rates less than sands of an initially loose state. Furthermore, the rate of pile shaft resistance degradation with cyclic loading decreases with increasing overconsolidation ratio (OCR). It was reported that the material gradation has a profound influence on the cyclic behaviour of shaft friction. The pile frictional capacity degrades rather quickly for uniformly graded sands and exhibits a much gentler degradation rate for well-graded sands. Grain crushing was reported to influence the frictional behaviour of piles during load reversals. Particle crushing is dependent on the material composition, stress level and the cyclic shear amplitude.

CHAPTER 3

Centrifuge Modelling

3.1 Introduction

Coulomb's strength criterion for soils is widely recognized by geotechnical engineers and researchers. The criterion is appropriate for frictional materials and states that the shear failure depends on pressure or stress level. This statement is fundamental in the development of the criteria of soil failure in modern soil mechanics. The geotechnical centrifuge technique properly simulates the stress-dependent behaviour of soils and centrifuge modelling is now a well-recognized and respected form of modelling soils and soil-structure interaction. Centrifuge modelling has shown to be very useful in modelling gravity dependent phenomena (e.g. Ketcham *et al.* 1997; Murff, 1997; Schofield, 1980). This is accomplished by placing a model within a centrifuge. During operation, the centrifuge generates an inertial radial acceleration field that simulates gravity. The exaggerated gravitational field allows for similarity of stresses between the model and the corresponding prototype.

Soil models placed at the end of a centrifuge arm can be accelerated to achieve an inertial radial acceleration field which, to the model, simulates normal gravity but many times stronger than Earth's gravity. A soil model commonly has a free upper surface,

unstressed and open to the atmosphere. The material within the soil body has an increasing stress level that increases with depth at a rate that is dependent on material density and the magnitude of the accelerated gravitational field.

It is important to remember that a centrifuge model is a simplification of the corresponding prototype and only represents a unique situation and has certain limitations due to the simplified nature of physical modelling. Proper appreciation of the model limitations is required to enable a given level of confidence to be applied to test data. The two key issues in centrifuge modelling are scaling laws and errors, both of which are discussed in detail within the following sections. The scaling laws can be derived by making use of dimensional analysis and consideration of the governing differential equations.

3.2 Model Scaling Laws

3.2.1 Introduction to Centrifuge Scaling

If the same soil is used in both the model and prototype and the soils both have similar stress histories, then soil stress between the model and prototype may be directly compared. When the soil model is subjected to an accelerated inertial stress field of N times Earth's gravity, the vertical stress at depth h_m in the model will be equal to the prototype vertical stress at soil depth h_p where $Nh_m = h_p$. This is the basis of centrifuge scaling laws and centrifuge modelling, that stress in the model and prototype are equal at

homologous points by accelerating a model of scale *1:N* to *N* times Earth's gravity (*g*). The scaling laws can be derived by making use of dimensional analysis.

If a model is to have an equal stress distribution to a full-scale prototype condition the correct acceleration level and geometric scale *N* must be chosen to correspond to the appropriate prototype condition (Taylor, 1995). The vertical stress (σ_{vp}) of a prototype soil of density ρ at depth h_p is given by

$$\sigma_{vp} = \rho g h_p \qquad (3.1)$$

Where g = Earth's gravity and subscript "p" represents the prototype condition, whereas subscript "m" indicates the centrifuge model. Assuming the same material is used in the same volumetric state (i.e. relative density), hence the same material density, the corresponding vertical stress in the model of scale *1:N* is given by

$$\sigma_{vm} = \rho N g h_m \qquad (3.2)$$

If stress levels between the model and prototype are to be equal ($\sigma_{vp} = \sigma_{vm}$) at homologous points then the linear dimension h_p must equal Nh_m, therefore the geometric scale factor between model and prototype is *1:N*. That is, one unit-length in the centrifuge model will represent *N* linear units in the prototype setting. Since the model is a geometric representation of the prototype, any displacements between the two conditions will also be at a model to prototype scale of *1:N*. Therefore the ratio of strains is 1:1 since strain can be defined as the ratio of displacement to a unit-length, which share a common scale factor of *1:N*. It follows therefore that the portion of the stress-strain curve mobilized in the model will be identical to what is observed within the prototype setting.

Based on the linear geometric relation of $1{:}N$, the model scales for area, volume, mass and force can all be easily visualized and derived. With a model to prototype scale of $1{:}N$ applied on a linear dimension of L, the scale for area will therefore be $1{:}N^2$ since area is defined by two geometric lengths and has a dimensional unit of L^2. Likewise for volume but to the third power ($1{:}N^3$). In many cases, since the same material is used in both the model and prototype and at the same mass density (ρ), the scale for mass is equal to that of volume ($1{:}N^3$), which is a cube of linear measure L. Since stress is at a ratio of 1:1 and is defined by a force over a unit area, it therefore follows that the model to prototype scale with respect to force is $1{:}N^2$, the same scale as area.

3.2.2 Static Time Scaling

There are different time scales: viscous, inertial and seepage phenomena (Ketcham and Black, 1995). Furthermore, the scaling laws for seepage have led to minor controversy with respect to whether or not Darcy's permeability is a relevent parameter and how to interpret the hydraulic gradiant (Taylor, 1995). As a result, time scale conflicts can occur and make correct modelling of time for certain conditions impossible. Therefore the experimenter must consider the scaling limitations imposed by the modelling laws when designing and planning the model test regime.

The consolidation states between the model and prototype must be alike to enable direct comparison. Consolidation is a function of dissipation of excess pore water pressure and

is considered to be a time related diffusion event. The degree of consolidation is described by Terzaghi's dimensionless time coefficient T_v defined below.

$$T_v = \frac{c_v t}{d^2} \tag{3.3}$$

Where c_v = coefficient of consolidation (m^2/yr), t = time duration of consolidation (yr) and d = the length of drainage path with respect to pore fluid (m). For the same degree of consolidation, which is uniquely determined by T_v, to exist in both the model and prototype, Equation (3.3) for both conditions may be equated as shown by Equation (3.4).

$$\frac{c_{vm} t_m}{d_m^2} = \frac{c_{vp} t_p}{d_p^2} \tag{3.4}$$

Considering that $d_p = N d_m$, further manipulation of Equation (3.4) yields

$$t_m = \frac{c_{vp}}{N^2 c_{vm}} t_p \tag{3.5}$$

If the same soil material is used in the model as is present within the prototype, the time scale between model and prototype would be $1:N^2$ for diffusion events such as consolidation. As well, this type of scaling would also be correct for other diffusion related events such as heat transfer by conduction, which can be applied to soil-structure events such as thaw settlement or frost heave action, both of which are currently very active areas of geotechnical research in the field of centrifuge modelling.

Further analysis of seepage flow involves investigation of material permeability and the effects of hydraulic gradient (Taylor, 1995). Darcy's law for seepage flow is defined as

$$v = ki \tag{3.6}$$

Where υ = superficial seepage velocity, k = coefficient of permeability and i = the hydraulic gradient. The intrinsic permeability K may also be used and is defined by

$$K = \frac{vk}{\rho g} \tag{3.7}$$

Where v = the dynamic viscosity. If the same pore fluid is used between the model and prototype then Darcey's coefficient of permeability now becomes a function of gravitational acceleration which leads to the apparent relation of $k_m = Nk_p$. The hydraulic gradient (i) is dimensionless and it is argued that it does not scale with acceleration. Equating Darcey's seepage law for model and prototype would then yield

$$i_m = i_p \tag{3.8}$$

$$\upsilon_m = i_m k_m = i_p N k_p = N\upsilon_p \tag{3.9}$$

It is shown with Equation (3.9) that the velocity of model seepage flow is N times greater than in the prototype. The controversy enters when the same logic dictates that soils would become impermeable under a zero gravity field. A porous media such as a soil would then appear impervious due to a lack of a hydraulic or pressure gradient that acts as the driving force. Taking this logic into consideration there is then merit to question the applicability of hydraulic gradient as a ratio of two lengths. A more appropriate representation of hydraulic gradient may be as a ratio of pressure drop (ΔP) over a linear distance (L). Substituting hydraulic gradient for a pressure gradient yields

$$i = \frac{H}{L} = \frac{\Delta\left(\frac{P}{\rho g}\right)}{L} \tag{3.10}$$

Since pressures (or stresses) are at a ratio of 1:1 between model and prototype and linear geometric dimensions are scaled at *1:N*, by equating Equation (3.10) between model and prototype one would determine that $i_m = Ni_p$. With this relation, the intrinsic permeability (K) can then be treated as a material property and remain as a constant (Equation 3.11) and would yield a seepage velocity scale as

$$K_m = K_p \tag{3.11}$$

$$\upsilon_m = i_m K = N i_p K = N \upsilon_p \tag{3.12}$$

From Equation (3.12) it is determined that the seepage flow velocity has a model to prototype scale of *N:1* as found with Equation (3.9). Considering Equations (3.11) and (3.12) and that the pore fluid travels along a path of geometric length that has a scale of *1:N*, using dimensional reasoning, the time scale for seepage would therefore follow Equation (3.13).

$$\upsilon_m = \frac{L_m}{t_m} \therefore t_m = \frac{L_m}{\upsilon_m} = \left(\frac{L_p}{N}\right)\left(\frac{1}{N\upsilon_p}\right) = \frac{t_p}{N^2} \tag{3.13}$$

The time scale factor for seepage events is $1:N^2$ as determined for consolidation and diffusion processes. If different materials were used in the model than were present in the prototype condition, Equation (3.14) would apply.

$$t_m = \frac{K_p}{N^2 K_m} t_p \tag{3.14}$$

The scaling laws for static models are displayed within Table 3.1.

Table 3.1 Dimensions and scaling factors for static geotechnical centrifuge modelling.

Parameter	Dimensions M,L,T System	Prototype	Model
Length	L	1	1/N
Area	L^2	1	$1/N^2$
Volume	L^3	1	$1/N^3$
Mass Density	M/L^3	1	1
Mass	M	1	$1/N^3$
Force	ML/T^2	1	$1/N^2$
Gravity	L/T^2	1	N
Stress	M/LT^2	1	1
Strain	---	1	1
Time	T	1	$1/N^2$
Velocity	L/T	1	N

N = scale factor

3.2.3 Viscous Time Scaling

Considering viscous forces at work if the fluid viscosity is independent of gravity a time scale different from seepage is uncovered. Ketcham and Black (1995) derive the viscous flow time scale in terms of dimensional ratios. Since stress is at a ratio of 1:1 and is defined by a force divided by unit-area, it therefore follows that the force ratio (K_F) must equal the area ratio (K_l^2) as defined by Equation (3.15). The viscous force acting on a small area A can be defined by Equation (3.16).

$$K_F = K_l^2 = \frac{F_m}{F_p} \tag{3.15}$$

$$F_v = v_s \frac{dv}{dn} A \tag{3.16}$$

Where v_s = the viscosity of the pore fluid and, dv/dn = velocity gradient. The dimesional units of velocity are L/T, therefore the velocity ratio can be defined by a combination of two ratios, the ratios of length (K_l) to time (K_t), as shown in Equation (3.17). Converting Equation (3.16) into the form of a ratio yields the viscous force ratio (K_{Fv}) in terms of a combination of two dimensional ratios (Equation 3.18).

$$\frac{K_l}{K_t} = \frac{v_m}{v_p} \tag{3.17}$$

$$K_{Fv} = \frac{K_l^2}{K_t} \tag{3.18}$$

Since K_{Fv} must equal K_F as noted earlier (Equation 3.15), K_t must therefore be equal to 1 if the viscous forces are to be scaled in the same manner as the weight forces. Therefore the model to prototype time scale for viscous events is 1:1.

3.2.4 Dynamic Time Scaling

Similar to the analysis of viscous events, a time scale for inertial or dynamic events can be calculated with dimensional analysis (Ketcham and Black, 1995). An inertial force (F_i) can be defined by the product of mass and acceleration. Furthermore, the model to prototype ratio of inertial forces (K_{Fi}) can be defined with

$$K_{Fi} = \frac{F_{im}}{F_{ip}} = \frac{m_m}{m_p}\frac{a_m}{a_p} \tag{3.19}$$

In terms of dimensional analysis, acceleration has units of L/T^2, therefore the acceleration ratio can be expanded into ratios of length and time (Equation 3.20).

$$\frac{K_l}{K_t^2} = \frac{a_m}{a_p} \tag{3.20}$$

Since the same material is used in both the model and prototype at the same mass density (ρ) the scale for mass is then equal to that of volume ($1{:}N^3$), which is a cube of linear measure L. From Equations (3.19) and (3.20), the inertial force ratio becomes

$$K_{Fi} = \frac{K_l^4}{K_t^2} \tag{3.21}$$

Since the inertial force ratio K_{Fi} must equal the weight force ratio K_F as defined by Equation (3.15), K_t must therefore equal K_l. Like the geometric scale, the model to prototype time scale for inertial events is $1{:}N$.

Dynamic or inertial events with a time scale of $1{:}N$ would therefore have a velocity scale different than that of the static condition since the static condition has a time scale of $1{:}N^2$ and velocity is a function of time. Considering the dimensional units of velocity (L/T), during dynamic events with a length scale of $1/N$ and a time scale of $1/N$ the velocity scale would therefore be 1:1. This is also confirmed by analyzing the parameter of acceleration with geometric scaling for dynamic events. The acceleration parameter with scale N and linear dimensions with scale $1/N$ confirms that the velocity scale for dynamic events is 1:1. The energy produced from dynamic models has a scale of $1/N^3$, the same as mass. Table 3.2 displays the scaling laws for dynamic events.

Table 3.2 Dimensions and scaling factors for dynamic geotechnical centrifuge modelling.

Parameter	Dimensions M,L,T System	Prototype	Model
Length	L	1	1/N
Area	L^2	1	$1/N^2$
Volume	L^3	1	$1/N^3$
Mass Density	M/L^3	1	1
Mass	M	1	$1/N^3$
Gravity	L/T^2	1	N
Stress	M/LT^2	1	1
Strain	---	1	1
Time	T	1	1/N
Velocity	L/T	1	1
Frequency	1/T	1	N
Energy	ML^2/T^2	1	$1/N^3$

N = scale factor

Additional scaling laws focusing on parameters specific to various unique processes have also been investigated by modelers. Parameters relevant to cold regions experimentation such as moisture flux and heat flux have been analyzed and scaled for centrifuge modelling. Furthermore, the area of environmental geomechanics and transport processes is another area with unique modelling parameters requiring individual attention. Smith (1995) and Culligan-Hensley and Savvidou (1995) will lead one through the unique scaling laws for geotechnical cold regions investigations and environmental mass transport events, respectively.

3.3 Model Limitations

3.3.1 Time Scales

The conflict in time scales between dynamic and static events has introduced controversy amongst experimental modellers but has also brought forth techniques of manipulating the test parameters to achieve an acceptable test setup. Take for instance the case of modelling the clay-steel interface response of a friction pile during seismic activity. A prototype earthquake of a 10 second duration with a frequency of 1 Hz could be modelled in a centrifuge at 100*g* and would therefore have a duration and a frequency of 0.1 seconds and 100 Hz, respectively, based on dynamic scaling. A nominal displacement amplitude in the prototype of 0.2 m would be modelled in the centrifuge as just 2 mm. This is assuming that over the 0.1 second test duration no excess pore water pressure would dissipate, therefore the diffusion time scale would not be relevant until the dynamic event is complete. For this case the use of both time scales may be implemented without incorporating significant error, the scale of $1{:}N$ for the very short dynamic event followed by a time scale of $1{:}N^2$ for the ensuing pore pressure dissipation stage.

Time scale conflicts are created when modelling fine saturated sand and a seismic induced liquefaction event. The rapid dissipation of pore pressure does not permit the use of two time scales as in the case of clay described above. For this case it is necessary to match the time scale for motion to the time scale for fluid flow. One technique accomplishes this by decreasing the relative permeability (Darcy's) of the soil by increasing the viscosity of the pore fluid. The use of a model fluid that is N times more

viscous than the prototype, while still maintaining approximately the same density, would make the model material appear to be N times less permeable. Therefore, following Darcy's law of seepage and Equation (3.6) through (3.13), the time scale factor for diffusion ($1:N^2$) would be then be $1:N$, equivalent to the time scale for dynamic motion. But, more viscous pore fluid must not affect the effective stress response of the soil skeleton.

3.3.2 Stress Field Variance

The inertial acceleration developed in a centrifuge is dependent on the angular velocity (ω) and the radius (r) from the point of rotation. The inertial field scale is defined by

$$N = \frac{R\omega^2}{g} \tag{3.22}$$

The inertial acceleration level is directly dependent on the radius. The acceleration and stress field are constant at any point along the radial arc length while both the acceleration and model stresses increase with increasing radius. Keeping this in mind, the g level would therefore change throughout the model depth as the radius of rotation increases thereby causing a scaling error as shown in Figure 3.1. Taylor (1995) and Schofield (1980) show that there is exact correspondence in stress between the model and prototype at two thirds of the model depth. Above and below that point are under and over stresses, respectively. The analysis of stress variation and derivation of the model equivalent radius to the point of exact stress correspondence follows.

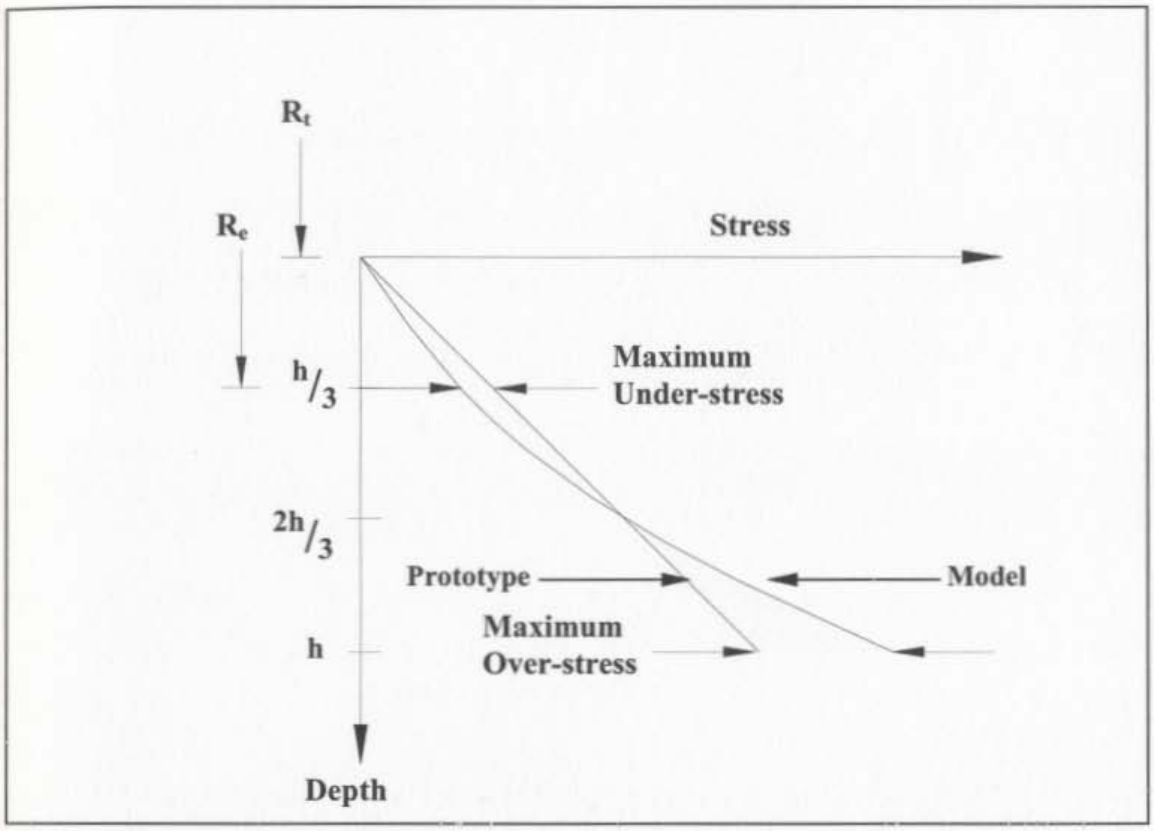

Figure 3.1 Comparison of stress variation between model and prototype with respect to model depth and radius of rotation (After Taylor, 1995; Schofield, 1980).

Considering the radius to the top of a model is R_t, at a depth z the vertical stress can be determined with

$$\sigma_{vm} = \int_0^z \rho\omega^2 (R_t + z) dz = \rho\omega^2 z \left(R_t + \frac{z}{2} \right) \qquad \textbf{(3.23)}$$

If the vertical stress in the prototype is equal to a point in the model with an effective radius of Re at a corresponding depth of $z = h_i$, then from Equations (3.1), (3.22) and (3.23) it can be shown that

$$R_e = R_t + \frac{h_i}{2} \tag{3.24}$$

To minimize the error from over and under stresses at the model's vertical extremeties, the relative magnitude of stress distribution is considered. The model to prototype ratio of under stress at the model depth of $0.5h_i$ is given by

$$r_u = \frac{0.5h_i\rho gN - 0.5h_i\rho\omega^2\left(R_t + \frac{h_i}{4}\right)}{0.5h_i\rho gN} \tag{3.25}$$

Substituting the effective radius defined in Equation (3.24) into Equation (3.25) and simplifying, yields

$$r_u = \frac{h_i}{4R_e} \tag{3.26}$$

Similarily, the computation of the model to prototype over stress ratio (r_o) found at the base of the model at distance h_m, can be shown to be

$$r_o = \frac{h_m - h_i}{2R_e} \tag{3.27}$$

Equating the two ratios to determine equivalent lengths of h yields

$$h_i = \frac{2}{3}h_m \tag{3.28}$$

Using Equation (3.24) and substituting Equation (3.27), a point for exact correspondence in stress between model and prototype can be found at

$$R_e = R_t + \frac{h_m}{3} \tag{3.29}$$

There is exact correspondence in stress between the model and prototype at two thirds of the model depth as given in Equation (3.28). Considering the magnitudes of over stress below this point and the under stresses above, the effective centrifuge radius should be measured from the central axis to one third of the model depth in order to minimize error. Consideration of the variation of acceleration with model depth should be considered upon design of the model. For example, keeping pile lengths as short as possible thereby minimizing the difference between the effective radius and the radius to either the top or bottom of the model and keeping the over and under stresses to a minimum. Schofield (1980) stated that as long as the overall soil model depth is less than 10% of the effective centrifuge radius, the acceleration level may be assumed constant with model depth without excessive error.

A centrifuge is used to simulate an exaggerated gravitational field, but this stress field is cylindrical in nature whereas many models tend to have flat surfaces. That is, the inertial radial acceleration is based around a fixed axis; therefore the radial acceleration is proportional to the effective radius. Furthermore, the acceleration is directed through the centerline of travel and therefore there is a change in the gravitational resultant direction in the model's horizontal plane across the width of the model. The resulting lateral component of acceleration may be of significance if a test activity takes place off the model's centreline. Shaping the model surface to match that of the angular path of travel can account for the radial nature of the acceleration field. As well, ensuring that the critical point of concern with regards to the test is at or near the centre of the model and

along the centrifuge centreline thereby minimizing possible variation in the gravitational field.

An unavoidable error incorporated into the stress field is the 1*g* effect. Regardless of the model scale *Ng* acting through the centrifuge centreline, there is always Earth's 1*g* acting downwards. In the case of the swinging basket-type beam centrifuge, the resultant gravitational force will always act normal to the model surface, assuming a frictionless free swinging bucket. Although the error that may be incorporated is small, and decreases with increasing scale factor *N*, the 1*g* effect is always present.

3.3.3 Coriolis Effect

Modelling dynamic events in a centrifuge can introduce the problem of the Coriolis effect (Schofield, 1980). When a mass is moved within the plane of rotation the accuracy of the prototype simulation may be compromised. This special condition can be encountered with models that involve large accelerations and velocities within the test package, such as modelling of explosions. The blast velocity of material may be equal to or exceed the angular velocity of the centrifuge. An example given by Steedman and Zeng (1995) relates this to the Earth's gravity and rotation. Imagine a long tube penetrating to the centre of the Earth. Consider if you were to drop a stone down this very long shaft and that the stone did not experience any air turbulence or friction, would the stone fall straight down the shaft? No it would not. The stone was dropped with a tangential velocity from the Earth's rotation but it is also accelerating towards the centre of the earth

by gravitational attraction and therefore a radial velocity is generated. However, the tangential velocity is constant and exceeds the radial velocity. Therefore, the stone would have a tangential velocity greater than the shaft as the stone travels downward. To the stone it would appear that the wall of the shaft had just moved towards the stone's line of travel, this is the Coriolis effect. The Coriolis acceleration (a_c) is related to the centrifuge's angular velocity (ω) by

$$a_c = 2\omega\upsilon \tag{3.30}$$

Where υ = radial velocity of the movement within the model. Putting the Coriolis acceleration in terms of radius R gives

$$a_c = \frac{\upsilon^2}{R} \tag{3.31}$$

Where $R = \upsilon/2\omega$. The inertial acceleration ($a = Ng$) in terms of model velocity (V) within centrifuge flight is defined by

$$a = \omega V \tag{3.32}$$

By comparing the Coriolis accelertion with the constant centrifugal acceleration yields the Coriolis error (Equation 3.33) as defined by Steedman and Zeng (1995).

$$\frac{a_c}{a} = \frac{2\upsilon}{V} \tag{3.33}$$

If the particle velocity is small in relation to the constant centrifugal velocity the error from the Coriolis effect may be insignificant. It is stated that by keeping the a_c less than 10% of the inertial acceleration (a), the error due to the Coriolis effect can then be

neglected (Schofield, 1980; Steedman and Zeng, 1995). That also translates to keeping the model mass velocity (υ) within the following range defined below.

$$0.05V<\upsilon<2V \tag{3.34}$$

3.3.4 Data Interpolation

A model test, whether it is conducted in a centrifuge or in a laboratory at 1g, has the need for calibration or verification of test results in order to make a comparison to the corresponding prototype. In order to ensure the data collected from a centrifuge model test is of the same nature as the prototype the technique of "modelling of models" can be employed (Schofield, 1980; Phillips, 1995; Taylor, 1995). This technique requires the modelling of a prototype in various acceleration fields with the appropriate geometric size. Since both stresses and strains are scaled at 1:1 between the model and prototype and the model dimensions scale linearly with g level, the resultant stresses will therefore be constant with g-level (Figure 3.2). In other words, since the acceleration level and the size of the model are directly related, similarity between the modelling of models is expected if significant error is not encountered. The same phenomena should be observed between model tests, which correlate to one prototype condition. The modelling of models provides a check for the modelling procedure but it should be kept in mind that it is not a guarantee that the data can be directly interpolated back to the prototype without encountering additional error.

3.3.5 Material Grain Size Effect

It has been argued that a sand in the prototype if used in the centrifuge within an accelerated gravitational field of Ng would be scaled up in size N times thereby representing a gravel in the hypothetical prototype. Based on that logic, a clay or silt within an accelerated gravitational field of a centrifuge would better represent sand in a prototype. Considering the stress/strain behaviour of clay and that of sand, this substitution is inaccurate and cannot be done. Furthermore, another important issue relating to particle size scaling is that as the particle size decreases the grain crushing

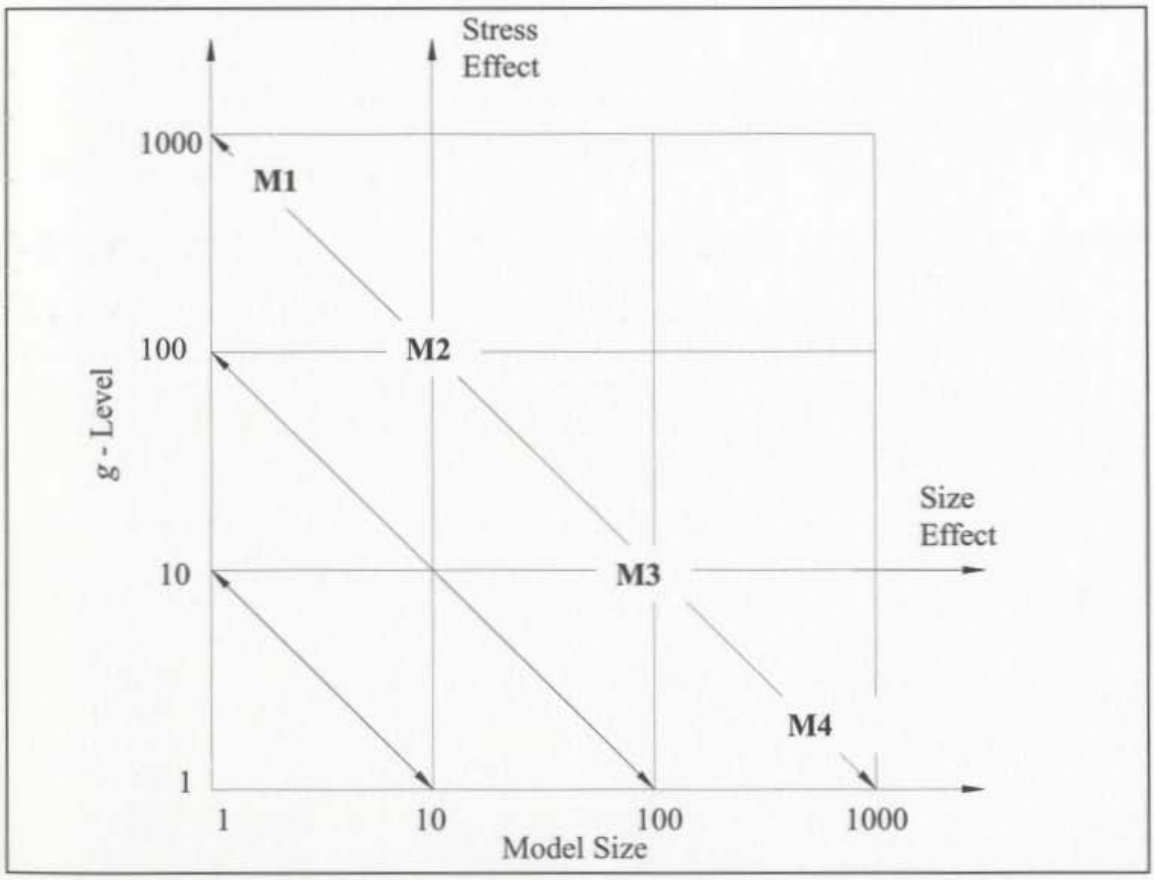

Figure 3.2 Modelling of models principle (After Ko, 1988).

resistance increases. In order to maintain consistent behavioural soil characteristics between the model and prototype it is recommended that the model material should not differ from the prototype. Accepting the fact that the material grain size is not geometrically scaled, the effects of this have to be considered. Through model testing it has been determined and generally agreed upon by several researchers (Gemperline, 1988; Bolton and Lau, 1988, 89; Bolton *et al.*, 1999) that a minimum of about 30 mean particle diameters (d_{50}) must be in contact with a linear dimension (L) of the model in order to maintain a continuous representation of foundation performance. For example, the ratio of pile diameter to the mean grain size should have a minimum value of about 30.

3.3.6 Boundary Conditions

Depending on the type of centrifuge, drum or beam type, different boundary conditions will apply. The drum centrifuge, which is essentially a spinning cylinder, has the soil contained in or spread over the walls of the rotating drum, which gives very different model boundary conditions from that of the beam type centrifuge. The beam type centrifuge must contain the model on the test platform suspended on the end of the rotating arm. This is accomplished with some kind of test container or strongbox, which introduces boundary conditions different from that of the drum type centrifuge. This section will focus on the boundary conditions encountered with a model test container and the use of a beam type centrifuge.

The boundary conditions encountered depend on many factors, some of which stem from the centrifuge limitations. The maximum acceleration obtained correlates to the maximum g level that in turn dictates the smallest geometric scale ($1:N$) that may be modelled. Furthermore, the centrifuge platform dimensions give limitations to the size of the test container that may be loaded. Therefore, the primary limitation is that of model size and how it relates to lateral, horizontal and vertical boundary conditions. To cope with the high stresses within the centrifuge the test containers or strongboxes must be rigid and strong. To maintain similitude to the prototype, the non-compliance of the test container base and side-walls must be considered. High lateral stiffness is required to prevent lateral soil movement and therefore requires a rigid boundary.

Soil settlement and consolidation processes are performed during centrifuge operation that result in soil shearing along the container walls. The friction from the strongbox walls must be limited to prevent significant boundary influence. Tests using a cohesive soil may account for wall friction by coating the walls with a waterproof lubricant. For tests with sand, the wall friction can be limited by placing a glass sheet between the model material and the container wall. To further reduce the frictional influence, a lubricated latex membrane can be placed at the soil boundary that will stretch and accommodate any vertical soil displacements (Phillips, 1995). The later approach was used by Sharp *et al.* (1998) who performed a series of CPT tests in sand. By greasing the container walls and applying a latex membrane at the container surface, the frictional arching effect seen prior to the application of the greased membrane was eliminated.

Although, the use of a grease or lubricant on boundary interfaces with frictional granular material has been reported by some experimental modellers to have little to no effect (Santamarina and Goodings, 1989). It has been shown that the model soil width to depth ratio should be greater than four to eliminate general boundary influence (Santamarina and Goodings, 1989). Proper design of the test set-up with respect to test and instrumentation locations can assist in limiting the influence from container boundaries. Testing involving any soil displacements and any measurement of soil settlement or displacement should be positioned as far away from any rigid frictional boundary as possible.

In the case of pile models or cone penetrometer tests (CPT) during centrifuge flight, three boundary conditions must be considered (Parkin and Lunne, 1982). The first condition as described in the previous section is the boundary condition of the *particle size effect,* which must be considered for such models as piles and penetrometers as the model diameters are usually quite small. A model diameter to mean particle size ratio (L/d_{50}) should exceed 30 in order to avoid modelling error. The second condition is the distance to the rigid horizontal boundary commonly put in terms of pile diameters or cone diameters. Bolton *et al.* (1999) state that a CPT must not be performed at a distance less than 10 cone diameters from any rigid boundary in order for cone data to be meaningful. Furthermore, the influence of the container diameter to cone diameter ratio was analyzed and found to have little influence on penetrometer capacities for ratios exceeding 40 and 33.6 as determined by Bolton *et al.* (1999) and Been *et al.* (1987) respectively. Axial

model pile tests performed by Rao and Krishnamurthy (1982) and Alawneh *et al.* (1998) used and recommended horizontal boundary conditions of 7 and 8 pile diameters. The third boundary condition with respect to cones and foundation elements is the test container bottom or the model depth limitation. Depending on the foundation element in question, the general rule followed by centrifuge modellers is to keep the model at least 6 to 10 model diameters or widths away from the rigid bottom surface.

CHAPTER 4

Experimental Facilities and Equipment

4.1 Geotechnical Centrifuge

The C-CORE Centrifuge Centre, located on the campus of The Memorial University of Newfoundland, houses an Acutronic 680-2 centrifuge. Commissioned in 1993, the Centre comprises a main two-level building and a separate three-level structure containing the centrifuge and mechanical components.

The main building has space for model preparation and post-test investigation. The facilities include an electrical workshop, machine shop, an X-ray bay, coldroom and the centrifuge control room. The upper level of the centrifuge containment structure houses the electrical slip-rings and provides a stiff ceiling for the centrifuge operation chamber (centre level). The centre level has an inner diameter of 13.5 m and a ceiling height of 4.2 m with 300 mm thick reinforced concrete chamber walls that retain a rockfill safety berm outside. The basement level houses the centrifuge drive unit, hydraulic actuator, refrigeration unit and the fluid rotary union (FRU).

The Acutronic 680-2 centrifuge is a beam-type centrifuge with a swinging platform as shown in Figure 4.1. With a radius of 5.5 m, it can accelerate a model to approximately

200*g* at a rotational speed of 189 rpm. The model platform is 1.4 m in length and 1.1 m in width and can accommodate a model of 1.2 m in height and upwards of 2.1 m at the mid point of the platform. The centrifuge may accommodate a payload of 0.65 tonnes at 189 rpm and up to 2.2 tonnes at a reduced speed of 134 rpm. Phillips *et al.* (1994) and Paulin (1998) give a complete description of the C-CORE Centrifuge Centre and the Acutronic 680-2 centrifuge.

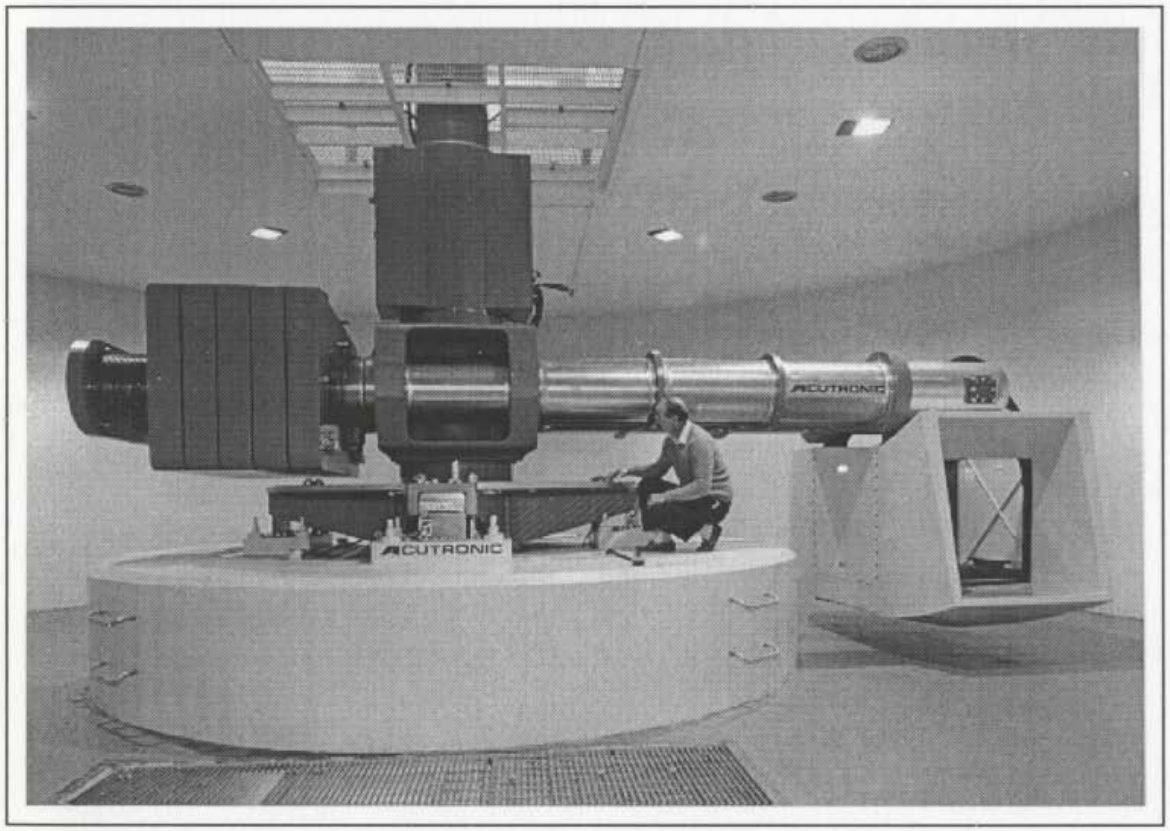

Figure 4.1 C-CORE Centrifuge Centre, Acutronic 680-2 centrifuge.

4.2 Model Design

Taking advantage of the experiences of other experimental modelers, the model design incorporated ideas from other pile model test research. Making use of the existing ancillary equipment, such as strong boxes and CPT actuators, the design was attempted to incorporate the most cost-effective route while still maintaining the predetermined operational requirements. The layout of the model test package is displayed in Figure 4.2 and will be described in detail within the following sections.

4.2.1 Pile Models

A cylindrical pile of 2 m in diameter and 15 m in length was chosen as the prototype to model in the centrifuge. In order to apply the concept of *modelling of models*, three models of varying dimensions were fabricated with the intent to represent the single prototype. Following the scaling laws derived in Section (3.2), the physical dimensions of the three pile models are given in Table 4.1 with respect to the associated g-level to properly represent the prototype condition.

Table 4.1 Prototype pile and pile model dimensions.

Pile	Diameter	Length	Wall Thickness	g-Level (N)
Pile 1	30	225	1.05	66.7
Pile 2	35	263	1.23	57
Pile 3	40	300	1.4	50
Prototype	2,000	15,000	70	1

units = mm

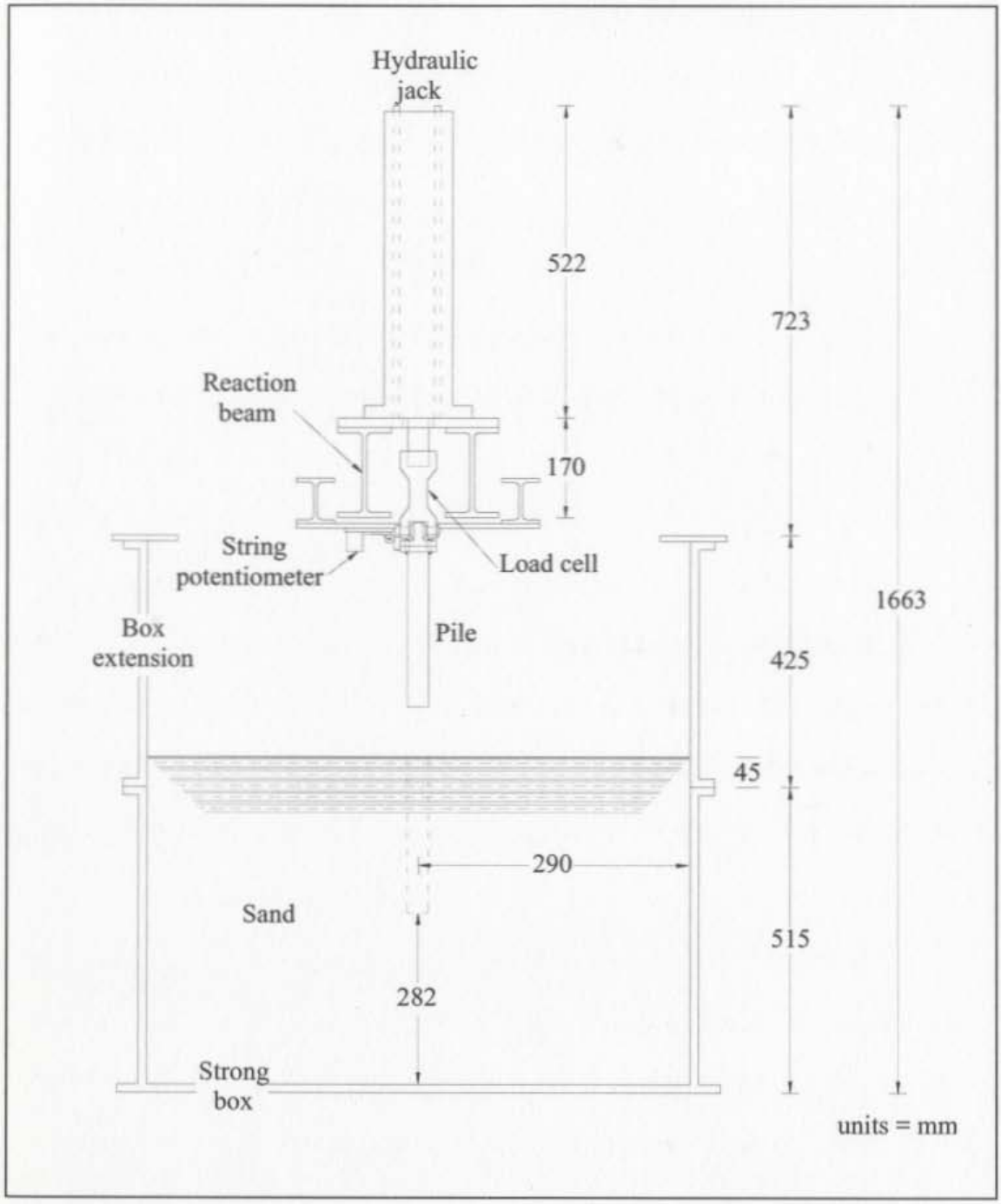

Figure 4.2 General schematic of the pile model test package, Pile 2 shown.

The prototype pile and the pile models are relatively short and all have a *L/b* ratio of 7.5. The wall thickness of all the models properly scale the prototype to give the ability to consider the Poisson's effect presented by De Nicola and Randolph (1993).

The pile models had a surface roughness of 4.6 μm and were constructed of standard mild steel at the Technical Services machine shop of the Memorial University of Newfoundland. In order to isolate the pile shaft resistance of the pile models, both the total capacity and the end bearing capacity were recorded. To accomplish this task the design called for an inner rod to be placed within the centre of the pipe pile body that would be used to transmit the end bearing load to the pile head, independent of the pile shaft. An end cap at the pile toe was bolted to a load cell, which in turn was threaded into the inner rod as shown in Figure 4.3. A small gap between the end bearing cap and the pile shaft filled with a pliable silicone kept the pile end cap independent of the shaft. The silicone was used to seal the pile end and not permit grains of sand to enter the space between the end cap and shaft that would result in end bearing load being transferred to the shaft. Post-test analysis of the model revealed that this technique was effective, as it was for Latotzke *et al.* (1998). To keep the inner pile assembly in position and free of the outer pile shaft, the end cap was machined to accommodate a standard O-ring. This O-ring ensured a rubber to metal contact between the inner and outer pile components. The O-ring was coated with common automotive grease to limit the friction at the mating surface. To check if this connection would lock in a measurable stress on the end bearing load cell or transmit end bearing load to the shaft, a load cell coupling check was

periodically performed throughout the test series. The check involved applying a series of known tensile and compressive loads to the complete pile assembly while observing the load cell response to determine the magnitude of load carried by the O-ring seal. It was determined that the O-ring connection would lock in about 10 N in either the tensile or compressive loading direction once the applied load was removed. The smallest anticipated pile shaft capacities were about 1 kN thereby resulting in a potential error of no more than 1%.

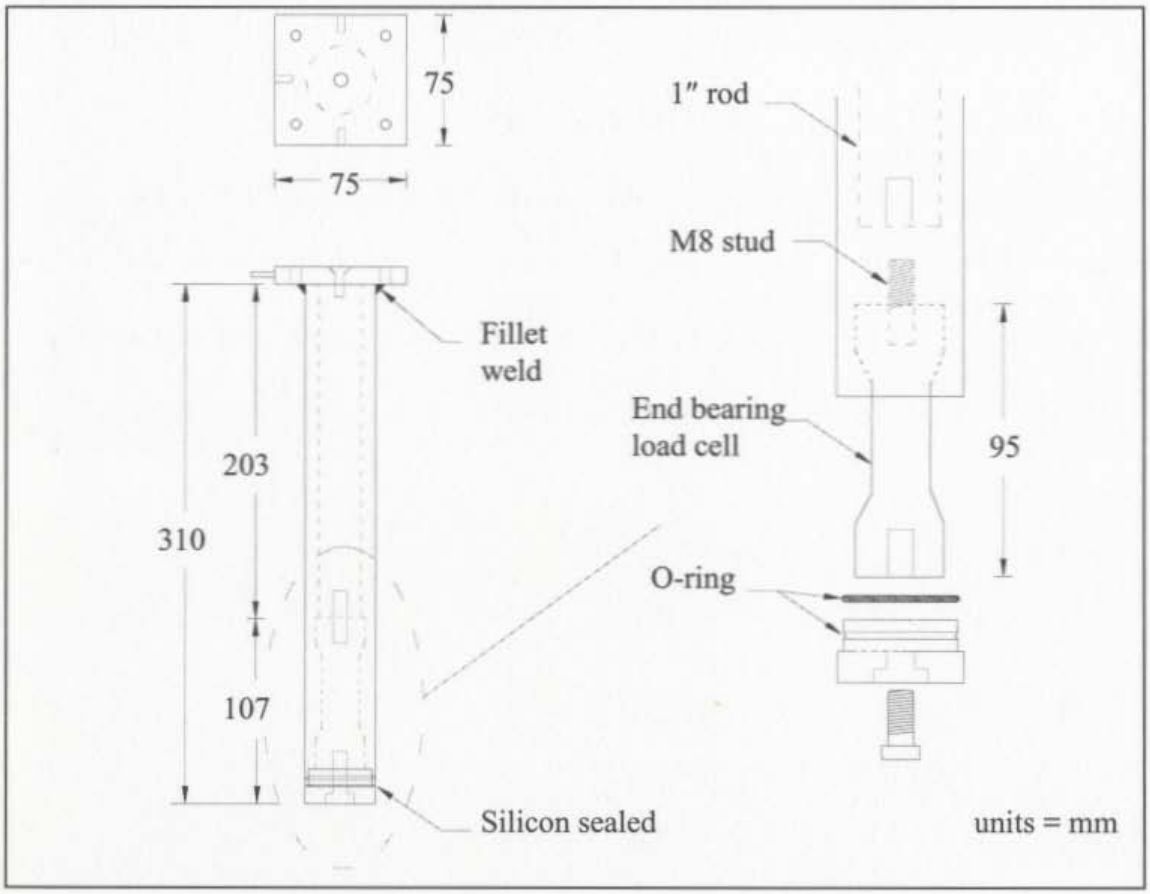

Figure 4.3 Typical design layout of pile models, Pile 3 shown.

Using conventional foundation design theory, the expected capacities of the pile models was estimated. With this information the models were designed to safely accommodate such loads. The bearing stresses and unit factored compressive resistance considering slenderness was computed for the pile shafts and the inner rods that are required to transmit the large end bearing loads to the pile head.

The pile head was mated to a load cell measuring the total pile capacity. In turn, the load cell was fixed to a 92.5 kN capacity hydraulic cylinder that was used for pile loading. Two pile head fixities were used throughout the study. The initial head fixity chosen was a free rotating ball joint type much like the pile model tests performed by Rezende *et al.* (1998). The free rotating pile head fixity proved to be troublesome. To increase test repeatability, the second fixity used in the study was a simple rigid vertical connection. The ball joint was removed and the pile was bolted directly to the load cell, which in turn was fixed directly to the hydraulic actuator. Both pile head fixities are shown in Figure 4.4.

4.2.2 Soil Model

The soil used in the modelling study was dry fine silica sand. Conventional laboratory tests were conducted to determine the material's physical properties. Purchased from Shaw Resources in Nova Scotia, the #00 Alwhite silica sand had little fines and a specific gravity of 2.65, a maximum void ratio of 1.06, a minimum void ratio of 0.65 and a mean grain size of 0.32 mm and is uniformly graded. The physical and chemical properties of

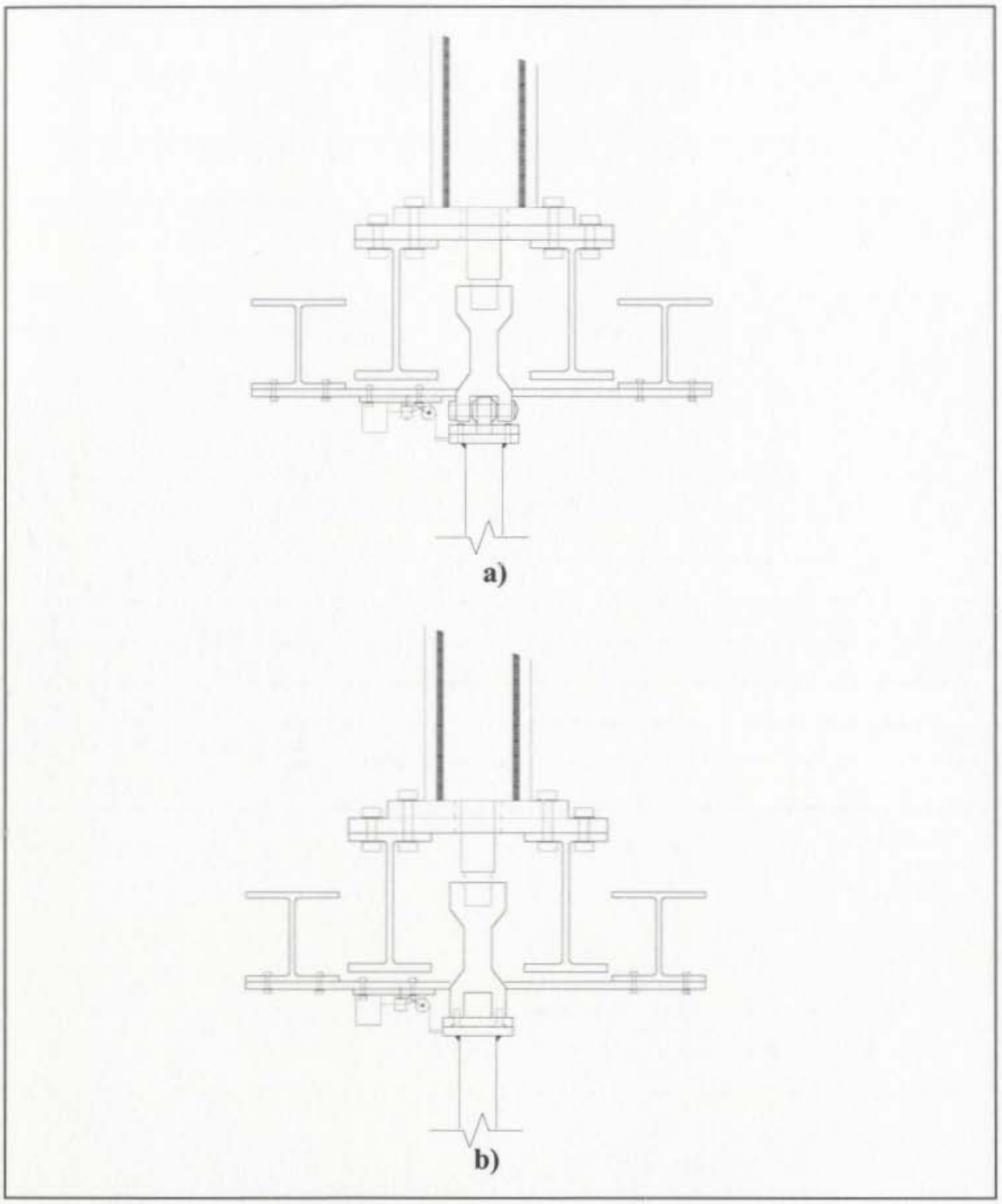

Figure 4.4 Pile head fixities; a) free rotating ball joint, b) rigid connection.

the modelling sand are summarized in Table 4.2 and the material grain size distribution is shown in Figure 4.5. Used by many researchers at C-CORE (Zhu 1998; Phillips *et al.* 2000) it is a material of known properties and predictable behaviour lending itself well to known initial test conditions.

Table 4.2 Physical and chemical properties of #00 Alwhite silica sand.

Physical Parameter:	**Unit**	**Value**
Specific gravity, *Gs*:	1	2.65
Maximum dry unit weight, γ_{max}:	kN/m^3	15.8
Minimum dry unit weight, γ_{min}:	kN/m^3	12.7
Maximum void ratio, e_{max}:	1	1.06
Minimum void ratio, e_{min}:	1	0.65
Effective grain size, d_{10}:	mm	0.18
Mean grain size, d_{50}:	mm	0.32
Uniformity coefficient, C_u:	1	2.06
MoH hardness	1	7
Chemical Composition:		
SiO_2	%	98 to 98.6
TiO_2	%	0.4
Fe_2O_3	%	0.35
LiO	%	0.3
Al_2O_3	%	0.15
CaO	%	0.1
MgO	%	0.04

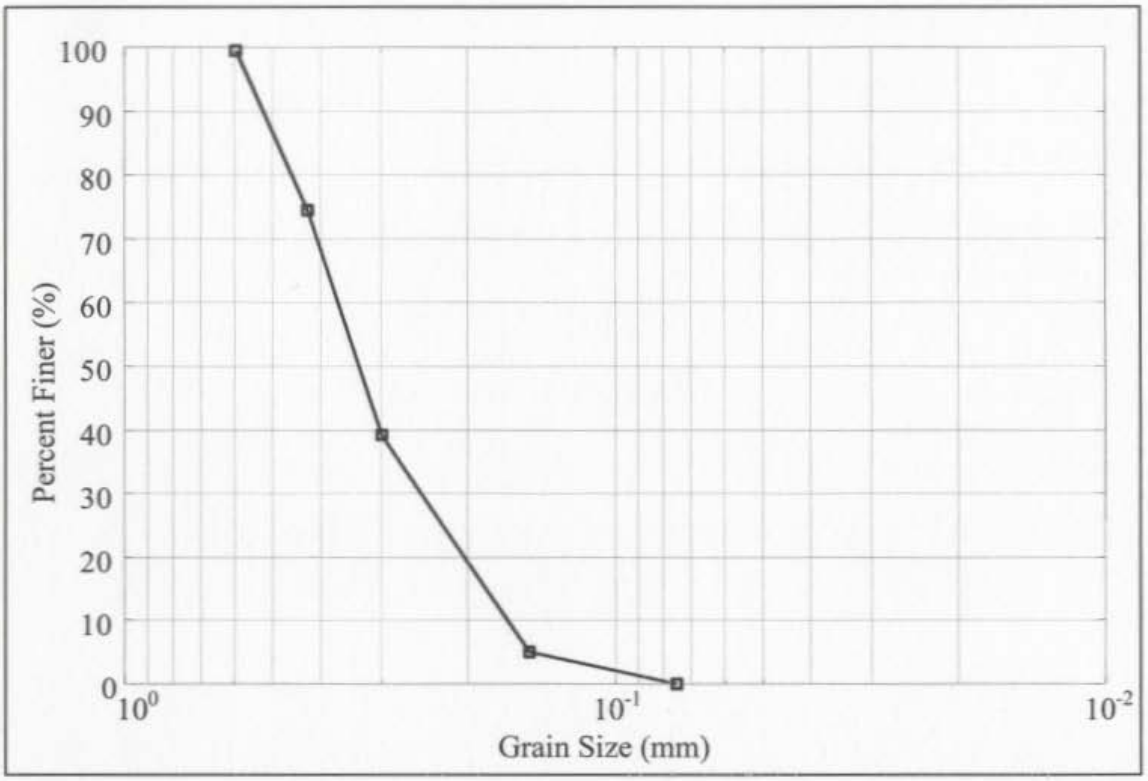

Figure 4.5 Grain size distribution of #00 Alwhite silica sand.

The modelling sand is manufactured through a crushing process and therefore the grain shape is generally fragmented and angular. Furthermore, the modelling sand particles are bulky or spherical in nature with the absence of flattened or elongated particles. For this reason, the modelling sand would not be subject to orientation of elongated particles at the sand-pile interface, which would affect the pile shaft frictional response to load reversals. Sand composed of fragmented bulky grains will reveal dilative shear response and therefore reveal the effects of OCR, which is a good representation of common *in-situ* conditions.

The internal angle of friction (ϕ) is known to decrease with increasing stress level as reported by Bolton (1986). Determined from triaxial tests, Zhu (1998) gives functions defining the modelling sand internal friction angle with respect to principal stress level (confining stress from triaxial tests) for both peak and critical state

$$\phi_{max} = 53.6 - 4.78 log_{10}\sigma_3 \quad (4.1)$$

$$\phi_{cs} = 45.8 - 4.09 log_{10}\sigma_3 \quad (4.2)$$

Where ϕ_{max} = peak internal friction angle, ϕ_{cs} = critical state internal friction angle, and σ_3 = principal stress level.

4.2.3 Instrumentation

All the model instrumentation is monitored from the centrifuge control room. Data acquisition is performed using a PC based data acquisition system. Amplification, transducer excitation voltage, and filtering are provided using a custom designed signal-conditioning system. Transducer signals are digitized with a 16-bit data acquisition board operating through Windows based data acquisition software called Snapmaster. Phillips *et al.* (1994) and Paulin (1998) report in greater depth the details and specifications, with respect to the data acquisition and signal processing capabilities, of the C-CORE Centrifuge Centre.

Pile displacement was measured using rotary string potentiometers. For the pile tests with a free rotating head fixity, three string potentiometers were required to measure both the vertical displacement and the pile inclination off vertical if required. Two string

potentiometers were used for the tests with rigid connection head fixity, with only one actually required and the second acting as a redundant instrument. In all cases the string potentiometers were mounted on beams independent of the pile load reaction beams as shown in Figure 4.2. Therefore beam flexure due to pile resistance was not interpreted as pile displacement. The potentiometers have a linear measurement range up to 1270 mm and were used to measure both the pile installation displacement and the cyclic displacement during the displacement controlled pile loading. In order to accurately measure both displacement processes, the string potentiometers each utilized two channels for data acquisition. With a signal gain or amplification of one, the first channel was used to monitor the pile installation displacement. The second channel was used to view a much smaller displacement window required to measure the cyclic displacements after the pile was installed to depth. Therefore the electronic zero was manually set to the pile installation depth. Furthermore, the signal gain was set to 100 and subsequently enhanced the displacement signal by 100 times greater than the primary channel recording the pile installation. With a signal gain of 100, the very small cyclic displacements could be monitored accurately. Each string potentiometer was recalibrated periodically throughout the test series.

The pile loads were monitored with a set of custom designed load cells. A load cell was mounted at the pile head to record the total resistance and a second load cell was placed within the base of each pile model to measure the end bearing resistance. As shown in Figure 4.3, the end bearing load was transmitted to the head of the pile with a solid inner

rod made of mild steel. Two end bearing load cells were fabricated, one entirely dedicated to Pile 3 and the second shared between Piles 1 and 2. The load cells were milled from 6061 aluminum alloy stock and each were outfitted with a full-bridge 90° rosette strain gauge layout. Four active gauges were placed in the uniaxial stress field, two aligned with the maximum principal strain and two Poisson's gauges. Each load cell was loaded axially to about 1200 micro strain in a calibrated press to derive a loading constant. This calibration procedure was performed periodically throughout the test series to ensure the accuracy of the data collected.

Sand surface settlement was expected during centrifuge spinup and this fact was incorporated into the model design. A single linearly variable differential transformer (LVDT) with a range of 25 mm was installed and aligned vertically with the sand bed at the model centrepoint. The LVDT and mounting assembly were supported by the same beams used to carry the string potentiometers and was therefore independent of the pile reaction beams. Surface settlements could then be recorded during each test set.

To determine the strength profile and uniformity of the sand bed within the increased gravitational field during centrifuge operation, a series of in-flight cone penetrometer tests (CPT) were performed. A custom designed vertical actuator used to perform the cone penetrometer tests was mounted on the same reaction beams as the pile and hydraulic cylinder. The penetrometer was outfitted with a load cell within the tip enabling measurement of tip resistance. The penetrometer was made of stainless steel and had a

diameter of 11.2 mm with a 60° cone tip. Cone penetration rates were kept constant at 3 mm/s over a penetration depth of 300 mm. The vertical actuator was powered by a DC stepper motor and was controlled with a PC interface using Motion Dynamics software.

4.3 Hydraulic System

Due to the large reaction loads expected during pile installation and compressive loading, direct vertical actuation with an electric gear driven actuator or pneumatic cylinder did not appear feasible. Therefore the application of hydraulic actuation was investigated and implemented. Since the C-CORE centrifuge was already outfitted with a fluid rotary union (FRU) with two vacant high-pressure ports, hydraulic pressure could then be routed to the centrifuge platform without extensive modification.

4.3.1 Closed Circuit Hydraulic Loop

A closed circuit hydraulic loop was chosen for reasons of simplicity and strain rate control in the high gravitational field on the centrifuge platform during operation. The system includes two identical hydraulic cylinders at either end of the closed loop, a master and a slave. Purchased from Tube Craft Atlantic Ltd. the hydraulic cylinders were Parker series J2 HD with a nominal operating pressure of 2500 psi (17.2 MPa). With a bore diameter of 82.6 mm and a stroke of 343 mm, the cylinders each have a maximum capacity of 92.6 kN. A set of remotely operated 2-way valves, a pair of pressure relief valves and a hydraulic recharge reservoir are placed near the master cylinder. A 4-valve assembly is plumbed into the hydraulic lines for manual de-airing of the closed loop

circuit at the high point of the system. External connections to the hydraulic circuit at either the centrifuge platform or the de-airing valve assembly are done with high-pressure quick release couplings in order to limit the potential of air being introduced into the system. An actuation ratio of about 85% was achieved between the master and slave. The 85% displacement efficiency rate was due to the great length of the closed loop, hose compliance and compression of entrapped air within the hydraulic fluid. A schematic of the closed loop hydraulic system is given in Figure 4.6.

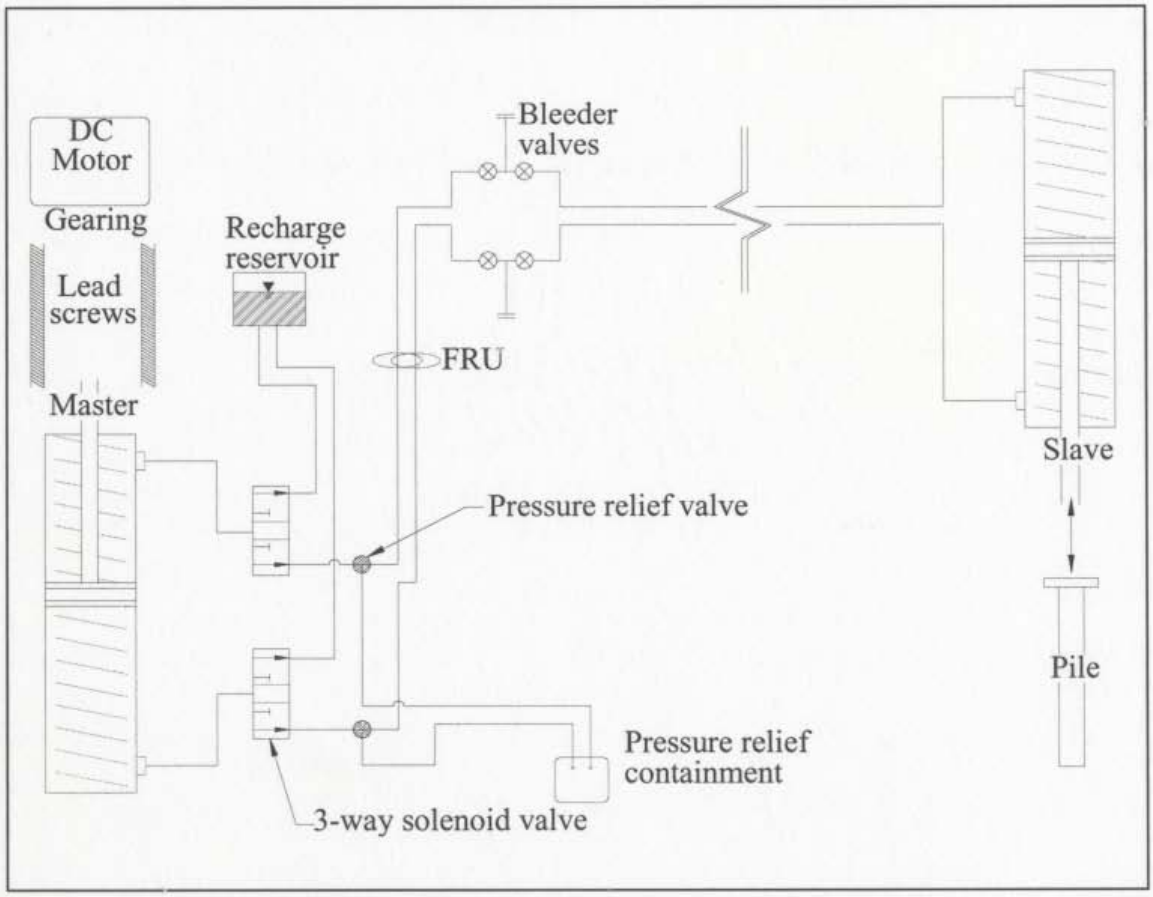

Figure 4.6 Closed loop hydraulic system.

4.3.2 Hydraulic Actuator

To achieve a closed loop hydraulic system both a master and slave cylinder are required. The master cylinder must either be depressed or pulled to actuate the slave. To accomplish this, the master cylinder was bolted to a rigid reaction box constructed of $^3/_8$ (9.5mm) and $^1/_2$" (12.7mm) steel plates. The master cylinder was bolted to one end of the rigid steel box, at the other end was a $^1/_2$ Hp 90 V DC Dayton gear motor with a set of 2 $^1/_2$ to 1 reduction gears. As shown in Figure 4.7, the motor and gear assembly turn a pair of 20 mm diameter steel loading rods machined with acme threads at a pitch of 6 threads per inch (25.4mm). The loading rods travel through a steel block outfitted with brass bushings and are carried by a set of thrust bearings at either end of the box. The master cylinder is threaded into the steel block at the centrepoint and is actuated by operation of the gear motor.

Remote operation of the hydraulic actuator from the centrifuge control room was accomplished with a custom designed DC voltage controller. Directional operation of the motor is accomplished by reversing the DC current at the control box. Varying the magnitude of the DC voltage supply enables one to control the motor speed. A slide potentiometer mounted on top of the hydraulic actuator enabled the displacement of the hydraulic actuator and the steel loading block to be observed through the data acquisition software. As a safety precaution, limit switches were mounted on either end of the rigid box. The electric motor or gearing would be overloaded if the loading block were to travel too far to one extreme and make contact with the steel bulkhead, therefore a limit

switch on either end of the box was installed that if tripped would cut off power to the drive motor. Furthermore, as a last measure an 8 amp fuse was placed inline between the motor and power supply control box.

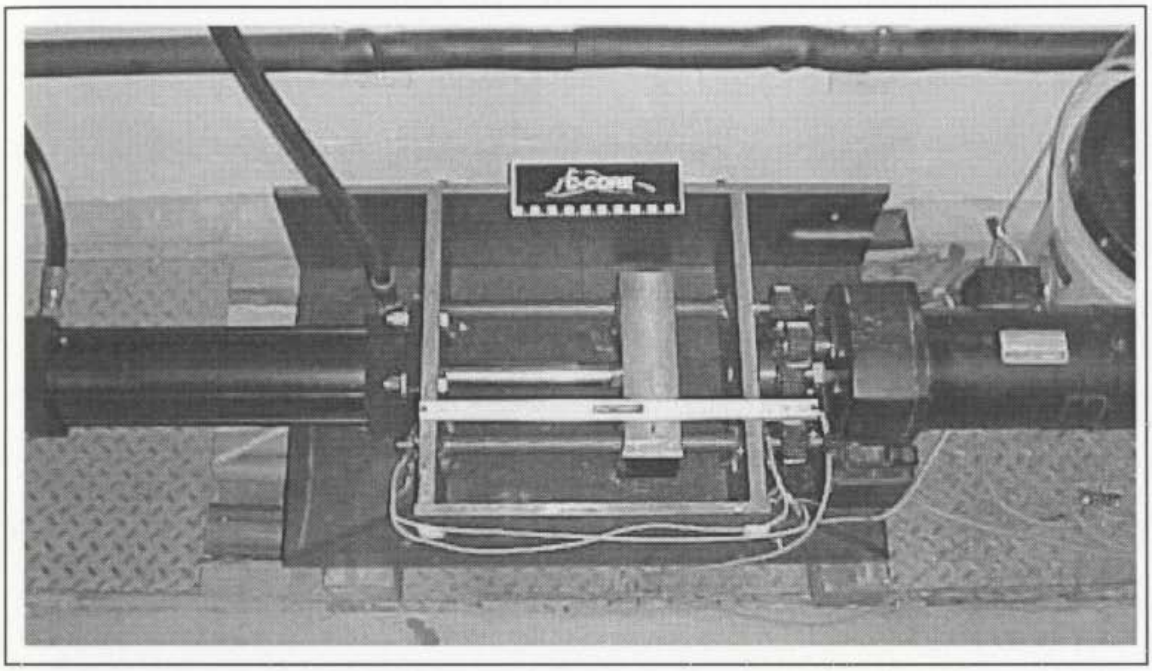

Figure 4.7 DC powered hydraulic actuator.

CHAPTER 5

Experimental Test Procedure

5.1 Introduction

To properly perform the centrifuge pile model tests all aspects and properties of the modelling soil and the interaction with the steel pile model should be considered. Aside from the data collected during each test series, corresponding data was collected during model assembly and complementary laboratory tests. Relative density measurements were taken during the preparation of the soil model and a series of standard direct shear interface tests were performed to determine the volumetric behaviour and interface friction angles of the modelling sand.

To verify the centrifuge model data the physical modelling principle *modelling of models* was followed, as described in Section 3.3.4. Three pile models were tested at varying *g*-levels to correspond to one prototype condition, a total of 15 pile tests were performed. To verify test consistency and repeatability, chosen pile tests were repeated.

5.2 Direct Shear Interface Tests

The interface friction angle between a cohesionless soil and a smooth steel surface is known to be less than the soil's internal angle of friction. The interface friction angle may

be experimentally determined with a modified version of the standard direct shear test by removing the lower half of the shear box and replacing it with a steel surface as shown in Figure 5.1. The steel surface should be of the same material and roughness as the pile shaft to properly model the soil-pile interface. The surface roughness of the pile models and the steel plate were determined with a Mitutoyo Surftest 301 surface roughness meter. The surface roughness was taken as the maximum peak-to-valley height over both the longitudinal and horizontal direction with respect to the primary shear direction and for all three pile models averaged 4.3 μm. The surface roughness of the steel block used in direct shear tests averaged 4.1 μm.

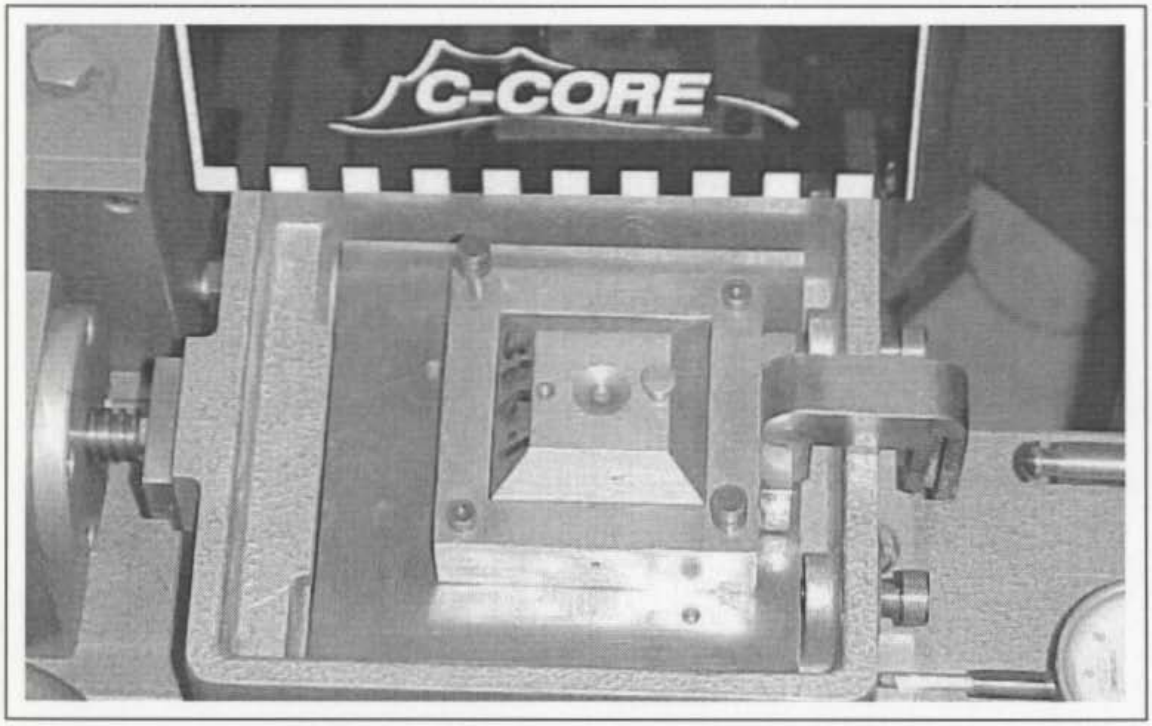

Figure 5.1 Standard direct shear interface apparatus.

The direct shear box was secured to the steel block and by means of dry pluviation, the sand was rained into the direct shear box. A sand hopper with a shutter/diffuser assembly attached beneath was used for the sand raining (pluviation) process. The sand was rained through a circular shutter of 26 cm in diameter. The shutter was outfitted with 13 evenly spaced 4.0 mm diameter apertures. Three sieves beneath the shutter acted as a diffuser. From top to bottom, the sieves used were No. 10, No. 14 and No. 18 standard sieves with apertures of 2.00, 1.40 and 1.00 mm respectively. The height between the shutter and the top sieve was 100 mm with a 50 mm gap between the two adjacent sieve meshes. To achieve optimum diffusing results, the mesh between each sieve was turned 45° from adjacent sieves. The shutter and sieves were positioned vertically during the sand raining process with a constant falling height of 250 mm from the bottom sieve to the sample surface.

A series of density checks were performed by raining the material into a calibration container. The containers of a known volume (100 cm^3) were removed and weighed to determine the density index achieved based on the maximum and minimum unit weights of the material. This process was performed prior to direct shear testing to calibrate the required falling height and material flow rate to obtain the desired relative density. The average relative densities (I_D) obtained were about 78 % and match the range of densities (70 – 80%, see Figure 5.3) used in the centrifuge soil models.

Shear tests followed ASTM D 3080-90 standards as presented by Bowles (1992) and involved shearing the sand samples under normal stresses (σ_n) of 25, 40 and 60 kPa. A total of 8 cyclic tests were performed. Shearing was performed with a standard manually operated direct shear apparatus manufactured by Wykeham Farrance Engineering Ltd. Under dry conditions and at a constant shear rate of 0.14 mm/min, the sample was sheared over a horizontal distance of 1.4 mm while monitoring the vertical displacement and the applied horizontal load. To complete an individual test, a total of 9 load reversals were executed. The cyclic testing or load reversals were applied to determine the interface friction angles in both directions. The forward or initial direction of shearing would represent the primary or compressive direction of pile loading. Conversely, shearing in the reverse direction would then represent the tensile pile condition. The cyclic shearing process continued over 9 load reversals to obtain the residual state and measure the constant volume interface friction angles (δ_{cv}) in both directions.

5.3 Centrifuge Model Preparation

The C-CORE Centrifuge Centre has a room dedicated to sand raining where the modelling sand was placed into a circular strong box by means of dry pluviation. As shown in Figure 5.2, the test container was placed under a tubular steel frame outfitted with a reciprocating sand hopper. The sand hopper travels along the rails and empties the contents into the strong box at the predetermined rate. The sand flow rate is controlled by manipulating the position of the gate valve type opening at the bottom of the hopper. Furthermore, the horizontal displacements, velocities, accelerations and number of

operational cycles of the hopper are all controlled with a PC interface and the PCMC motion controller software. A timing belt and sprocket combination powered by an electric motor moves the hopper horizontally along a pair of rails. Produced by Japan Servo co Ltd, the DC stepper motor type KP8M2FP-001 enabled precise control of the hopper displacement, velocity, acceleration and deceleration.

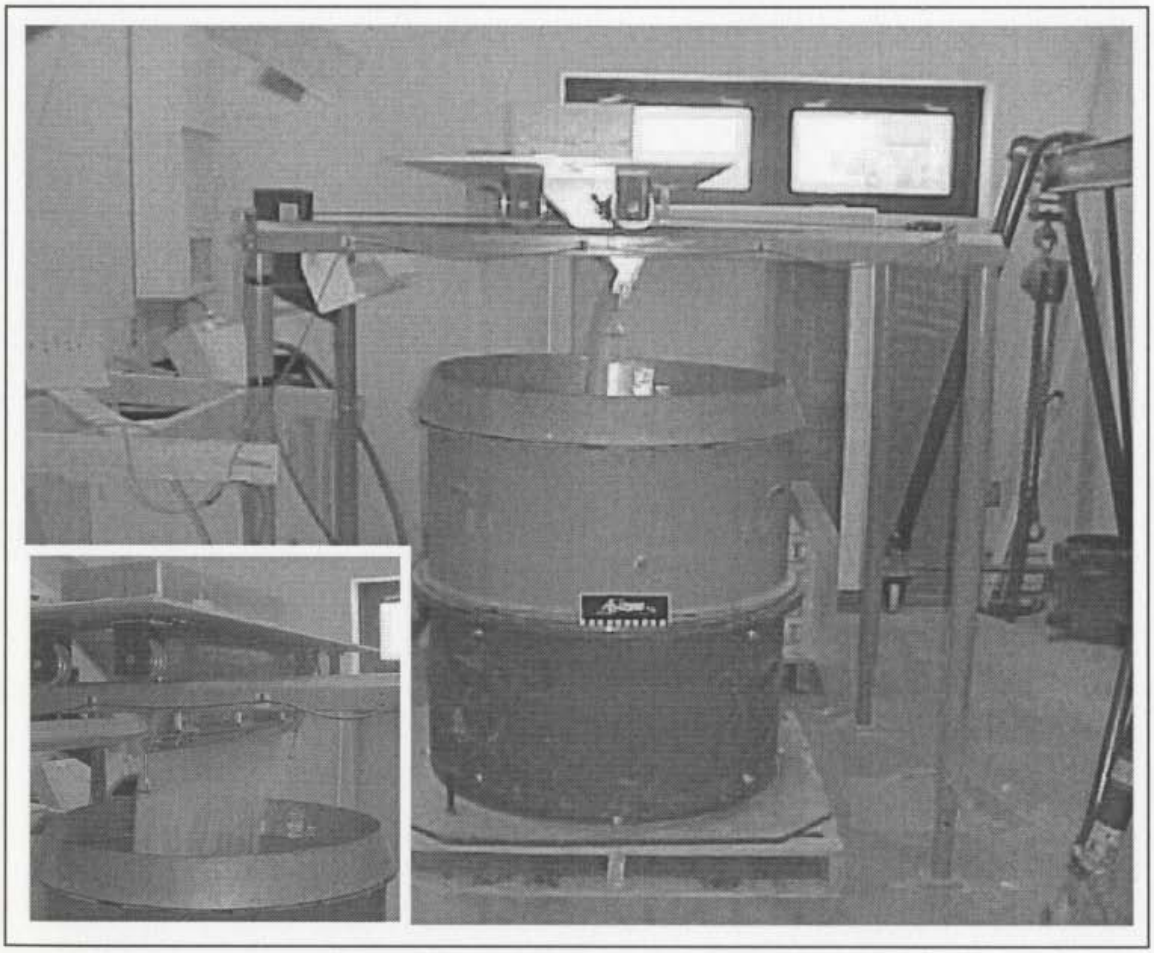

Figure 5.2 Sand raining equipment.

The test container was outfitted with a metal cutting edge on the upper most box edge to limit the boundary influence on the pluviating sand grains. To obtain a homogeneous sand density profile constant sand falling height should be maintained, but the elevation of the strong box was not altered throughout the pluviation process. Pluviating at heights greater than the terminal velocity height should result in uniform sand densities. The terminal velocity height was determined to be about 500 mm for #00 Alwhite silica sand (Zhu, 1998). The falling height for the setup shown in Figure 5.2 ranged from 1270 mm initially and terminated at 725 mm after achieving the final depth of sand. Possibly due to rigid boundary effects and an air current generated from the hopper movements, slight density variations were detected for falling heights well beyond 500 mm. It is believed that the sand particles were not able to achieve terminal velocity and were therefore affected by variance in falling height. Determined from density cups placed in the model during material placement, the relative densities achieved over three separate test beds are plotted with sand depth in Figure 5.3 and reveals an average relative density of 71 % at the model surface and 81% at the model base.

The sand was deposited about 20 to 30 mm thicker than the test design level. The excess surface sand was removed with a vacuum with a precision nozzle guided by a pair of reference beams to achieve the desired surface level. The initial thickness of the sand samples for all tests was 545 mm.

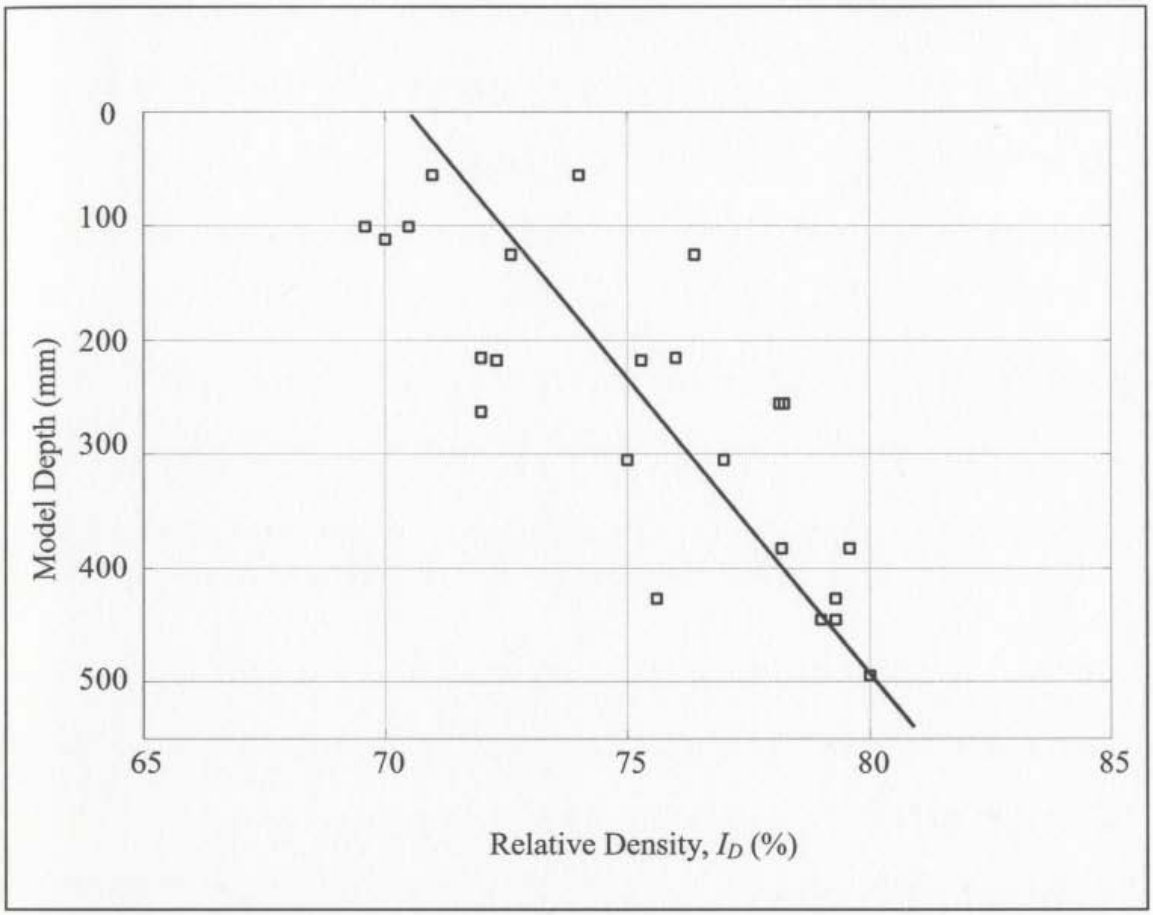

Figure 5.3 Sand model relative density profile.

5.4 Model Testing Procedure

During the initial centrifuge spinup of an undisturbed test bed, settlement of the sand sample is expected. A common practice employed to accommodate such settlements is to cycle or vary the centripetal velocity between the operational test speed and some lower speed, which corresponds to cyclic *1-D* compression. Rezende *et al.* (1998) stated that a minimum of three cycles must always be performed before installing the pile to eliminate sand settlement effects. After three cycles the settlements had stabilized.

The rigid steel circular strong box containing the soil model had an inner diameter of 900 mm with a final sand depth of 545 mm. Piles were installed at three locations within each test sample. With every pile installation a cone penetrometer test was implemented. The CPT actuator was located on the opposite end of the same beam assembly as the hydraulic pile actuator. When the first test set was completed, the beam assembly was rotated 120° to position the pile and cone penetrometer over an undisturbed portion of the sand bed for the second test set of the series. Upon completion of test set two, the beam assembly was again rotated another 120° to the third test position as shown in Figure 5.4.

The notation used to distinguish the separate pile tests and associated cone penetrometer tests follows; the first sand model bed prepared for testing Pile 1 is noted as test series Pile 1A, whereas the second sand model bed is test series Pile 1B. The same logic is followed for Pile 2 and Pile 3 test series. Within each test series are three individual pile and cone tests, labeled as test sets. The first pile test of a given series is denoted by the series title followed by a dash and set number, one through three. The same notation is followed for the associated cone penetrometer tests.

The rigid boundary conditions are the most critical for Pile 3, the largest pile tested. For Pile 3 with an outer diameter of 40 mm, the distance from the pile toe to the bottom of the model container was 6.1 pile diameters and the horizontal distance to any rigid boundary was 6.75 pile diameters. For Pile 1, the smallest pile of the test group, vertical and horizontal distances were 10.7 and 9.2 pile diameters, respectively. The recommendations

of the imposed rigid boundary conditions given in Section 3.3.6 state that a minimum of 6 pile diameters should exist between the pile toe and the container bottom and at least 7 diameters to the rigid horizontal boundary of the test container walls. Piles 1 and 2 pass the boundary limit criteria while Pile 3 is at the recommended limit and may be influenced by the boundaries imposed by the test container.

With the centrifuge operating at test speed and the pile hanging free in the air, the pile was jacked into the sand bed at a rate of 0.66 mm/sec. After about two thirds of the pile length had penetrated, the jacking process was halted to allow the master hydraulic actuator to recharge and complete the pile installation. When the pile was jacked into the final position the total measurable load was removed prior to initiating the first load cycle. During the first load cycle a compressive displacement of 3 mm was applied. After the compressive displacement, the pile was left in position for about 45 seconds prior to initiation of the first load reversal. The tensile load was applied and limited to an upward vertical displacement of 3 mm above the original jacking depth. In total, 40 load reversals were applied within the same displacement window, with 45 second pauses between load applications and at an average loading rate of 0.2 mm/sec. For each pile test, a cone penetration test was performed once the 40 load reversals were completed. Each cone test had a constant penetration rate of 3 mm/sec and a penetration depth of 300 mm.

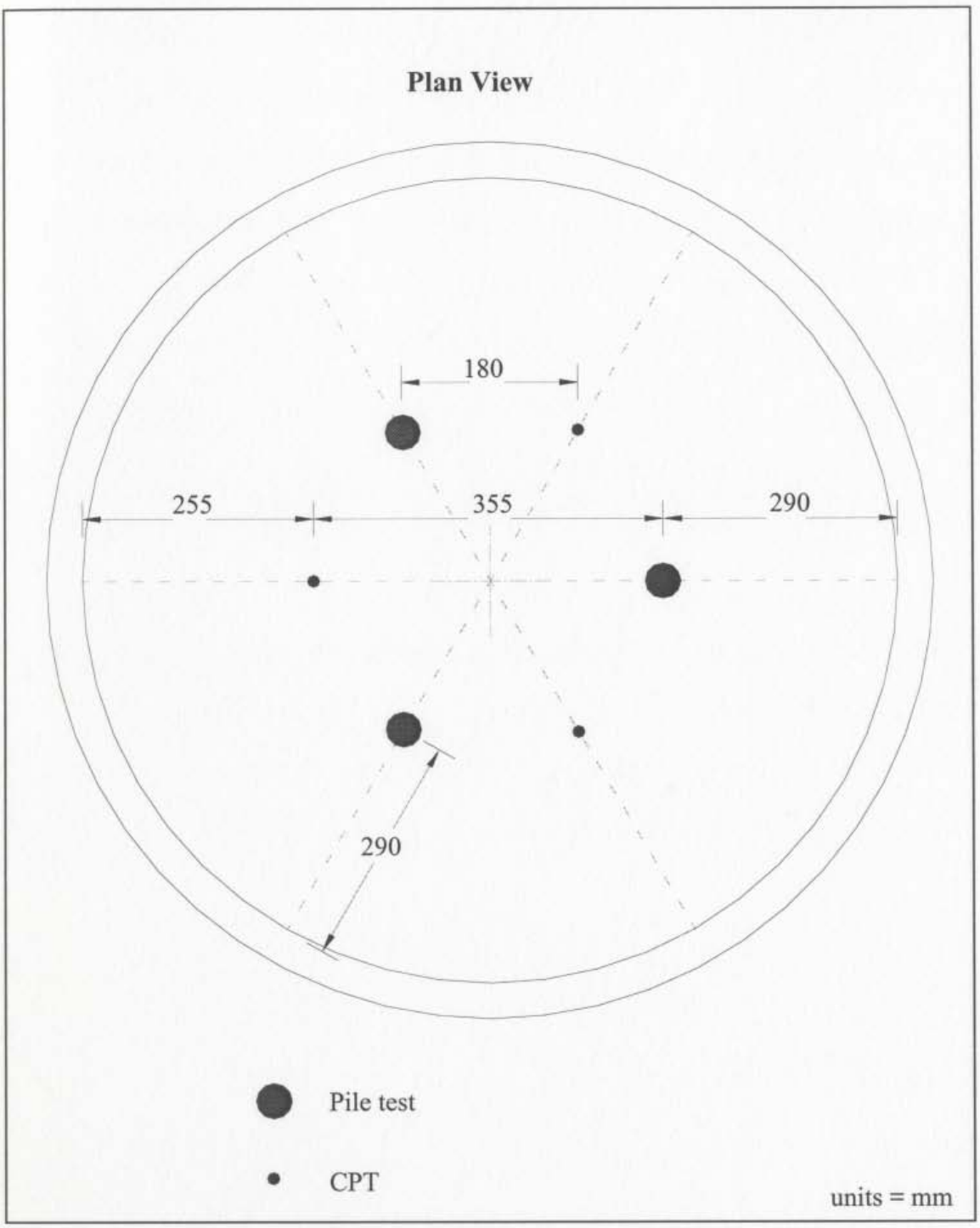

Figure 5.4 Model test locations.

Some small forms of modelling error have been incorporated into the model design and test procedure. The data acquisition system (DAS) zero points for the pile load cells were taken when the centrifuge was at operational test speed and the pile was hanging free above the sand surface. This was a convenient point to accept as the point of zero load, but this position of zero point theoretically does not yield the same zero value as the final test position when the pile is at depth. The gravitational field in the centrifuge model increases with the effective radius of rotation and the square of the angular velocity. Since the end bearing load cell is of little mass, the influence of effective radius would be minimal whereas the total pile capacity load cell is larger and supports the entire pile assembly. The amount of zero point error incurred on the total pile capacity load cell for the Pile 3 test series translates to about 58 N. The total error for Pile 1 is about 68 N. Pile 1 is smaller and was expected to yield much smaller loads and therefore was considered the critical condition for load cell error due to changes in effective radius. Based on the minimum expected static shaft capacity, the errors equate to 4.8% and 2% for Piles 1 and 3 respectively.

Test locations off the centreline axis of rotation will result in a lateral component of the stress field and an extra lateral force on the pile. Pile tests were performed in locations up to 160 mm off the centreline axis of rotation. Therefore, the maximum lateral component of the stress field is less than $2g$ for all pile tests.

5.5 Post-Test Investigation

In a post-test examination of the model, the pile inclination off vertical and material orientation at the sand-pile interface were identified. For pile tests with a free rotating head fixity the pile inclination off vertical was recorded in-flight by orienting three string potentiometers in the centres on three of the sides of the pile head. Post-test examination of inclination confirmed what was already recorded through the data acquisition system.

During excavation of the test material sand grain crushing at the sand-pile interface was recognized, which most likely occurred due to the high end bearing stresses experienced during pile jacking. The fine crushed sand at each test location was collected for further analysis.

An attempt was made to collect an undisturbed sand sample from the sand-pile interface. After the third test set of series Pile 1B was completed, the pile was left in the sand bed. The sand surface was then covered with geotextile and the perimeter was sealed with just the pile head exposed. The upper portion of the strong box was then filled up with sand until the box was entirely full. A plywood cover was bolted to the top of the strong box enclosing the model and overburden material. The plywood cover had two removable slats positioned directly above and to one side of the in-place pile. The strong box was then positioned on its side such that the slats could be removed. With the strong box on its side, excavation of the overburden to the point of the model surface could be undertaken. The modelling sand was excavated along the length of the pile at a distance

of about 50 mm from the pile surface. A hardening solution was applied to the sand along the pile length. The pile could then be removed from the model with an undisturbed sand sample attached along the length of the pile, as shown in Figure 5.5. The pile was cut horizontally and longitudinally to prepare thin sections from both axes. The thin sections were viewed under a microscope in order to identify the amount of particle crushing and particle orientation along the interface.

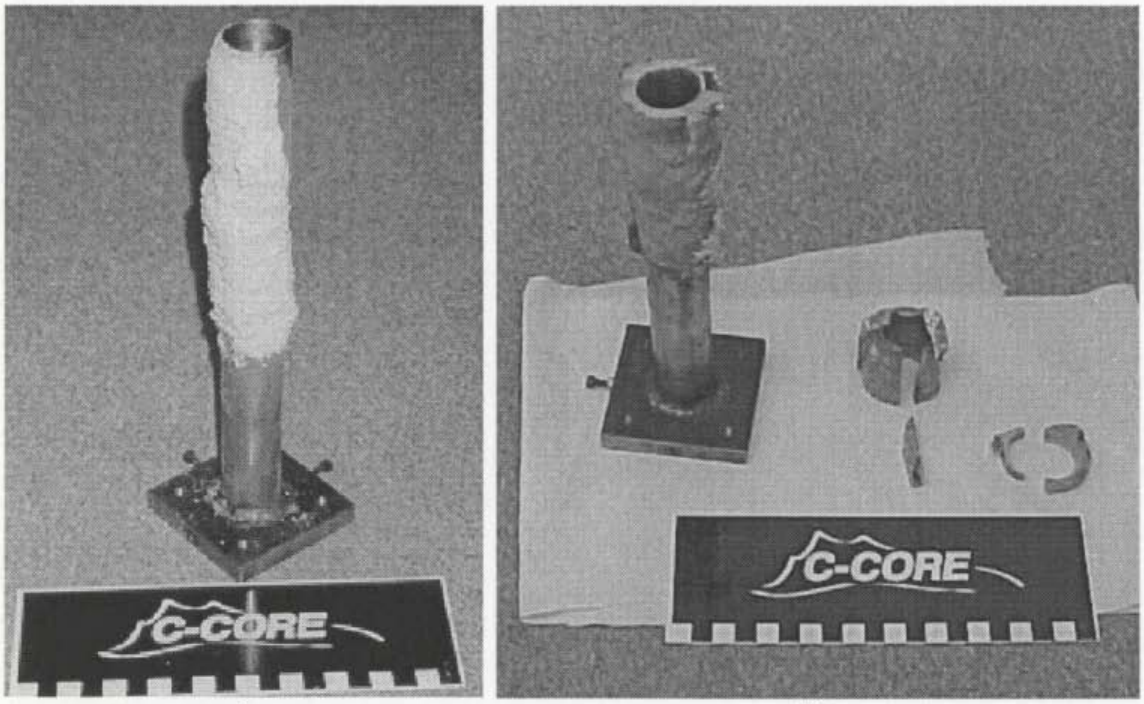

a) b)

Figure 5.5 a) Sand-pile interface sample, test set Pile 1B-3; b) Pile 1 cut and sectioned to obtain both a horizontal and longitudinal sand-pile interface thin section, test set Pile 1B-3.

CHAPTER 6

Experimental Test Results

6.1 Direct Shear Interface Tests

Standard direct shear interface tests gave the peak interface friction angles (δ_{max}) and also provided the residual or constant volume interface friction angles (δ_{cv}) for both the primary and secondary shear directions. Peak shear stresses (τ) observed over the first shear cycle of each test set reveal that the peak interface friction angles ranged between 27.5° and 23.8° depending on the normal stress levels, as shown in Figure 6.1. The peak interface friction angles decrease with stress level, which is in accordance with findings by Zhu (1998) who performed similar tests and observed such behaviour for this material. After the first load reversal, shearing in the secondary direction revealed a reduction in shear stress by up to 20% and a reduction in the interface friction angle of up to 5°.

The cyclic shear tests revealed what was assumed to be δ_{cv} values for both shear directions, both of which decreased with stress level. The constant volume condition was never truly achieved but the volumetric behaviour tended towards a steady state. The average constant volume interface friction angles and the average interface friction angles measured during the initial shear in the primary direction are summarized in Table 6.1.

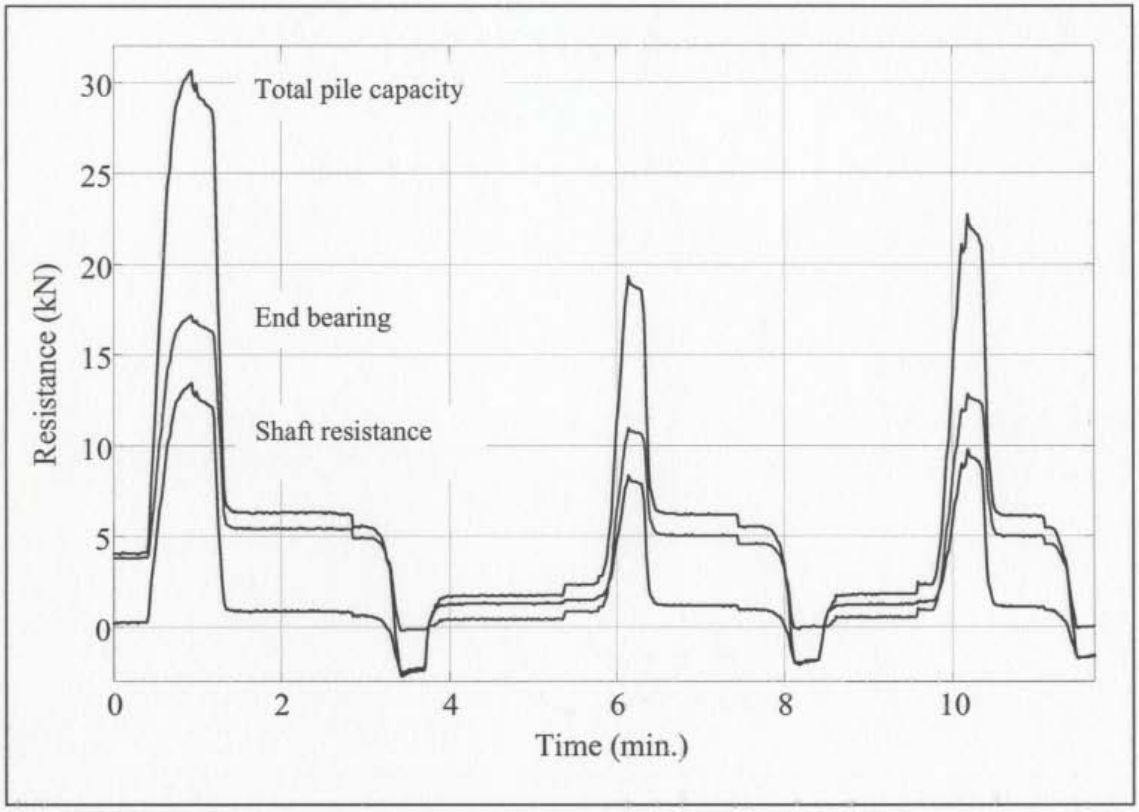

Figure 6.10 Pile loads activated from the first three load cycles (Pile 3A-3).

reduction in shear stress occurred within the first two load reversals and the onset of the critical state was established rather quickly.

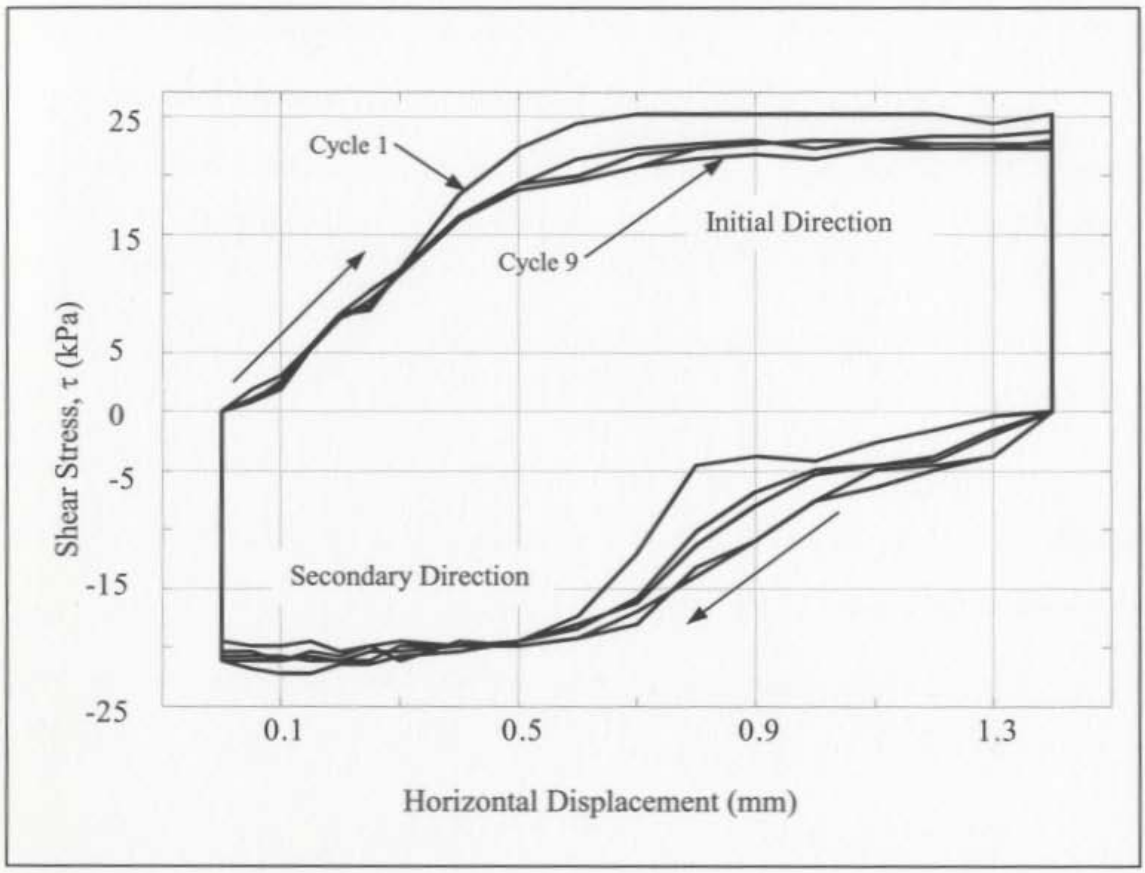

Figure 6.2 Typical cyclic direct shear interface behaviour (σ_n = 60 kPa).

The plastic volumetric strains observed throughout the test series did not reveal a consistent correlation between strain and stress level. Although, the general trend was that dilative volumetric strain in the order of 0.04% during the first load cycle was followed by contractive volumetric strains with continuous load reversals. The maximum contractive volumetric strain was 0.4% after 9 load reversals. The material was assumed

to be near the critical density at the onset of testing. Although a steady state was obtained with respect to shear strength, a constant volume state was never achieved since continuous contractive strains persisted in an erratic manner. It was assumed that a constant volume state was reached and that the small compressive strains observed were due to material losses at the interface gap. Due to dry conditions and the material's workability in this state a small portion of the sand sample was observed to work free of the direct shear box during load reversals. Post-test observations did not reveal the presence of particle crushing at the shear interface.

6.2 Cone Penetrometer Tests

Three cone penetrometer tests were performed in each sand sample, one per pile test. The penetrometer test was executed at the end of each pile test set prior to centrifuge spindown and repositioning of the beam superstructure. Therefore each penetrometer test would be carried out under slightly different conditions. With increasing number of test sets, the soil was subject to additional centrifugal acceleration and deceleration that could cause further compressive/stress cycling of the soil. Furthermore, the amount of sample disturbance from pile and cone tests increases with increasing test sets. The combination of the two factors may explain the observed increase in cone penetrometer tip resistance with increasing test set numbers. Table 6.2 and Figure 6.3 contain the peak cone tip resistances for all three test sets of the five test series, at model depths corresponding to 15 m in the prototype. Maximum and minimum tip resistances are 31 and 19 MPa

respectively, with an average of 25.8 MPa. A typical plot of CPT q_c with model depth is given in Figure 6.4.

Table 6.2 Peak CPT tip resistance at 15 m prototype depth.

Test Series	Test Set	q_c (MPa)
Pile 1A	Cone 1A-1	25
	Cone 1A-2	22
	Cone 1A-3	31
Pile 1B	Cone 1B-1	19
	Cone 1B-2	22.5
	Cone 1B-3	24
Pile 2A	Cone 2A-1	22
	Cone 2A-2	29
	Cone 2A-3	31
Pile 2B	Cone 2B-1	26
	Cone 2B-2	24.5
	Cone 2B-3	26.5
Pile 3A	Cone 3A-1	25
	Cone 3A-2	29
	Cone 3A-3	30

Vertical displacements measured at the model centrepoint reveal that on average 65% of the final surface settlements occur during the centrifuge cycling process prior to executing the first test set and about 25% and 10% subsequent to test sets 2 and 3, respectively. The summation of the total observed settlement, including settlement prior to testing, translates to an average increase in model I_D of about 1.5%, which is not significant enough to explain the increasing trend in CPT q_c values.

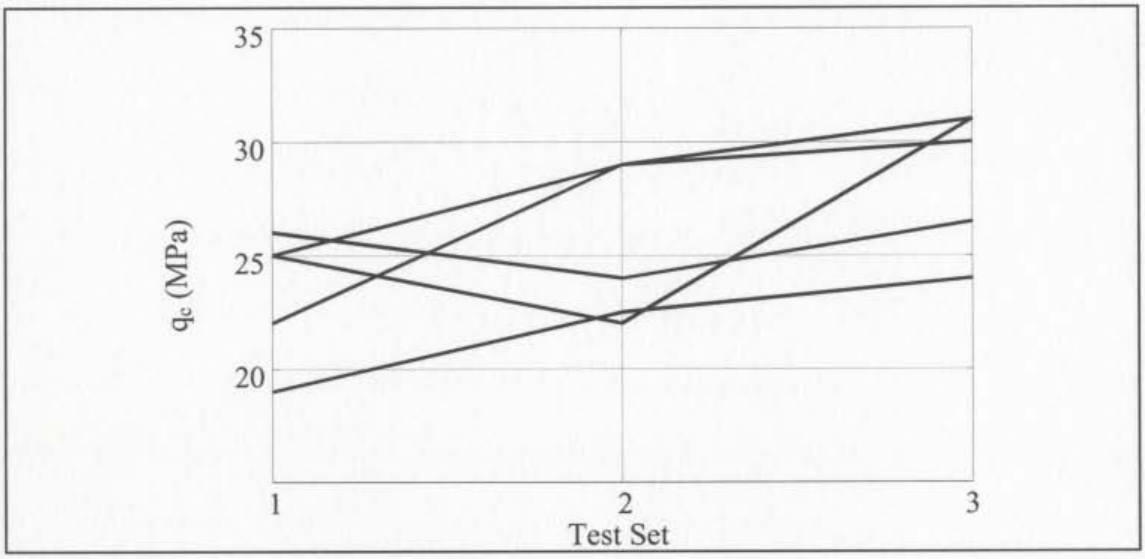

Figure 6.3 CPT q_c trend with increasing test sets at 15 m prototype depth.

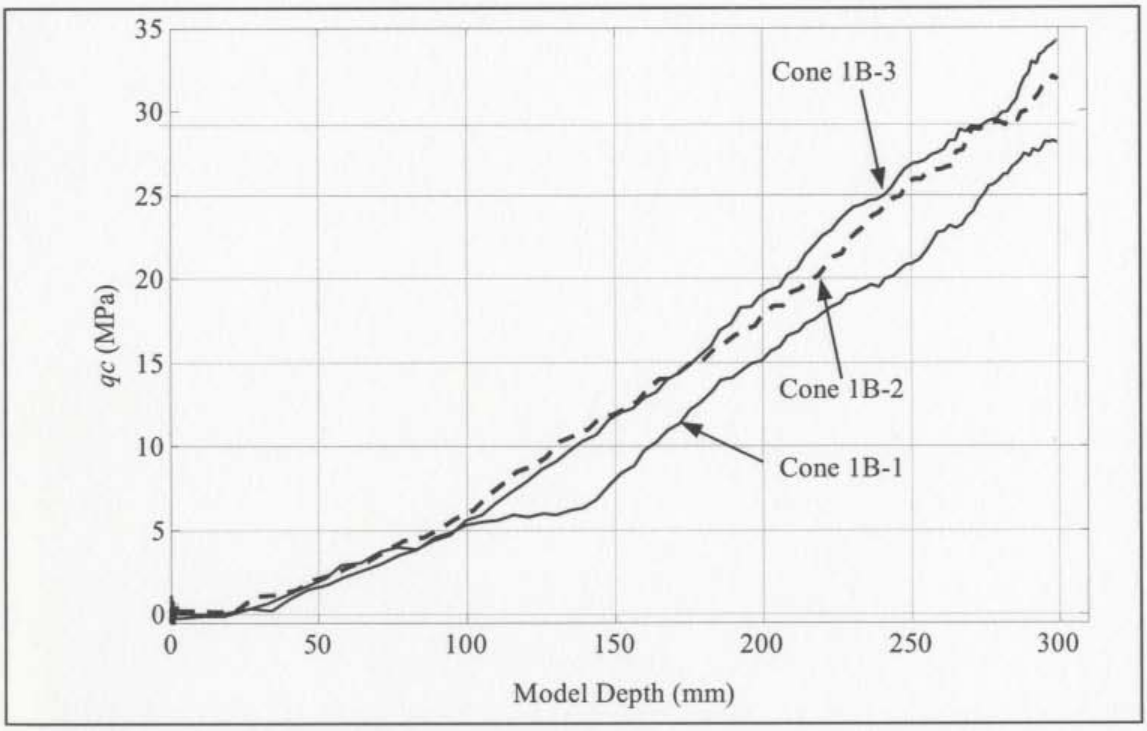

Figure 6.4 CPT q_c soil model profile and increasing strength trend with test sets (Series Pile 1B).

The physical boundary conditions imposed on the cone penetrometer test locations are thought to be the factors influencing the increasing trend of cone tip resistance q_c with increasing test sets. As shown in Figure 5.4, in given test sets a pile test is performed within 180 mm from the CPT location. The pile models are closed end and therefore displace a significant amount of material. Boundary conditions reported in Section 3.3.6 state that a pile model requires a minimum of 7 or 8 pile diameters from a rigid horizontal boundary to avoid boundary influence. Furthermore, the horizontal boundary conditions required for CPTs is recommended as a minimum of 10 cone diameters. The boundary conditions imposed between pile test locations and CPT locations range from 4 to 5.5 pile diameters, therefore the CPT would be expected to be influenced by adjacent pile testing. Kezdi (1964) reported that soil displacements within an area of 3 pile diameters from the pile centreline may be experienced with pile driving or jacking into a medium-dense sand. Accordingly, the soil is densified from pile installation causing an increase in CPT tip resistance. The first cone test of each series is a significant distance from the associated pile test, while the second cone test of the series is performed next to the pile test location of the prior test and finally the third cone test is bound by pile tests on either side and would therefore be expected to yield larger tip resistances than sets 1 and 2.

The pile tests do not have the same imposed boundary conditions as the associated CPT. The first pile test of each test series and the corresponding CPT are both performed in an undisturbed location. The second pile test is performed next to the previous CPT while the second CPT is performed next to the first pile test, which displaces more soil and

imposes a greater influence than a CPT. The third and final pile test is bound by previous CPTs on either side of the test location while the third CPT is bound by a prior pile test on either side. Considering the sequence and timing of each component of a test series, it can be concluded that the cone test gives a good measurement of the model soil strength profile in the first pile test location and gives slightly larger soil strength readings for the second and third pile tests. Therefore estimation of pile capacity with a CPT would yield an increasingly less conservative prediction as the number of test sets increase.

6.3 Pile Model Test Results

Three geometrically similar pile models were tested at different g-levels. A summary of the testing series is given in Table 6.3.

Table 6.3 Summary of pile model test series.

Test Series	Test Sets	Pile length (mm)	Pile diameter (mm)	*g*-level (N)
Pile 1A	Pile 1A-1, 2, 3	225	30	66.7
Pile 1B	Pile 1B-1, 2, 3	225	30	66.7
Pile 2A	Pile 2A-1, 2, 3	263	35	57
Pile 2B	Pile 2B-1, 2, 3	263	35	57
Pile 3A	Pile 3A-1, 2, 3	300	40	50

Both test series Pile 1A and Pile 1B were performed with free rotating pile head fixity. The pile model tested was 30 mm in diameter, 225 mm long and was tested at 66.7*g* to

correspond to the prototype of 2 m in diameter and 15 m in length. Due to the free headed pile head fixity, test sets Pile 1A-1 and Pile 1A-2 resulted in pile inclinations off the vertical by as much as 4°, which resulted in a large portion of the total pile load being carried by the shaft. This situation is undesirable since the same degree of pile inclination is not easily repeatable between test sets and inhibits data comparison and verification of test repeatability. The iterative process of balancing the pile to achieve vertical installation resulted in Pile 1A-3 being installed only about 2.0° off vertical and a near vertical pile installation for test set Pile 1B-1 and perfectly vertical installations for sets Pile 1B-2 and 1B-3. Test set Pile 1B-1 incurred technical difficulties in measuring pile displacements and only remitted partial data. Plots of the pile installation resistances with depth (Figures 6.5a and 6.5b) reveal the effect of pile inclination on shaft resistance. The shaft resistance of an inclined pile model picks up much more quickly with depth than a truly vertical installation that appears to only pick up significant shaft load after about five pile diameters of penetration. It is for this reason that only the vertical installations will be directly compared to one another (Section 6.6). It should be noted that there is some skepticism with respect to the load resistance data for the inclined piles. Due to the introduction of bending moment into the total load cell, the data obtained may be corrupt since the load cell was not designed to carry a moment. The complete set of test data is contained in the supplementary CD-ROM (Hanke, 2001).

Both test series Pile 2A and Pile 2B were performed with rigid pile head fixity. The pile model tested was 35 mm in diameter, 263 mm long and was tested at 57g to correspond

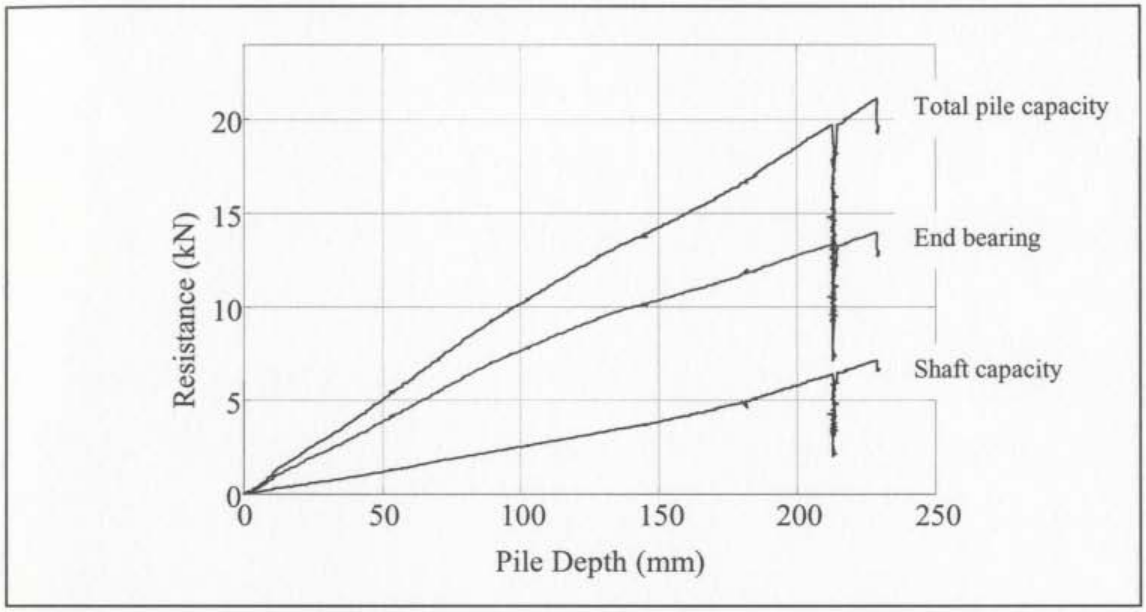

Figure 6.5a Pile installation resistance with 2.5° batter (Pile 1A-3).

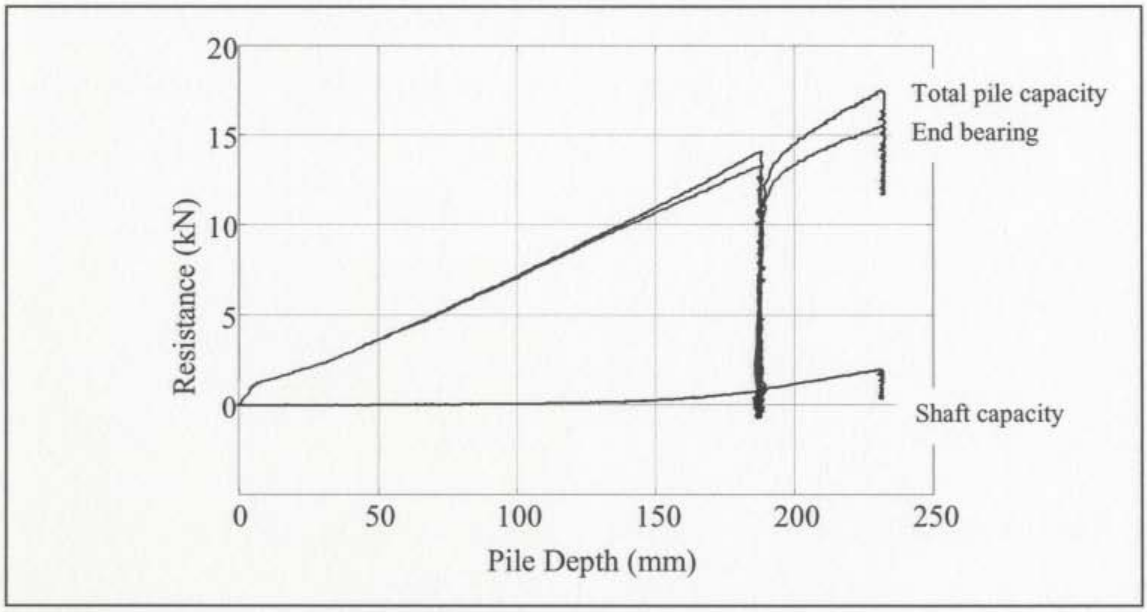

Figure 6.5b Pile installation resistance, vertical installation (Pile 1B-2).

to the prototype of 2 m in diameter and 15 m in length. Due to the rigid pile head fixity, test series Pile 2A and 2B rendered consistent and repeatable test results.

Test series Pile 3A was performed with both rigid pile head fixity and with free rotating ball joint head fixity. The pile model tested was 40 mm in diameter, 300 mm in length and was tested at 50*g* to correspond to the chosen prototype pile. Test sets Pile 3A-1 and Pile 3A-2 were executed with the free rotating ball joint head fixity like both the Pile 1 test series. Like the initial Pile 1 test sets (series Pile 1A) the problem of balancing the pile proved difficult and excessive pile inclination off vertical ensued. The final pile batter for both test sets exceeded 7° and the decision to cease testing prior to completing 40 load reversals was made for set Pile 3A-2, therefore a complete set of data was not obtained. The third test set of the series (Pile 3A-3) was performed with the rigid pile head fixity to avoid the problems encountered within the two prior test sets.

The test results for the piles which were installed vertically are as follows; The loads activated during load testing (total load, end bearing and shaft resistance) are plotted for the first 3 load cycles for Pile 1B-2 on Figure 6.6, for Pile 2B-2 on Figure 6.8 and for Pile 3A-3 on Figure 6.10. End bearing and shaft resistances are plotted versus displacement for the respective piles on Figures 6.7, 6.9 and 6.11. Each pile is displaced 3 mm above and 3 mm below the original drive depth, which constitutes the reference datum. The maximum tensile shaft capacity is reached very quickly and is maintained for the total cyclic tensile displacement of 6 mm. Conversely, the start of a given compressive cycle

sees the pile being displaced downward from a point 3 mm above the reference datum where the compressive shaft resistance is virtually equal to the tensile shaft resistance. After about 3 mm of compressive displacement, or 10% of the pile diameter, the pile is considered to have reached full failure (Toolan *et al.* 1990; Terzaghi *et al.* 1996). Although, at the point where the pile tip reaches the reference datum and the pile is thought to have reached full failure, the compressive shaft resistance starts to increase significantly reaching a maximum after 3 mm of further compressive displacement. Total pile resistance, end bearing and shaft resistance, inclination off vertical and post-cyclic resistances are summarized in Table 6.4 for test series Pile 1A and Pile 1B, in Table 6.5 for piles 2A and 2B and in Table 6.6 for Pile 3A.

Pile 3A-3 had a clearance problem at the pile tip. The space between the end bearing cap and the pile shaft was not sufficient to keep the two load transferring mechanisms separate. It was observed that during compressive loading a portion of the end bearing load was transferred to the pile shaft and interpreted through DAS as shaft resistance. Conversely, tensile loading was not affected and remitted the expected tensile load behaviour. Post-test examination of the pile assembly revealed minimal clearance between the end cap and pile shaft. Calibration of the pile assembly in this state, to delineate the magnitude of load transfer, proved difficult and was not completed to satisfaction. The total load recorded is correct but the portion of the end bearing is under represented whereas the shaft resistance in compression is too high. The tensile shaft resistance was not affected and therefore permits a basis for estimating the true

compressive shaft and end bearing resistance based on the shaft to end bearing ratios of Pile 1 and Pile 2. The estimates of compressive shaft resistances and end bearing for Pile 3A-3 are given in Table 6.6 along with the actual measured data.

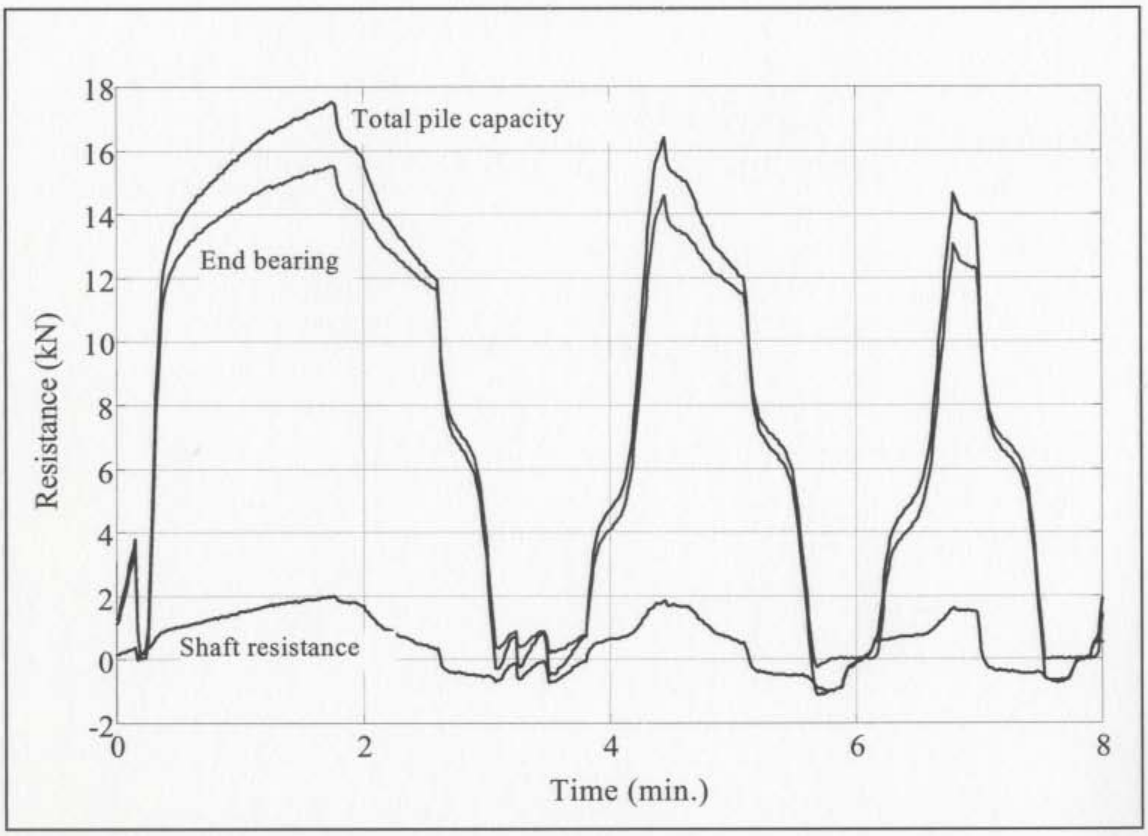

Figure 6.6 Pile loads activated from the first three load cycles (Pile 1B-2).

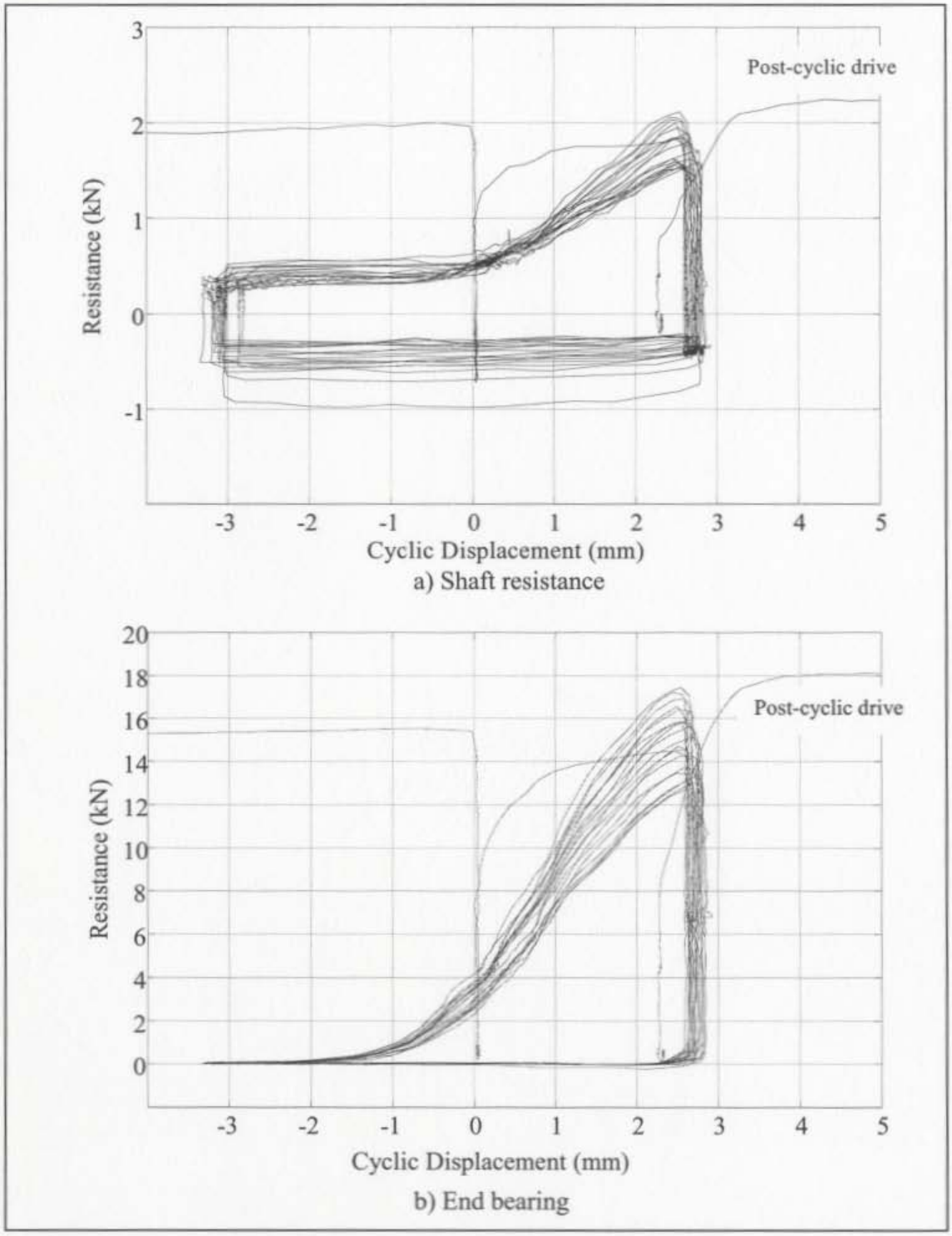

Figure 6.7 End bearing and shaft capacity response to cyclic loading (Pile 1B-2).

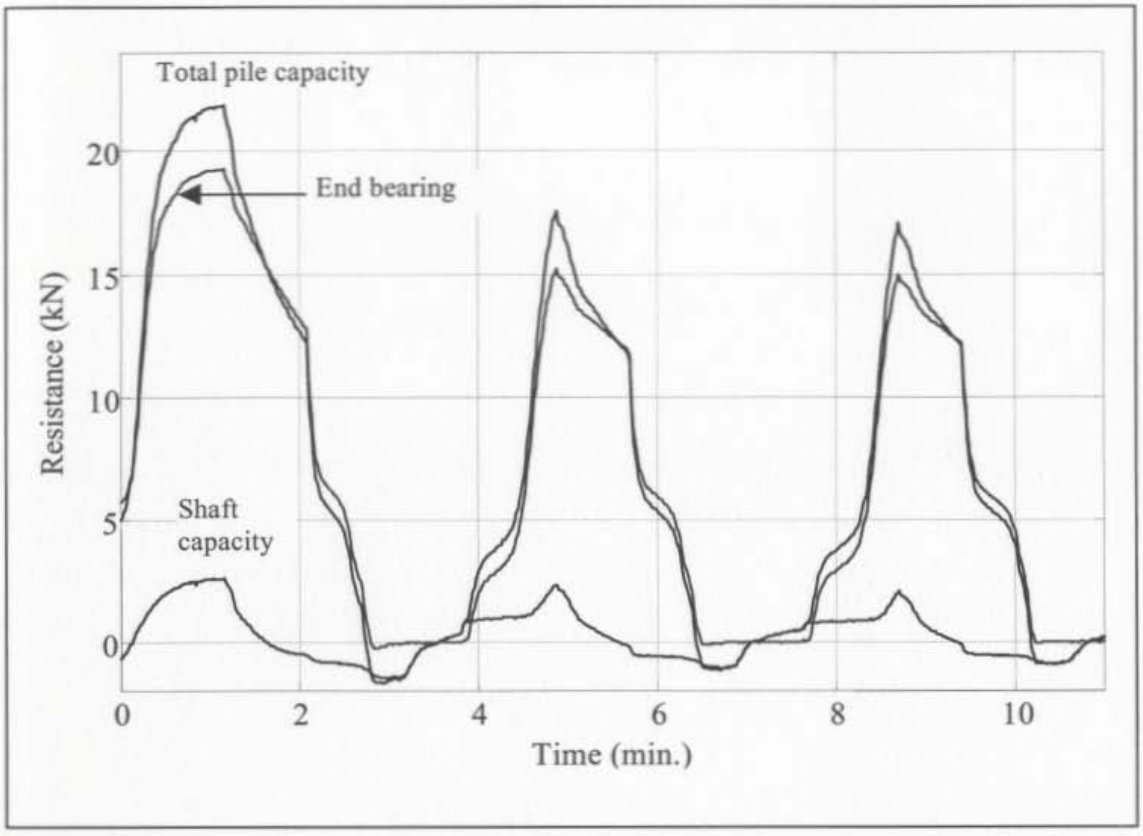

Figure 6.8 Pile loads activated from the first three load cycles (Pile 2A-2).

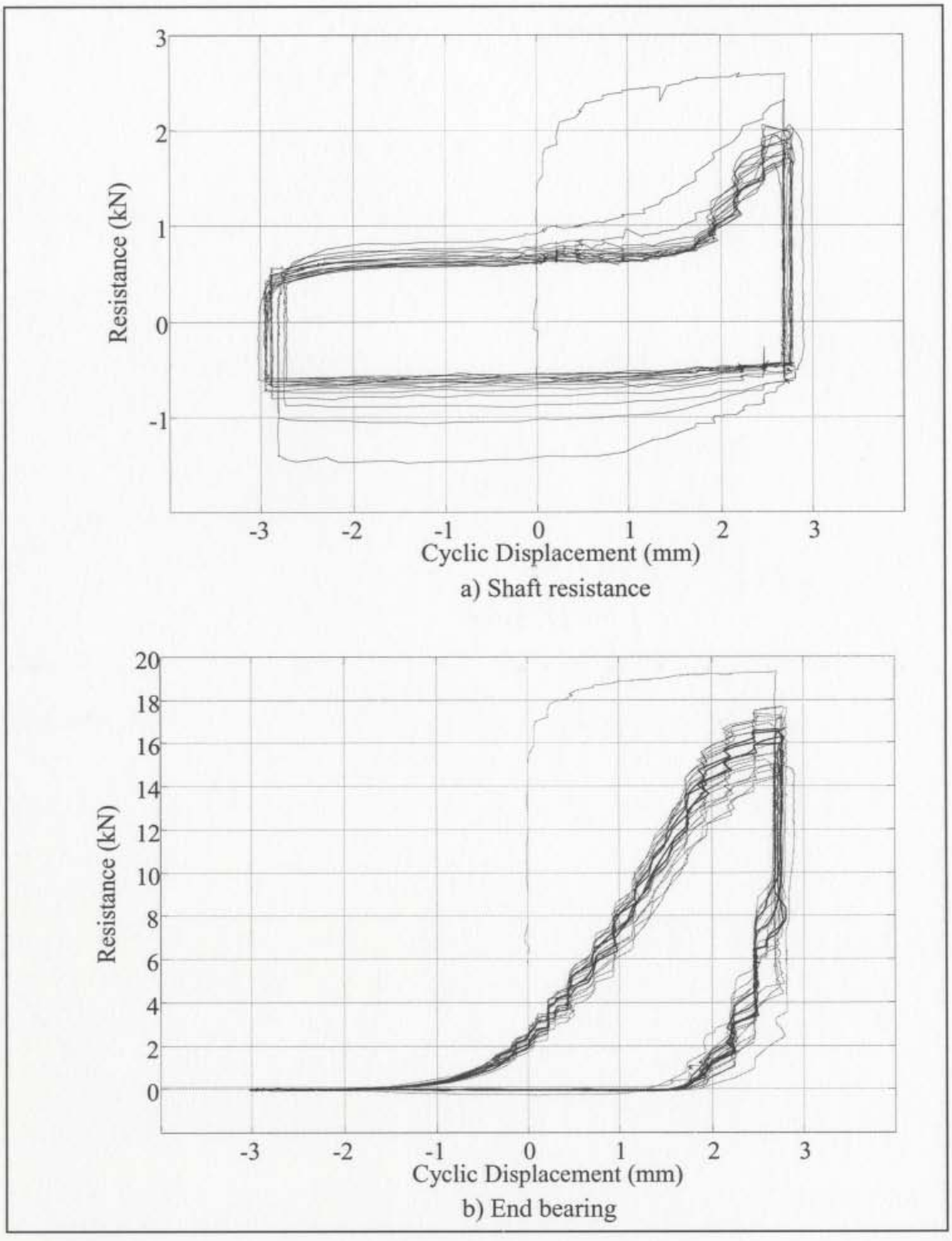

Figure 6.9 End bearing and shaft capacity response to cyclic loading (Pile 2A-2).

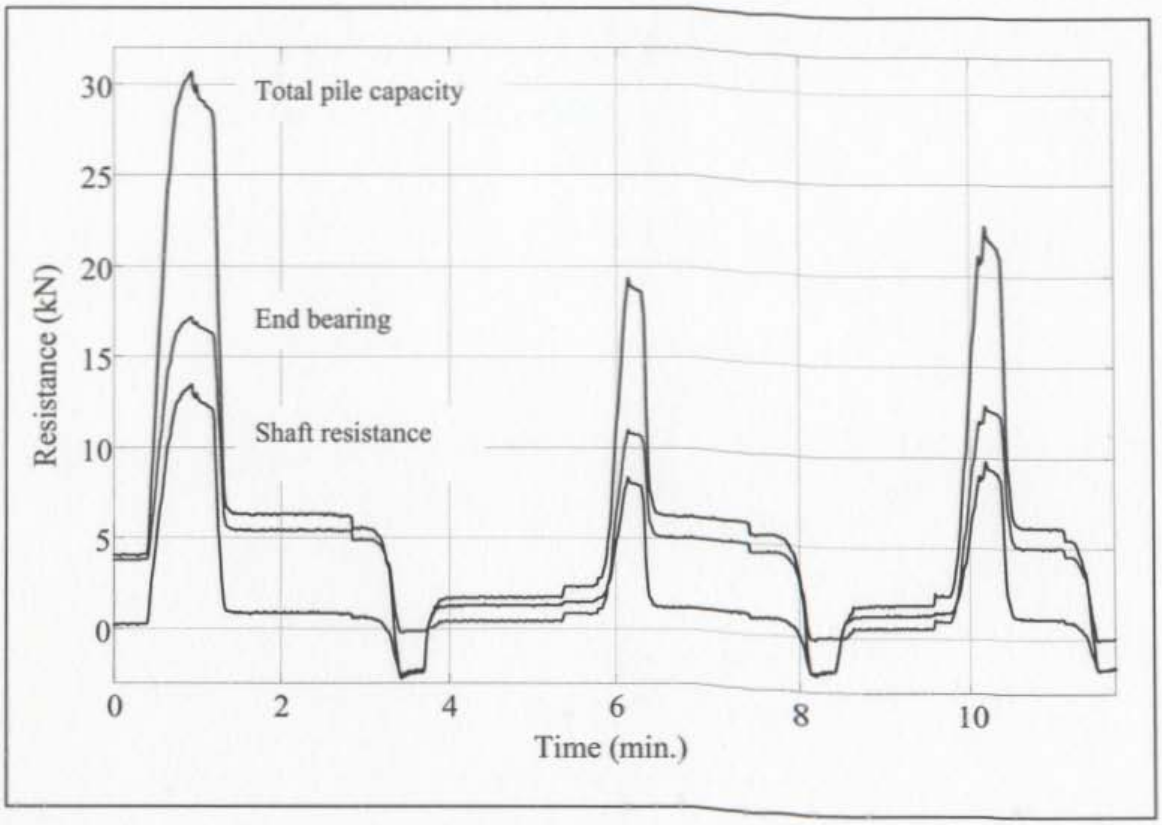

Figure 6.10 Pile loads activated from the first three load cycles (Pile 3A-3).

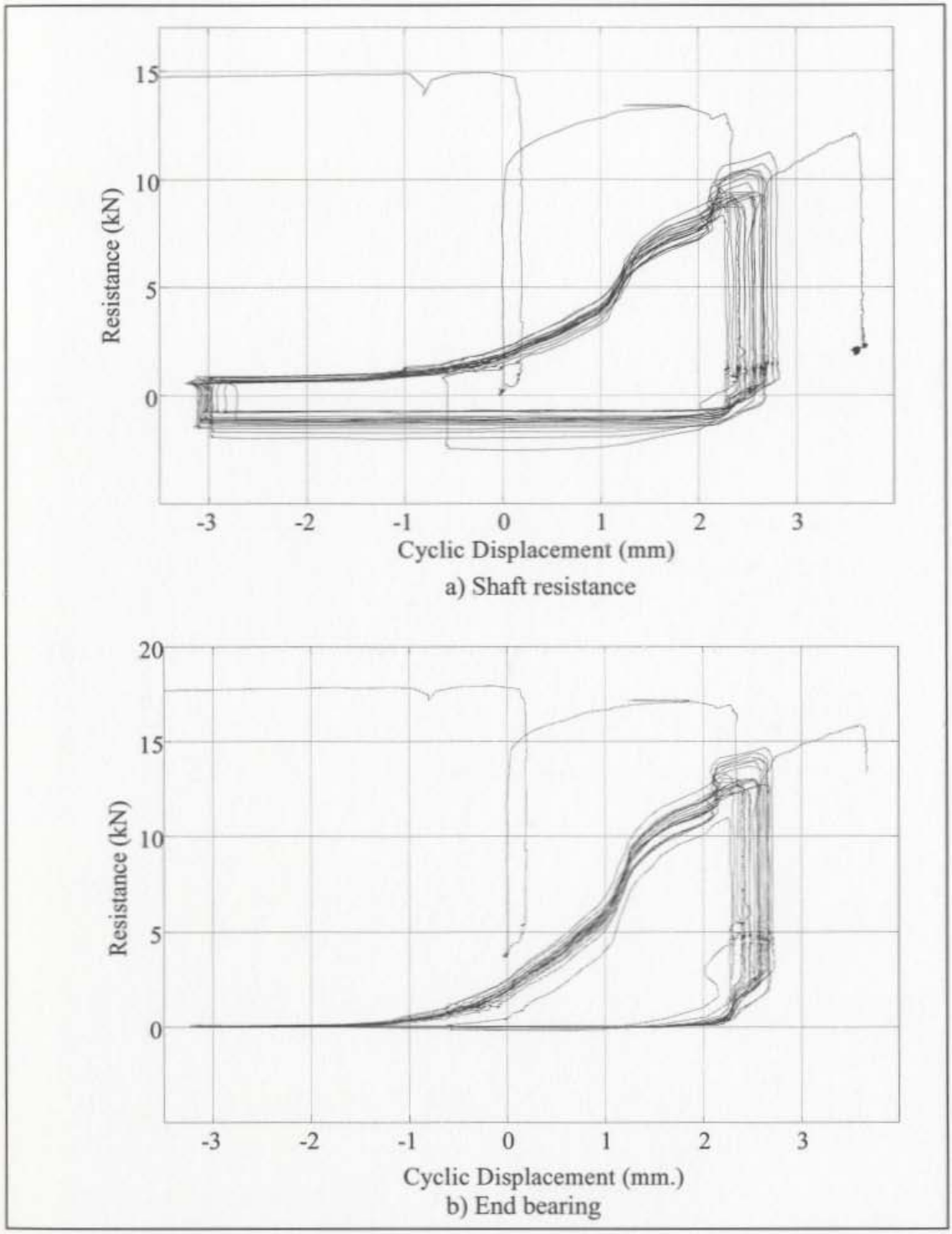

Figure 6.11 End bearing and shaft capacity response to cyclic loading (Pile 3A-3).

Table 6.4 Pile load data, test series Pile 1A and Pile 1B.

Series	Set	Test Cycle No. 1 Resistance (kN)			Post-Cyclic Resistance (kN)			No. cycles *N*	Batter (deg.)	Head Fixity
		Shaft Comp.	Shaft Tension	End Bearing	Shaft Comp. *(Comp)	Shaft Tension	End Bearing			
Pile 1A	Pile 1A-1	10.9	2	17.8	8.5 *(2.4)	1.1	14	13	4	Free
	Pile 1A-2	11.1	2	17.8	7.0 *(2.3)	1.1	12.1	14	3.6	Free
	Pile 1A-3	7.1	1.3	13.9	5.8 *(2.2)	0.8	12.3	20	2.5	Free
Pile 1B	Pile 1B-1	3.1	1.1	17.9	-- *(--)	--	--	7	1	Free
	Pile 1B-2	1.8	1	15.2	2.2 *(0.5)	0.4	17.9	20	0	Free
	Pile 1B-3	1.5	1.2	17.4	0.9 *(0.3)	0.5	17.9	20	0	Free

* Compressive shaft resistance, disp. < 10% pile dia.

Table 6.5 Pile load data, test series Pile 2A and Pile 2B.

Series	Set	Test Cycle No. 1 Resistance (kN)			Post-Cyclic Resistance (kN)			No. cycles *N*	Batter (deg.)	Head Fixity
		Shaft Comp.	Shaft Tension	End Bearing	Shaft Comp. *(Comp)	Shaft Tension	End Bearing			
Pile 2A	Pile 2A-1	2.8	1.5	20.1	2.2 *(0.5)	0.5	19	20	0	Fixed
	Pile 2A-2	2.4	1.5	19.2	2.1 *(0.6)	0.6	17.5	20	0	Fixed
	Pile 2A-3	3.3	1.8	20.8	2.8 *(0.8)	0.7	19.3	20	0	Fixed
Pile 2B	Pile 2B-1	2.7	1.4	19.3	2.3 *(0.5)	0.5	18.6	20	0	Fixed
	Pile 2B-2	2.6	1.6	19.5	2.4 *(0.6)	0.5	18.6	20	0	Fixed
	Pile 2B-3	3.2	1.8	20.1	2.8 *(0.7)	0.7	19.5	20	0	Fixed

* Compressive shaft resistance, disp. < 10% pile dia.

Table 6.6 Pile load data, test series Pile 3A

Series	Set	Test Cycle No. 1 Resistance (kN)			Post-Cyclic Resistance (kN)			No. cycles *N*	Batter (deg.)	Head Fixity
		Shaft Comp.	Shaft Tension	End Bearing	Shaft Comp. *(Comp)	Shaft Tension	End Bearing			
Pile 3A	Pile 3A-1	13.1	2	12.5	14 *(2)	0.8	14.1	20	7.2	Free
	Pile 3A-2	12.4	2.1	17.2	11.1 *(--)	2	14.6	4	7.5	Free
	Pile 3A-3	13.4 *[3.7]*	2.5	17.1 *[26.8]*	10.1 *[2.5]* *(2)	1	14.2 *[21.8]*	20	0	Fixed

* Compressive shaft resistance, disp. < 10% pile dia.

[ ] Estimated maximum compressive resistances (Pile 3A-3).

6.4 Modelling of Models

The modelling of models procedure described in Section 3.3.4 provides a check for the modelling procedure. Since the acceleration level and the size of the model are directly related, direct similarity between the modelling of models is expected if significant error is not encountered. To follow the method of modelling of models, the stress levels at homologous points between models of different geometric scale should be equal since stress scales at *1:1* between like models and the corresponding prototype. This comparison may not only be applied towards the pile model tests but may also be applied to the soil model strength profile determined with the CPT.

The CPT results given in Section 6.2 include q_c values from 15 tests and 3 different g-levels at the representative prototype design depth all within $\pm 10\%$ of the average despite the influence of varying degrees of soil disturbance from adjacent piles of different diameters (Figure 6.3). This initially suggests the verification of the centrifuge modelling procedure to produce consistent sand models at varying g-levels.

Comparison of average pile shaft stresses (f_s) and end bearing stresses (q_b) for similar test sets of the three pile models has been done in an attempt to substantiate the test data and confirm the modelling of models principle. For comparative purposes, only test sets of piles with no measurable inclination for free headed fixity or piles with a fixed headed fixity are directly compared. Furthermore, due to the observed soil model densification with increasing test sets, the test sets chosen for modelling of models comparison are all

of the same set magnitude and are therefore assumed to have the same relative density. The test sets chosen are Pile 1B-3, Pile 2A-3, Pile 2B-3 and Pile 3A-3. The 4 test sets mentioned are all of set number 3 and all were of a fixed pile head fixity except for Pile 1B-3 which was of a free rotating head fixity but was performed with no measurable inclination and therefore may be directly compared to piles with rigid pile head fixity. Table 6.7 compares the pile shaft and end bearing stress levels of the 4 test sets mentioned above. As described in Section 6.5, Pile 3A-3 had a structural deficiency that transferred end bearing load to the pile shaft. By using the shaft to end bearing resistance ratios from Piles 1 and 2, the true compressive shaft resistance and end bearing was estimated. Both the measured values and the estimated values are given in Table 6.7.

Table 6.7 Model stress level comparison.

Set	Test Cycle No. 1 Stresses			Post-cyclic Stresses			Δf_s (C) %	Δf_s (T) %
	f_s (C) (kPa)	f_s (T) (kPa)	q_b (MPa)	f_s (C) (kPa)	f_s (T) (kPa)	q_b (MPa)		
Pile 1B-3	70.8	61.3	24.6	42.5 *14.2	23.6	25.3	-40 *-80	-61.5
Pile 2A-3	114.1	62.2	21.6	96.8 *27.7	24.2	20.1	-15.2 *-75.7	-61.1
Pile 2B-3	110.7	62.2	20.9	96.8 *24.2	24.2	22.9	-12.6 -78.1	-61.1
Pile 3A-3	355.4 *[98.1]*	66.3	13.6 *[21.3]*	267.9 *[66.3]* *53.1	26.5	11.3 *[17.4]*	-24.6 *[-32.4]* *-45.9	-60
C = compression T = tension						**Average**	**-23.1%**	**-60.9%**
* Compressive shaft stress, disp. < 10% pile dia.							***-69.9%**	
[ ] Estimated maximum compressive values (Pile 3A-3).								

The tensile shaft stress levels over the first load cycle are very uniform between the three pile models for the test sets compared in Table 6.7. The compressive shaft resistances over the same test period are not as close and do not plot as linear as the tensile resistances, shown in Figure 6.12a. Conversely, the end bearing stresses over the first load cycle are fairly uniform much like the tensile shaft resistance. It should be noted that the compressive resistances plotted for the Pile 3A-3 test set are the estimated values. This manipulation of data is supported by the fact that the tensile resistance for this set plotted linearly with the other associated tests and was not manipulated in any way. Both the tensile shaft stress and end bearing stresses give uniform values and would therefore support the conception that the centrifuge modelling procedures employed throughout the test series yield data that appears to be able to be extrapolated to the full-scale prototype.

Observing the post-cyclic stress levels reported in Table 6.7 reveals a similar stress level trend as seen during the first load cycle. As shown in Figure 6.12b, the tensile shaft stresses are quite uniform between the 4 test sets, as is the post-cyclic pile end bearing stress levels. As shown in Figures 6.7, 6.9 and 6.11 there are two distinct levels or stages of post-cyclic compressive shaft resistance throughout the compressive load cycle. Two states of compressive shaft resistance were plotted; the shaft stress observed after a small displacement (<10% pile dia.) and the maximum shaft stress achieved at the completion of the compressive load cycle (disp. > 10% pile dia.). Like the pre-cyclic condition, the maximum compressive shaft stress levels exhibit a slightly more erratic response, while the small displacement shaft stress appeared to increase linearly with pile diameter.

Conversely, the relative magnitude of average tensile shaft stress degradation with cyclic loading was observed to be extremely uniform, all sets within $\pm 0.75\%$, while the compressive shaft stresses display a variance greater than 20%. .

Both the tensile shaft stresses and end bearing stresses give uniform values and would therefore validate the model data and increase the credibility of the centrifuge modelling procedures employed. The erratic values of the compressive shaft stress levels can not be entirely accounted for. A possible source of error could be from a lateral loading force present for test locations off the centreline of centrifuge travel. Therefore a small moment is created and transferred to the primary load cell located at the pile head. Further difference may be accounted for from the different pile head fixities and from other small improvements to the testing procedure that were implemented as the testing program developed.

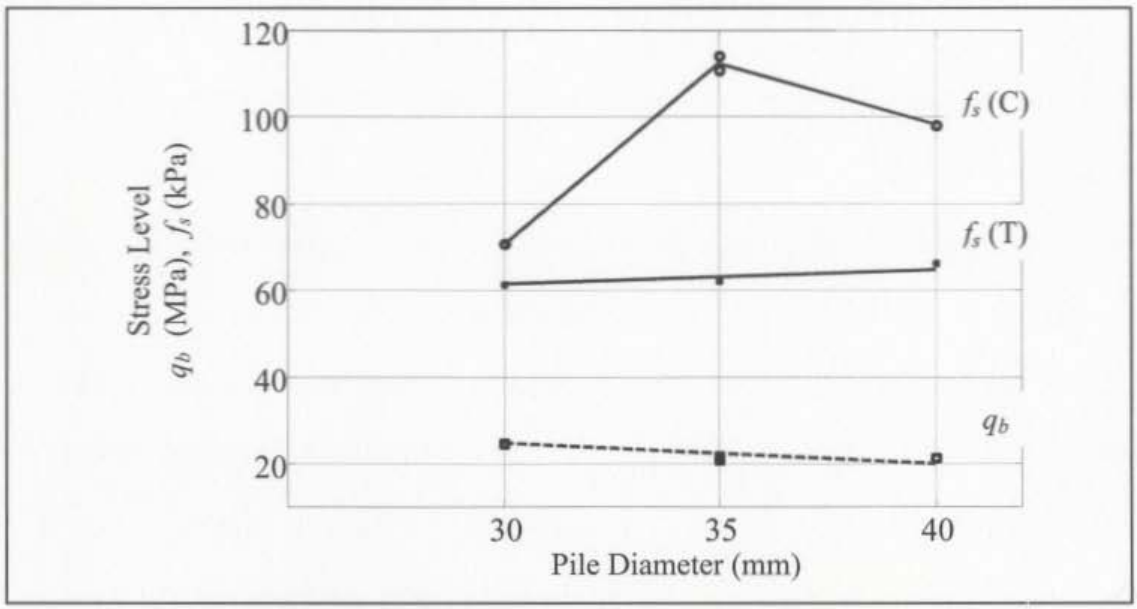

Figure 6.12a End bearing and shaft stress levels over load cycle No. 1.

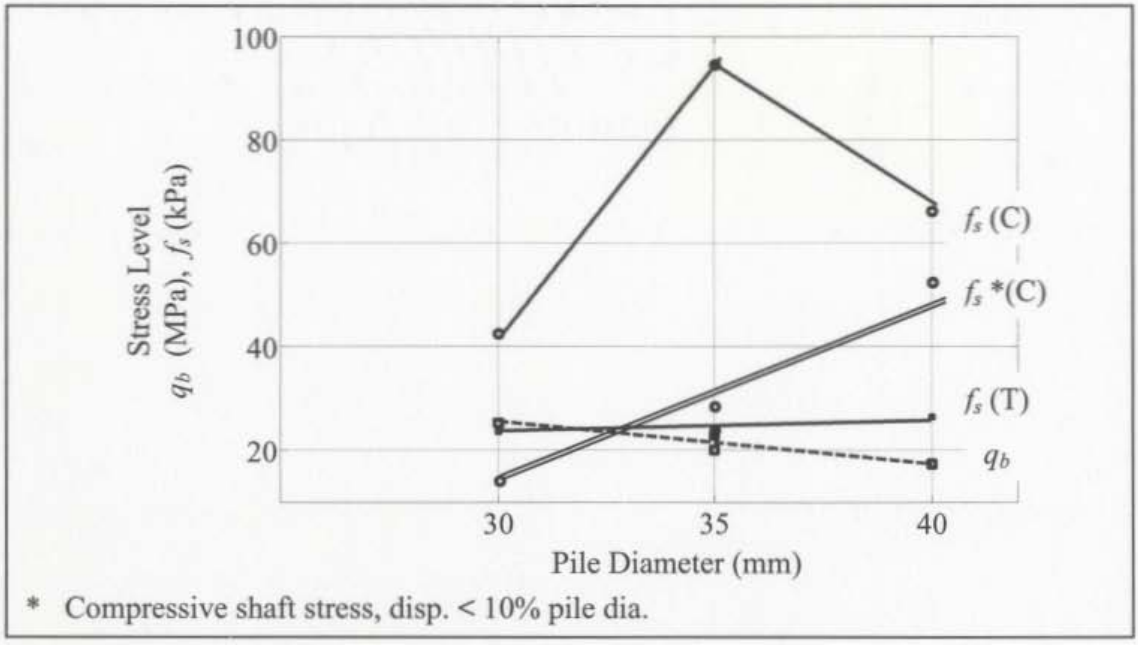

Figure 6.12b Post-cyclic end bearing and shaft stress levels after 40 load reversals.

6.5 Post-Test Findings

Post-test excavation revealed a significant amount of sand particle crushing at the test locations of piles and cone penetrometers. During excavation of the sand material an attempt was made to retrieve some of the crushed particles from the test locations. Due to dry conditions and the material's workability in this state a significant portion of the retrieved sand was contaminated with virgin material, i.e. sand grains that were not at the shear interface and therefore were not subject to crushing. Thus, the sand sample collected provided a very conservative measure of the extent of particle crushing along the sand-pile interface. In Figure 6.13 the gradations of the virgin material and the crushed post-test sample are compared to reveal a definite increase in the percentage of fines, from less than 1% to 12%. As reported by Lehane and Jardine (1994), the constant volume interface friction angle (δ_{cv}) is influenced by the active mean particle size at the sand-pile interface. As the mean particle size decreases, the constant volume interface friction angle increases. Therefore, the interface friction angles determined with the modified direct shear interface apparatus would underestimate the friction angles within the pile model tests since the direct shear tests did not show any evidence of particle crushing.

A sample of the sand-steel interface was obtained for test set Pile 1B-3. Horizontal and longitudinal thin-sections were prepared and analyzed under a microscope in an attempt to delineate the extent of fine sand particle accumulation at the sand-steel interface. The thin-sections were cut from Pile 1 at a distance of about 40 mm above the pile toe.

Figures 6.14a and 6.14b show the magnified sand-steel interfaces of the longitudinal and horizontal sections respectively. At a magnification of 170 times, the slides indicate an accumulation of fine material at the steel interface. The magnitude or band thickness of the crushed material is difficult to determine due to the poor clarity of the thin-sections. Due to the spherical nature of the modelling sand and the absence of elongated or platy grain shapes, particle orientation was not observed.

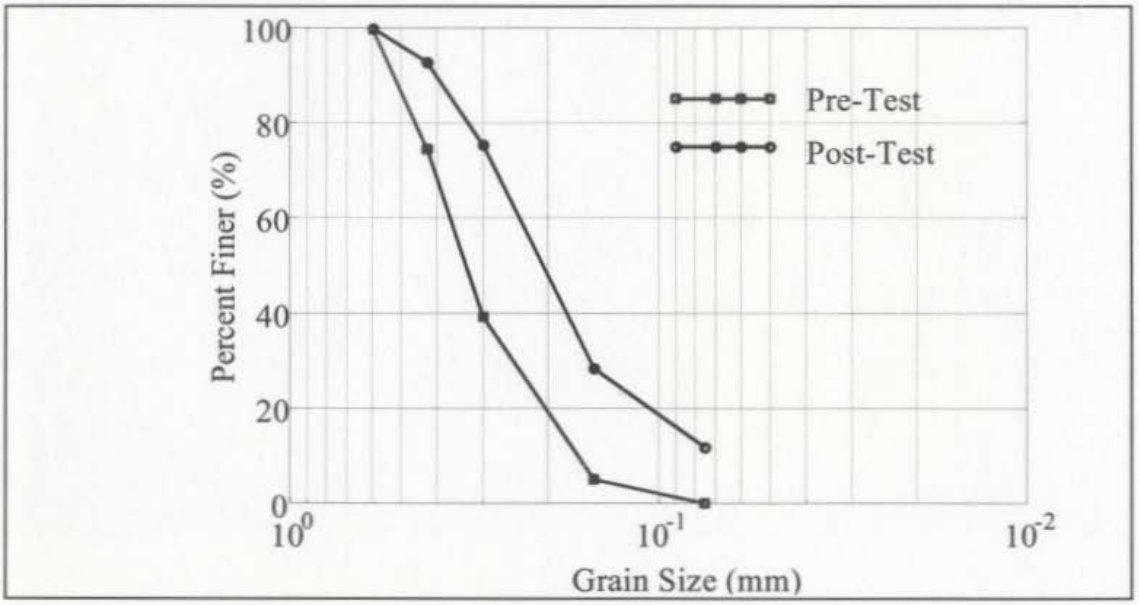

Figure 6.13 Comparison of gradation between virgin sand and a sample taken from the pile test locations containing crushed particles.

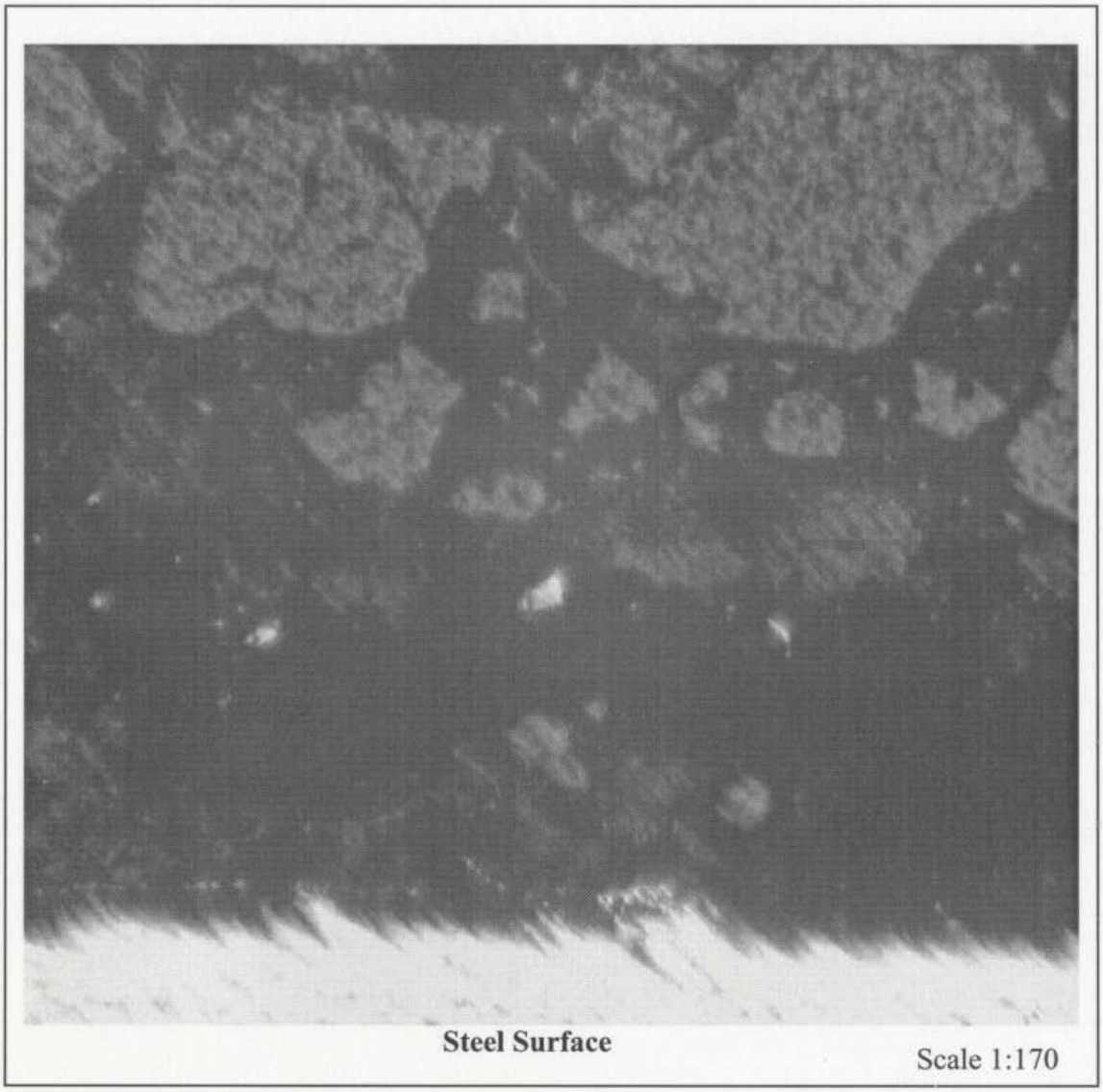

Figure 6.14a Longitudinal thin-section of Pile 1B-3 showing the post-cyclic sand-steel interface.

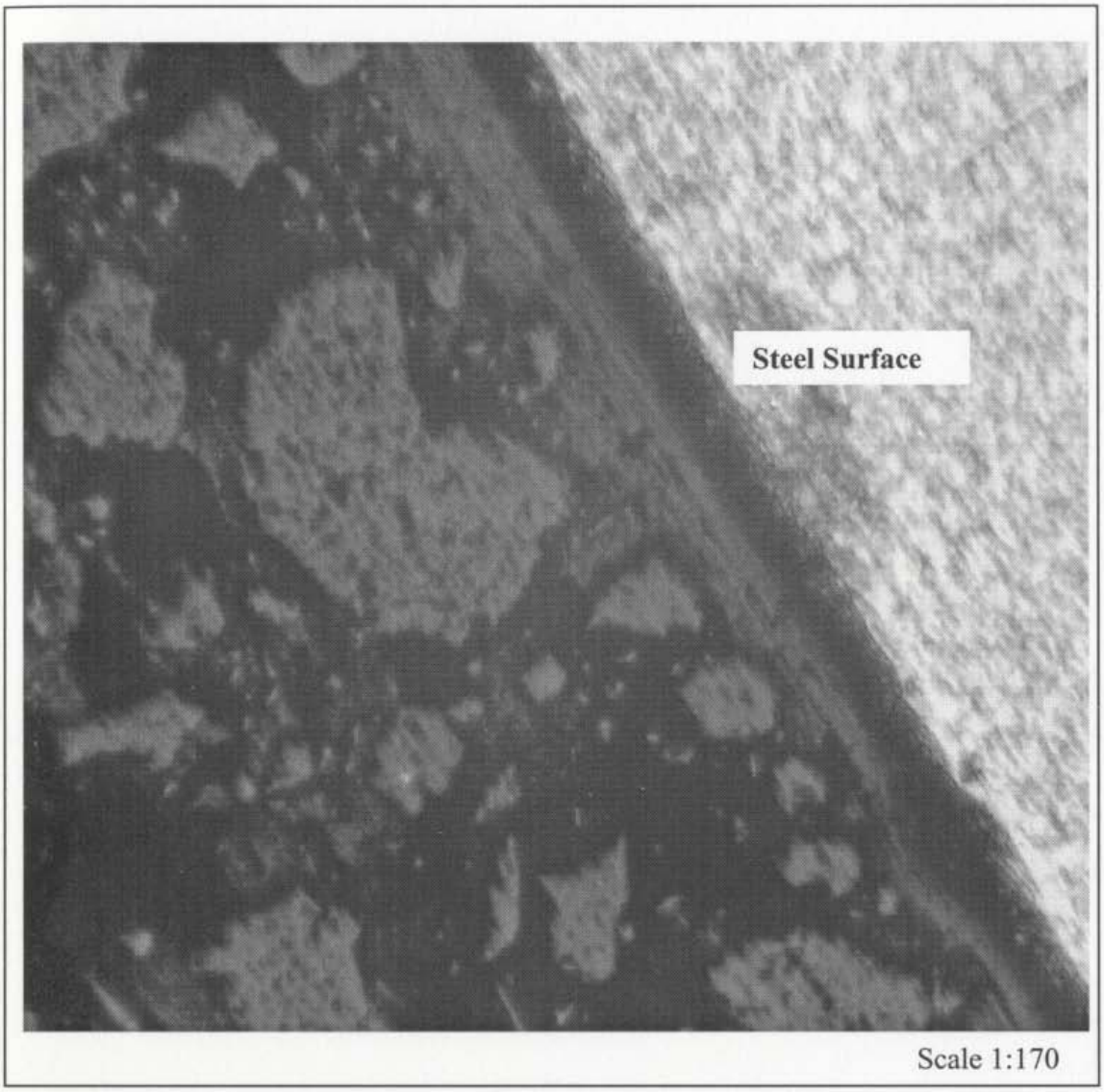

Figure 6.14b Horizontal thin-section of Pile 1B-3 showing the post-cyclic sand-steel interface.

CHAPTER 7

Data Analysis

7.1 Comparison of Analytical Predictions to Measured Data

The physical modelling data presented in Table 6.7 reveals reasonable similarity between stress levels and degradation rates with cyclic loading for the three pile models tested. For this reason, the pile shaft stress levels given in Table 6.7 were averaged and converted to a resistance at prototype scale, as shown in Table 7.1. The measured pre-cyclic and post-cyclic shaft loads will be compared to different forms of analytical prediction. Large discrepancies between the various procedures are apparent. Discrepancies occur with respect to the interface friction angle (δ), magnitude and method of determination, but more so with respect to the earth pressure coefficient (K). The tensile and compressive shaft resistances for measured ϕ, δ and varying K values have been computed and presented in Table 7.2 at prototype scale.

Table 7.1 Pile model shaft capacities presented at prototype scale.

Loading Direction	Cycle 1 Q_s (kN)	Cycle 20 Q_s (kN)
Tension	5900	2300
Compression	9300	6200
* Compression	N/A	2800

* Post-cyclic compressive shaft resistance, disp. < 10% pile dia.

Table 7.2 Computed pile shaft resistance at prototype scale with measured ϕ and δ values and various recommended earth pressure coefficients K.

ϕ	δ	Earth Pressure Coefficient K		f_s (kPa)	Q_s (kN)
ϕ_{max} 43.8°	δ_{max} 22°	K_a	0.18	8.1	760
		K_o	0.31	13.9	1300
		K_p	5.50	246.5	23000
		*CFEM	0.62	27.8	2600
		API RP2A, 14th ed.	0.70	31.4	3000
		API RP2A, 15th ed.	0.80	35.9	3400
		Craig (1997)	**1.5	67.2	6300
			2.00	89.6	8400
ϕ_{cs} 37.4°	δ_{cv} 21° (comp.)	K_a	0.24	10.2	960
		K_o	0.39	16.6	1600
		K_p	4.1	174.6	16500
		*CFEM	0.78	33.2	3100
		API RP2A, 14th ed.	0.7	29.8	2800
		API RP2A, 15th ed.	0.8	34.1	3200
		Craig (1997)	**1.5	63.9	6000
			2	85.2	8000
ϕ_{cs} 37.4°	δ_{cv} 19° (tension)	K_a	0.24	9.2	860
		K_o	0.39	14.9	1400
		K_p	4.1	156.6	14800
		*CFEM	0.78	29.8	2800
		API RP2A, 14th ed.	0.5	19.1	1800
		API RP2A, 15th ed.	0.8	30.6	2880
		Craig (1997)	**1.5	57.3	5400
			2	76.4	7200

* Canadian Foundation Engineering Manual, 3rd Edition (1992).

** Estimated reduction of Craig's coefficient to accommodate for medium-dense sand.

The average tensile and compressive shaft stresses were computed with Equation (2.2) using measured values of ϕ (Zhu, 1998) and δ (direct shear interface test) and earth pressure coefficients K recommended by various foundation design sources as outlined in Table 7.2. Both the maximum and critical state internal friction angles were used within the computations as was the maximum and constant volume interface friction angles to represent the pre and post-cyclic states, respectively. The analytical design procedures followed did not specify a preferred method for determination of ϕ values. Following Zhu (1998), ϕ values were calculated from triaxial tests at effective vertical stress levels found at one third of the pile depth.

The active, passive and at rest earth pressure states were included in the computations to provide the full spectrum of possible shaft resistances. The active, passive and at rest earth pressure coefficients were theoretically determined using the corresponding ϕ value taken at one-third of the model depth to minimize the stress field scaling error, as described in Section 3.3.2. The earth pressure coefficients recommended by API RP2A are for low displacement piles but in some cases were greater than the earth pressure coefficients recommended by the Canadian Foundation Engineering Manual (CFEM, 1992) for displacement-type piles, demonstrating the wide discrepancies that exist between various design procedures. Craig (1997) recommended a K value of 2 for displacement-type piles in dense sands. The average relative density of the modelling sand along the embedment length is about 73%, therefore a reduced K value of 1.5 was

estimated to accommodate for the medium-dense state of the sand model. Likewise, Ireland (1957) also recommended an earth pressure coefficient value of 1.5.

The maximum ϕ and δ values would be most representative of pile shaft resistances during the first load cycle given that the pile is short. Conversely, the critical state and constant volume friction angles are included to represent the post-cyclic state. Separate constant volume interface friction angles are included in the computations for the compressive and tensile loading conditions. Craig (1997) recommends an interface friction angle of 20°, which is the average of the measured compressive and tensile δ_{cv} values (21° and 19°). Alawneh (1999) recommends $\delta = \phi_{cv}$ - 4° for steel piles and Kraft (1990; 1991) recommends a δ/ϕ_{cv} of about 0.7 for siliceous soils.

Using the maximum friction angles, the computed shaft resistances with recommended K values ranged from 2600 kN to 8400 kN. By using K equal to $2K_o$, as recommended by the Canadian Foundation Engineering Manual, a very conservative shaft resistance is computed for either the tensile of compressive loading direction. Conversely, Craig gave a very close prediction of the compressive shaft resistance but overestimated the tensile resistance. Viewing the experimental data reveals that any design formulation that does not distinguish between tensile and compressive shaft resistances for displacement-type piles will encounter significant error. The 15th edition of API RP2A does exactly this and yields a safe measure of the tensile resistance but underestimates the measured compressive shaft resistance by a significant margin. Alawneh defines the earth pressure

coefficient K as a function of both pile diameter and relative density but the values presented were for low displacement piles. Kraft also defines K as a function of relative density and recommends an earth pressure coefficient of 0.9 for steel displacement-type piles within sand of equal relative density to the soil model. The δ values suggested by Alawneh and Kraft are greater than the measured values determined with the direct shear interface tests. Recalling that the standard direct shear interface tests did not generate stresses great enough to produce grain crushing, as was the case during the pile installation process, therefore the measured values may be conservative since the interface friction angle is known to increase with decreasing mean particle size.

Use of the critical state and constant volume friction angles to represent the post-cyclic test condition reveals a much different range of prediction accuracy. The use of constant volume and critical state friction angles only reduces the analytical prediction by as much as 10% since the change in friction angle magnitude was not great for the given test conditions. Furthermore, the measured post-cyclic shaft resistances reduced by as much as 61%, which resulted in some analytical predictions dangerously over predicting the measured value of the post-cyclic state. Table 7.3 gives the predicted to measured ratios of the pile shaft capacities over the three friction angle states described for chosen analytical methods.

Poulos and Chan (1986) stated that the shaft resistance should be expected to degrade to about 50% of the initial static value. Eigenbrod (1998) observed shaft resistance

Table 7.3 Predicted to measured shaft capacity ratios.

ϕ	δ	Earth Pressure Coefficient K		Q_s (tension) Pred./Measured	Q_s (comp.) Pred./Measured	***Q_s (comp.) Pred./Measured
Cycle 1		*CFEM	0.62	0.44	0.28	N/A
		API RP2A, 14th ed.	0.70	0.50	0.32	N/A
ϕ_{max}	δ_{max}	API RP2A, 15th ed.	0.80	0.57	0.36	N/A
43.8°	22°	Craig (1997)	**1.5	1.07	0.68	N/A
			2	1.42	0.91	N/A
Cycle 20		*CFEM	0.78	1.35	0.51	1.1
		API RP2A, 14th ed.	0.7	N/A	0.46	1
ϕ_{cs}	δ_{cv}	API RP2A, 15th ed.	0.8	1.38	0.52	1.1
37.4°	21° (comp.)	Craig (1997)	**1.5	2.59	0.98	2.1
			2	3.46	1.30	2.9
		*CFEM	0.78	1.21	0.46	1
ϕ_{cs}	δ_{cv}	API RP2A 14th ed.	0.5	0.78	N/A	N/A
37.4°	19° (tension)	API RP2A 15th ed.	0.8	1.24	0.47	1
		Craig (1997)	**1.5	2.33	0.88	1.9
			2	3.10	1.17	2.6

* Canadian Foundation Engineering Manual, 3rd Edition (1992).

** Estimated reduction of Craig's coefficient to accommodate for medium-dense sand.

*** Using measured compressive shaft resistance at displacement < 10% pile dia.

degradation as high as 55% whereas the experimental data from the centrifuge model piles experienced shaft degradation rates upwards of 61% from the first to the 20th load cycle. The analytical procedures presented are designed to predict the initial static value and not permit a cyclic displacement event such as the test series to occur. Therefore, comparison of the recorded loads from load cycle 1 reveals that only Craig over-predicts

the initial static value whereas the others give safe or conservative estimates of varying degrees.

In Table 7.4 the predictions according to Alawneh and Kraft are summarized, based on recommended δ and K values applied to Equation (2.2), and compared with the measured pre-cyclic test data.

Table 7.4 Shaft capacity prediction and comparison to measured pre-cyclic test data.

ϕ_{cs}	δ	K	Q_s (kN)	Q_s tension Pred./Measured	Q_s comp Pred./Measured
37.4°	ϕ_{cs} - 4°	0.90	6200	1.05	0.67 *[2.2]*
37.4°	$0.7\phi_{cs}$	0.90	4600	0.73	0.50 *[1.6]*

[ ] Using measured compressive shaft resistance at displacement < 10% pile dia.

The predictions in Table 7.4 are less conservative than the predictions by API and The Canadian Foundation Engineering Manual. By only changing the interface friction angle from the measured value to ϕ_{cs} - 4°, the predictions increase by as much as 48% and can alter an originally conservative estimate to one exceeding the measured capacity.

7.2 Prediction by CPT

Because the CPT is similar to piles, many attempts were made to estimate pile capacity with CPT data. Craig (1997) suggests that the average shaft stress $f_s = \bar{q}_c/200$ for piles in sand where $\bar{q}_c$ is the average cone tip resistance over the embedded length of the pile. Meyerhof (1983) estimates the average shaft stress $f_s = 0.005 q_{ca}$ where q_{ca} is the average

CPT tip resistance in a zone $4b$ above and $1b$ below the pile tip. The design procedures to predict pile shaft resistance with CPT q_c data is described in more detail in Section 2.1.2. In Table 7.5 the shaft resistance predictions using Craig (1997) and Meyerhof (1983) methods are compared with the pre-cyclic centrifuge model pile test data.

Table 7.5 Shaft capacity prediction with CPT q_c compared to pre-cyclic test data at prototype scale.

Series	Set	Q_s (T) (kN)	Q_s (C) (kN)	Craig (1997) (kN)	Meyerhof (1983) (kN)	Craig measured (T)	Craig measured (C)	Meyerhof measured (T)	Meyerhof measured (C)
Pile 1B	Pile 1B-3	5300	6700	5900	7100	1.1	0.9	1.3	1.1
Pile 2A	Pile 2A-3	5800	11700	8000	10900	1.4	0.7	1.9	0.9
Pile 2B	Pile 2B-3	5800	10400	6600	9700	1.1	0.6	1.7	0.9
Pile 3A	Pile 3A-3	6300	9300	7500	10800	1.2	0.8	1.7	1.2
					Average	**1.2**	**0.75**	**1.65**	**1.03**

Both Craig and Meyerhof overestimated the shaft resistance in the tensile loading direction by 20 and 65%, respectively. Craig was slightly more conservative than Meyerhof and yielded an average predicted to measured ratio of compressive shaft resistance of 0.75, while Meyerhof's methodology was more advantageous and predicted very accurate compressive shaft resistances that yielded an average predicted to measured ratio of 1.03. The over prediction of tensile shaft resistances reveals a lack of versatility of the reviewed design procedures. The CPT is a compressive loading test, thus fits with compressive pile loads and does not represent the tensile condition. It should be

remembered that the stress distribution around the tapered cone tip differs from the closed end piles tested. The full displacement-type piles tested within this modelling study have revealed tensile shaft resistances much lower than the compressive shaft capacity. This is not a unique case for many geotechnical modelers and researchers have reported such observations for both full and low displacement-type steel piles.

7.3 Theories and Observations

The pile models tested were closed end and therefore are classed as a full displacement-type pile. The displacement-type pile displaces a significant amount of material during pile installation and compressive failure. Furthermore, the portion of the total pile capacity carried by end bearing during compressive loading is significant and appears to have an influence on the shaft resistance. Centrifuge pile model test data revealed this influence of end bearing on shaft resistance, as presented in Section 6.3. The tensile shaft resistance is shown to reach the peak resistance for the given cycle at a very small displacement. When the tensile load cycle is complete and a compressive load is applied, the compressive shaft resistance is approximately equal to the tensile capacity until a compressive displacement of at least 5% of a pile diameter is achieved. At this point the end bearing is starting to pick up load and carry a significant portion of the total load, while the shaft resistance stays almost constant (Figure 7.1). At a certain point while the end bearing is increasing (in Figure 7.1 @ end bearing of 8 kN), the compressive shaft resistance picks up load again and increases to as much as 2 to 3 times of the corresponding tensile resistance. At this point a significant amount of compressive

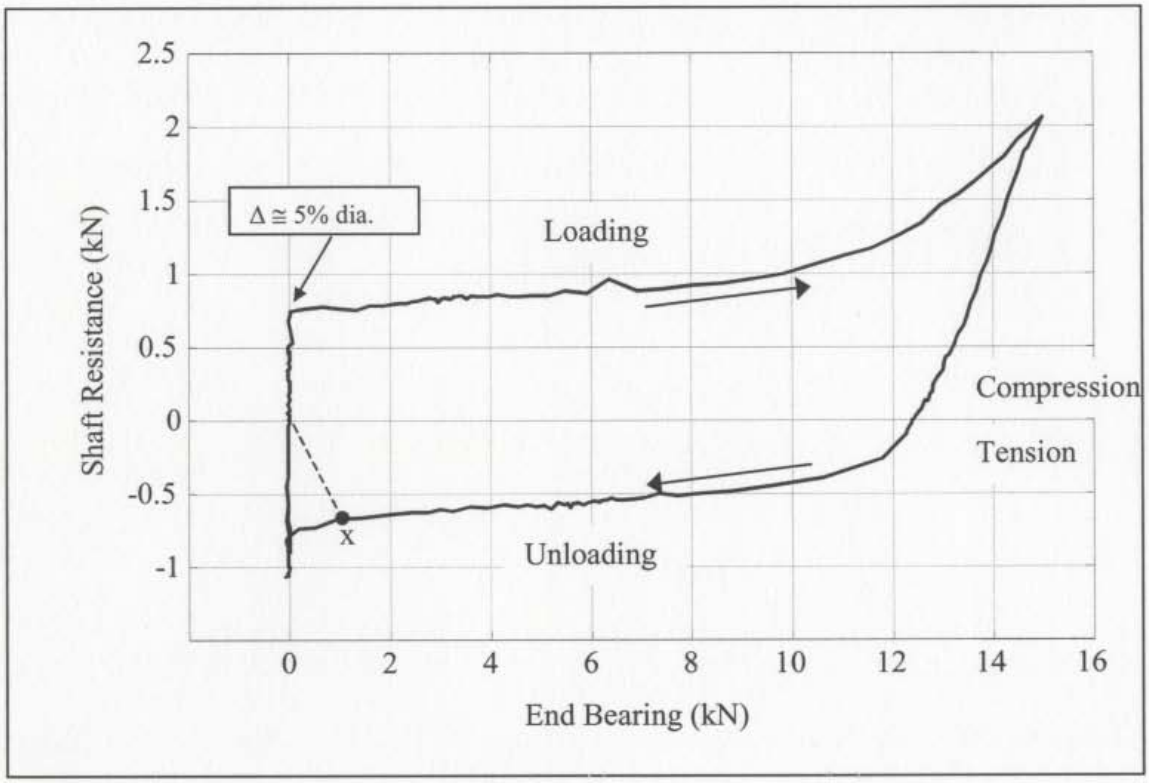

Figure 7.1 Relationship between end bearing and shaft resistance (Pile 2A-2, load cycle 2).

displacement has occurred prior to the increase in shaft resistance, as much as 10% of a pile diameter. This deformation is considered to be the point of failure by API RP2A and Terzaghi. Figures 6.7 and 6.9 reveal the cyclic displacements required for the described phenomena.

Figure 7.1 reveals the presence of a locked-in end bearing stress. Upon removing the axial compressive load, the sum of the shaft resistance and end bearing must therefore equal zero. A residual end bearing load may be seen simultaneously with a negative or

tensile pile shaft resistance (point x) of about 0.7 kN. This is thought to be due to the elastic rebound or resilience of the end bearing soil. The same resilient behaviour of end bearing soil has been observed and reported by researchers in the past. The development of an end bearing induced pressure bulb near the pile toe as described in Section 2.1.1 is suspected to be responsible for the increase in shaft resistance at this point. Significant compressive displacement is experienced prior to the increase in compressive shaft resistance, therefore soil dilation at the shear interface resulting in a net increase of shaft stress is not suspected as the influencing factor to cause such behaviour.

Eigenbrod (1998) investigated tensile and compressive shaft resistances of steel pipe piles at shallow depth. The test series involved pile load reversals to full failure in sand but with the end bearing removed. The pile was jacked into place and once the pile was at the design depth a cavity was created at the pile toe to eliminate the end bearing and isolate the shaft resistance. The compressive shaft resistance was somewhat greater than the tensile capacity, but with the absence of active end bearing, the compressive shaft response shown in Figures 6.7 and 6.9 did not materialize. The compressive shaft resistance responded much like the tensile resistance and did not increase further after a given displacement as in the case of the centrifuge pile models where end bearing was mobilized.

After the initial reduction in pile resistance from the first few load cycles, an increase in the total compressive pile resistance was noticed after about the tenth load reversal. This

is thought to be due to particle crushing and material densification at the zone of end bearing. As shown in Figure 7.2, the end bearing is shown to increase after about the sixth load reversal and slowly increases with continuous cycling. Due to the dry soil conditions and the material's workability in this state, material is thought to have continuously sloughed into the zone of end bearing during tensile displacements. Therefore, compressive loading would repeatedly compress and densify this material and result in an increase in bearing capacity. Furthermore, there is the possibility of sand particle crushing under the large end bearing stresses that would further densify the end bearing sand. Subsequently, the maximum compressive shaft resistance of each load cycle follows the same trend as the end bearing whereas the tensile shaft resistance shows no such end bearing interaction. This points to the apparent relation of end bearing to compressive shaft resistance, that once the pile is installed the magnitude of end bearing has a direct affect on compressive shaft stress. Observing the load resistance trend of the compressive shaft resistance taken at a compressive pile displacement less than 10% of a pile diameter further substantiates this claim. During a compressive loading stage and prior to the activation of end bearing, the compressive shaft resistance reaches a steady value, as shown in Figures 6.7, 6.9 and 6.11, which steadily decreases with increasing load cycles. The trend is very much like that of the tensile shaft resistance due to the absence of a large end bearing load at that stage of the load cycle.

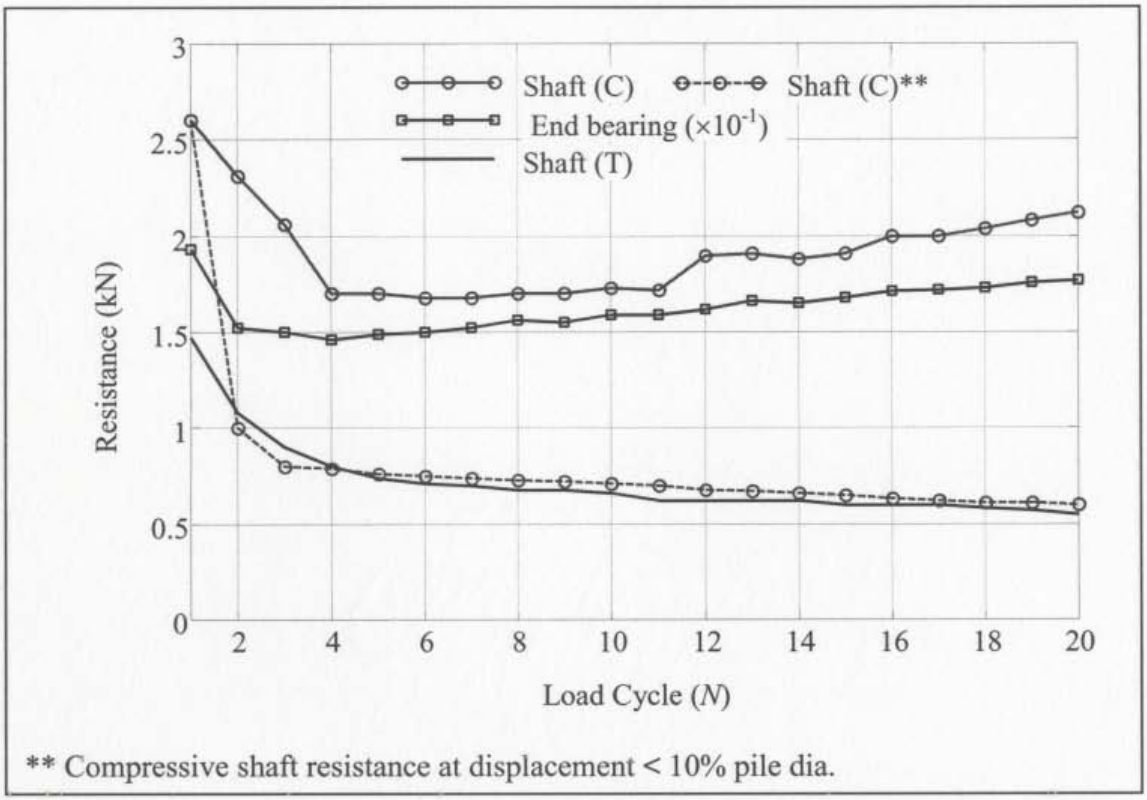

Figure 7.2 End bearing and shaft resistance with increasing load cycles (Pile 2A- 2).

CHAPTER 8

Conclusions and Recommendations

8.1 Conclusions

The objective of this study was to investigate the mechanisms involved with pile shaft resistance in a cohesionless soil and their response to continuous load reversals. A total of 15 centrifuge model tests were performed at three different scales. Furthermore, to compliment the centrifuge modelling study, a total of eight standard direct shear interface tests were performed. The tests were designed to investigate the following issues: Firstly, to determine the rate and magnitude of shaft resistance degradation with respect to load reversals. Secondly, assess the influence of pile end bearing on compressive shaft resistance. Thirdly, make qualitative comments on interface frictional behaviour by obtaining a quantitative measure of particle crushing and orientation at the sand-pile interface. Finally, prove the model design performance through test repeatability and modelling of models.

Axial load tests were performed on three geometrically similar closed end pipe pile models. The test regime emphasized the modelling technique termed *modelling of models*, therefore all three pile models of different scales corresponded to a single hypothetical full-scale prototype and were tested within centrifugal conditions in

accordance with the theoretically based scaling laws. If models of different scales predict the same hypothetical prototype, then this will provide a limited validation of the modelling data between the scales modelled and permits a cautious extrapolation of model output to the full-scale condition.

The application of modelling of models applied to the pile test data from this study does reveal a pattern of model prediction in accordance with the intent of the technique. A single hypothetical full-scale prototype was modelled with very close tolerance of pile end bearing and tensile shaft resistance; some variance of test data was present for the compressive shaft resistance phase of testing. Despite the variance of compressive shaft resistances between test series of different model scales, uniform rates and magnitudes of compressive shaft resistance degradation with cyclic loading was identified. In addition, the rates and magnitudes of tensile shaft resistance degradation with cyclic loading between the three models was uniform with only a $\pm 0.75\%$ difference after completion of 40 load reversals. On average, about 38% of the initial tensile shaft resistance was lost after the first three load cycles, and about 12% in the compressive loading direction. After the tenth load cycle, about 90% of the total observed shaft friction degradation had occurred for both loading directions. The observed rates and magnitudes of frictional degradation are in accordance with model and field studies reported by researchers.

The model piles tested were closed end and therefore model a full displacement-type prototype pile. Full displacement-type piles displace a significant amount of material and

a large portion of the total resistance is due to end bearing. A continuous record of shaft and end bearing resistances, with respect to axial displacement and time, was obtained for each of the model tests. A distinct relation between shaft resistance and end bearing was uncovered. The observed compressive shaft resistances were approximately equal to the tensile shaft resistances before the end bearing was mobilized. Beyond this point the compressive shaft resistance increased to values of two to three times that of the corresponding tensile capacity. The increase in compressive shaft resistance was observed to be proportional to the increase in end bearing capacity. Prior to the onset of influence from the increasing end bearing, compressive displacements were up to 8% to 10% of a pile diameter. These displacements are indicative of a full failure state prior to the end bearing related increase of shaft resistance. Therefore, the change in compressive shaft resistance is not due to dilative soil strain at the sand-pile interface but is due to end bearing and the mobilization of a stress bulb around the lower extremities of the pile shaft. Many researchers have hypothesized the presence of a stress bulb or failure surface from compressive loading of a displacement-type pile. The boundary of the failure surface is considered to be a function of pile diameter and the material internal angle of friction and may extend upward around the pile by as much as nine pile diameters. Since the lengths of the pile models are only 7.5 diameters, the effect of the end bearing induced pressure bulb on compressive shaft friction is significant. Theoretical predictions of pile performance often do not differentiate between the compressive and tensile shaft resistance. The modelling study has revealed not only a very distinct difference in capacity but also a difference in load transfer mechanisms, due to the end bearing effects.

Therefore, theoretical design procedures for displacement-type piles that do not differentiate tensile from compressive shaft resistance will yield overly conservative compressive capacity predictions if the tensile resistance is not to be overestimated.

The modelling soil chosen for the study was fine silica sand with a mean particle size of 0.32 mm. The sand particles are bulky in shape and are not prone to orientation with directional shearing. Post-test examination of the model sand bed revealed particle crushing within the areas of CPT and pile testing. Determination of the interface friction angle with a standard direct shear interface test did not reveal sand particle crushing to any extent at the interface, although the normal stresses applied did match the expected normal stresses acting along the pile model shaft. The particle crushing can then be attributed to the high end bearing stresses experienced from the pile jacking process and compressive cyclic axial loading. Therefore, determination of the interface friction angle with a standard direct shear interface test will yield a conservative value since the interface friction angle is known to increase with decreasing mean particle size. Conversely, particle crushing may result in a net volumetric compression that would lead to a reduction in the lateral confining stress. This is important as the predictions of shaft friction are based on both the effective horizontal stress and the tangent of the interface friction angle. An attempt was made to quantify the degree of particle crushing within the soil model. A true measure of particle crushing was never obtained even though it could be visually identified.

8.2 Recommendations

A large portion of the study consisted of design and development of the experimental equipment. Even though the test regime was limited, it provided insight into the pile load transferring mechanisms. The study also gave valuable information on limitations of the existing design and how it could be improved to give additional information on pile behaviour. Limitations of the current test design have been described throughout the previous chapters and include such limitations as the possible boundary effects of more than one test execution per sand model and instrumentation error due to stress field variance, among other possible sources.

The test data obtained from this modelling study strongly suggest that an interaction exists between compressive shaft resistance and end bearing. Moreover, the compressive shaft resistance was as much as three times that of the corresponding tensile resistance. Some theoretical design procedures do not differentiate between compressive and tensile shaft resistances, nor do they directly accommodate the end bearing interaction with shaft resistances. For full displacement-type piles, it is abundantly clear that both the initial static and post-cyclic compressive shaft resistances are much greater than the corresponding tensile resistances. For the given conditions, if the tensile shaft resistances are assumed to be equal to the compressive shaft capacity, a very dangerous overestimation may result.

An end bearing induced pressure bulb is thought to be the cause for the differences in shaft resistance. In order to substantiate this claim, further testing is required. The implementation of a fully instrumented (strain gauged) pile in the current configuration may yield the axial shaft stress profile with depth over the load cycles. Furthermore, strain gauges could also measure the radial stresses acting on the pile shaft. A point of interest would be the portion of the compressive load cycle when the end bearing is first mobilizing and the onset of end bearing influence on shaft resistance is first initiated. It is hypothesized that this would reveal a distinct change in the both compressive shaft stress profile and the radial stresses with the propagation of an end bearing induced pressure bulb.

To further substantiate the influence of end bearing on compressive shaft resistance, testing of geometrically similar open ended pile models could be implemented. An open ended pipe pile jacked into dry sand, such as the modelling sand of this study, may not plug since the models are relatively short and wide. If the pile does not plug, then it may be thought of as a low displacement-type pile and may have a proportionately smaller end bearing capacity. It is suspected that the end bearing effects would be minimized. The lower degree of displacement would also influence the tensile shaft resistance but it is hypothesized that the ratio of tensile to compressive shaft resistance would be much closer to 1 than for the full displacement-type pile. To prove further the existence of an end bearing induced pressure bulb; a more advantageous test design would see the direct isolation of the shaft capacity by complete elimination of the end bearing component. Not

representative of *in-situ* conditions, such tests have been carried out on 1*g* models to analyze pile shaft interface behaviour but not at the high stress levels within a centrifuge. The absence of end bearing would completely change the pile soil interaction from the existing design, but it is believed that with the absence of end bearing that the compressive shaft resistances would be very close to the tensile resistances.

The modelling of models technique was applied to this study with favorable results. Continuation of this study and application of the aforementioned modelling recommendations should be done over a larger scale range. This would enhance the confidence of model data extrapolation to the full-scale prototype condition if the modelling of models technique proved successful. Further development of the test parameters could include investigations in different sand gradations, mineral compositions and pile shaft roughness. Using a rough pile surface will obviously increase the magnitude of shaft resistance and therefore yield a stronger strain gauge signal response from a fully instrumented pile. Furthermore, to increase the confidence and accuracy of the applied instrumentation, addition of a third load cell to measure shaft resistance directly is recommended. A cylindrical load cell placed beneath the pile head to directly measure the shaft resistance would then make the procedure of back calculating the shaft resistance from the combination of total and end bearing resistances redundant.

Having used two different pile head fixities, a significant influence of pile batter on shaft resistance was observed. Since the loading system and instrumentation was not designed for pile inclination, the inclined effect was not desired but the compressive shaft resistance was observed to increase significantly at small pile inclinations. Due to the load cell design for the current program, the recorded loads are suspect but do raise questions on the effects of pile batter on shaft resistances. With proper model design, further evaluation of pile shaft resistance of a single battered pipe pile may be an area for future modelling studies.

It is suggested that a research program be conducted to examine the end bearing influence on compressive shaft resistance. The effects of pile displacement-type on shaft resistance, once revealed could refine the common theoretical design procedures.

References

Airey, D.W., Al-Douri, R.H. and Poulos, H.G. (1992). "Estimation of Pile Friction Degradation from Shearbox Tests" *Geotechnical Testing Journal*, ASCE, Vol. 15, No. 4, pp. 388-393.

Alarcon-Guzman, A., Leonards, G. and Chameau, J. (1988). "Undrained Monotonic and Cyclic Strength of Sands" *J. Geotech. Engrg.*, ASCE, Vol. 114, No. 9, pp. 1089-1109.

Alawneh, A.S. (1999). "Tension Piles in Sand, A Method Including Degradation of Shaft Friction During Pile Driving" *Transportation Research Record 1663*, Soils, Geology and Foundations, National Research Council, National Academy Press, Washington DC, (99-0092), pp.41-49.

Alawneh, A.S., Malkawi, A.I.H. and Al-Deeky, H. (1998). "Tension Tests on Smooth and Rough Model Piles in Dry Sand" *Canadian Geotechnical Journal*, Vol. 36, No. 4, pp. 746-753.

American Petroleum Institute (1984), *Recommended Practice for Planning, Designing and Constructing Fixed Offshore Platforms*, 15th Edition, Washington, D.C.

Association de Recherche en Géotechnique Marine (ARGEMA), (1992), *Design Guides For Offshore Structures*. (ed Le-Tirant, P.), Technip, Paris, France, 291p.

Been, K., Jefferies, M.G., Crooks, J.H.A. and Rothenburg, L. (1987). "The Cone Penetration Test in Sands: Part II, General Influence of State" *Géotechnique*, Vol. 37, No. 3, pp. 285-299.

Bolton, M.D. (1986). "The Strength and Dilatancy of Sands" *Géotechnique*, Vol. 36, No. 1, pp. 65-78.

Bolton, M.D. and Lau, C.K. (1988). "Scale Effect Arising From Particle Size" *Centrifuge '88*, Balkema, Rotterdam, pp. 127-134.

Bolton, M.D. and Lau, C.K. (1989). "Scale Effects in the Bearing Capacity of Granular Soils" *Proc. 11th Int. Conf. Soil Mech. Found. Engng.*, Rio De Janeiro Vol. 2, pp. 895-898.

Bolton, M.D., Gui, M.W., Garnier, J., Corte, J.F., Bagge, G., Laue, J. and Renzi, R. (1999). "Centrifuge Cone Penetration Tests in Sand" *Géotechnique*, Vol. 49, No. 4, pp. 543-552.

Boulon, M. and Nova, R. (1990). "Modelling of Soil-Structure Interface Behaviour, A Comparison Between Elastoplastic and Rate Type Laws" *Computers and Geotechnics*, Vol. 9, No. 1, pp. 21-46.

Bowles, J.E. (1992). *Engineering Properties of Soils and Their Measurement*, 4th Edition, McGraw Hill, NJ, 241p.

Bozozuk, M. (1972). "Downdrag Measurements on a 160-Ft Floating Pipe Test in Marine Clay" *Canadian Geotechnical Journal*, Vol. 9, No. 2, pp. 127-136.

Canadian Foundation Engineering Manual (1992), 3rd Edition, Canadian Geotechnical Society, Technical Committee on Foundations, 512p.

Craig, R.F. (1997), *Soil Mechanics*, 6th Edition, E & FN Spon, London, 485p.

Culligan-Hensley, P.J. and Savvidou, C. (1995). "Environmental Geomechanics and Transport Mechanisms" *Geotechnical Centrifuge Modelling*, (ed. Taylor, R.N.), Blackie Academic & Professional, London, pp. 196-263.

De Beer, E.E., (1963). "The Scale Effect in the Transportation of the Results of Deep-Sounding Tests on the Ultimate Bearing Capacity of Piles and Caisson Foundations" *Géotechnique*, Vol. XIII, pp. 39-75.

De Nicola, A. and Randolph, M.F. (1993). "Tensile and Compressive Shaft Capacity of Piles in Sand" *J. Geotech. Engrg.*, ASCE, Vol. 119, No. 12, pp. 1952-1973.

Eigenbrod, K.D. and Issigonis, T. (1996). "Pore-water Pressures in Soft to Firm Clay During Driving of Piles into Underlying Dense Sand" *Canadian Geotechnical Journal*, Vol. 33, No. 2, pp. 209-218.

Eigenbrod, K.D. (1998). "Capacity of Steel Piles in Silty Soils Under Repeated Loading" *Proc. 51st Can. Geotech. Conf.*, Edmonton, Vol. 2, pp. 359-365.

Eslami, A. and Fellenius, B.H. (1997). "Pile Capacity by Direct CPT and CPTu Methods Applied to 102 Case Histories" *Canadian Geotechnical Journal*, Vol. 34, No. 6, pp. 886-904.

Evgin, E. and Fakharian, K. (1996). "Effect of Stress Paths on the Behaviour of Sand-Steel Interface" *Canadian Geotechnical Journal*, Vol. 33, No. 6, pp. 853-865.

Foundations and Earth Structure Design Manual 7.2 (1982), NAVFAC DM-7.2, Department of the Navy, Alexandria, VA.

Gemperline, M.C. (1988). "Coupled Effects of Common Variables on the Behaviour of Shallow Foundations in Cohesionless Soils" *Centrifuge '88*, Balkema, Rotterdam, pp. 285-292.

Hanke, R. (2001). "Pile Model Test Data" *CD-ROM*, C-CORE, Memorial University of Newfoundland, St. John's.

Horvitz, G.E., Stettler, A.M. and Crowser, M. (1981). "Comparison of Predicted and Observed Pile Capacity" *Cone Penetration Testing and Experience*, (ed. G.M. Norris and R.D. Holtz), ASCE, pp. 413-433.

Ireland, H.O. (1957). "Pulling Tests on Piles in Sand" *Proc. 4th Inter. Conf. on Soil Mechanics and Foundation Engineering*, London, pp. 43-46.

Jardine, R.J., Overy, R.F. and Chow, F.C. (1998). "Axial Capacity of Offshore Piles in Dense North Sea Sands" *Journal of Geotech. and Geoenviro. Engrg.*, ASCE, Vol. 124, No. 2, pp. 171-178.

Johannessen, I.J. and Bjerrum, L. (1965). "Measurement of the Compression of Steel Pipe Pile to Rock Due to Settlement of the Surrounding Clay" *Proc. 6th Int. Conf. Soil Mech. Found. Eng.*, Montreal, University of Toronto Press, Toronto, 2, pp. 261-264.

Ketcham, S.A. and Black, P.B. (1995). "Initial Results From Small-Scale Frost Heave Experiments in a Centrifuge" *CRREL Report 95-9*, U.S. Army Cold Regions Research and Engineering Laboratory, Hanover, N.H., 18p.

Ketcham, S.A., Black, P. and Pretto, R. (1997). "Frost Heave Loading of Constrained Footing by Centrifuge Modelling" *J. Geotech. Engrg.*, ASCE, Vol. 123, No. 9, pp. 874-881.

Kezdi, A. (1964), *Bodenmechanik*, Vol. 2, Verlag fur Bauwesen, Berlin.

Kishida, H. and Uesugi, M. (1987). "Tests of the Interface between Sand and Steel in Simple Shear Apparatus" *Géotechnique*, Vol. 37, No. 1, pp.45-52.

Ko, H.Y. (1988). "Summary of the State-Of-The-Art in Centrifuge Model Testing" *Centrifuges in Soil Mechanics*, (eds. H.Y. Ko, R.G. James and A.N. Schofield), Balkema Rotterdam, pp. 11-18.

Kraft, L.M., Jr. (1990). "Computing Axial Pile Capacity in Sands for Offshore Conditions" *Marine Geotechnology*, Vol. 9, No. 1, pp. 61-92.

Kraft, L.M., Jr. (1991). "Performance of Axially Loaded Pipe Piles in Sand" *J. Geotech. Engrg.*, ASCE, Vol. 117, No. 2, pp. 272-296.

Kulhway, F.H. (1984). "Limiting Tip and Side Resistance: Fact or Fallacy?" *Proc. Analysis and Design of Pile Foundations*, ASCE, pp. 80-98.

Latotzke, J., König, D. and Jessberger, H.L. (1998). "Axial Pile Load Tests with Reaction Beams" *Centrifuge '98*, Balkema, Rotterdam, pp. 485-490.

Lee, C.Y. and Poulos, H.G. (1987). "Jacked Model Pile Shafts in Offshore Calcareous Soils" *Marine Geotechnology*, Vol. 7, No. 4, pp. 247-274.

Lehane, B.M. and Jardine, R.J. (1994). "Shaft Capacity of Driven Piles in Sand: A New Design Approach" *Proc. Conf. Behaviour of Offshore Struct. (BOSS)*, Boston, Mass., pp. 23-36.

Lemos, L.J. and Vaughan, P.R. (2000). "Clay-Interface Shear Resistance" *Géotechnique*, Vol. 50, No. 1, pp. 55-64.

Meyerhof, G.G. (1951). "The Ultimate Bearing Capacity of Foundations" *Géotechnique*, Vol. 2, No. 4, pp. 301-332.

Meyerhof, G.G. (1983). "Scale Effects of Ultimate Pile Capacity" *J. Geotech. Engrg.*, ASCE, Vol. 109, No. 6, pp. 797-806.

Murff, J.D. (1997). "The Geotechnical Centrifuge in Offshore Engineering" *Offshore Technology Conference*, Vol. 1, OTC 8265, pp. 1-15.

Orman, M.E. (1994). "Interface Shear-strength Properties of Roughened HDPE" *J. Geotech. Engrg.*, ASCE, Vol. 120, No. 4, pp. 758-761.

Parkin, A. and Lunne, T. (1982). "Boundary Effects in the Laboratory Calibration of a Cone Penetrometer in Sand" *Proc. 2nd Eur. Symp. Penetration Testing*, Amsterdam, Vol. 2, pp. 761-768.

Paulin, M.J. (1998), *An Investigation into Pipelines Subjected to Lateral Soil Loading*, Ph.D. Thesis, Memorial University of Newfoundland, St. Johns, Canada, 413p.

Phillips, R., Clark, J.I., Paulin, M.J., Meaney, R., Millan, D. and Tuff, K. (1994). "Canadian National Centrifuge Centre with Cold Regions Capabilities" *Centrifuge '94*, Balkema, Rotterdam, pp. 57-62.

Phillips, R. (1995). "Centrifuge Modelling: Practical Considerations" *Geotechnical Centrifuge Modelling*, (ed. Taylor, R.N.), Blackie Academic & Professional, London, pp. 34-60.

Phillips, R., Clark, J.I., Zhu, F. and Hanke, R. (2000). "Laterally Loaded Free Head Pile Test Comparison in Layered Soil" *Proc. 53rd Can. Geotechnical Conf, Montreal*, Vol. 2, pp. 961-965.

Poulos, H.G. and Davis, E.H. (1980). *Pile Foundation Analysis and Design*. John Wiley and Sons, New York, 397p.

Poulos, H.G. (1988), *Marine Geotechnics*. Unwin Hyman Limited, London, 473p.

Poulos, H.G. and Chan, F.K. (1986). "Model Pile Skin Friction in Calcareous Sand" *Geotechnical Engrg.*, Vol. 17, No. 2, pp. 235-257.

Rao, S.N. and Krishnamurthy, N.R. (1982). "Studies of Negative Skin Friction in Model Piles" *Geotechnical Engrg.*, Vol. 32, pp. 83-91.

Rezende, M.E.B., Garnier, J., Rault, G. and Cintra, J.C.A. (1998). "Effect of Shaft Friction Developed by Centrifuge Acceleration on Pile Loading Tests Results" *Centrifuge '98*, Balkema, Rotterdam, pp. 501-506.

Santamarina, J.C. and Goodings, D.J. (1989). "Centrifuge Modeling: A Study of Similarity" *Geotechnical Testing Journal*, ASCE, Vol. 12, No. 2, pp. 163-166.

Schofield, A.N. (1980). "Cambridge Geotechnical Centrifuge Operations" *Géotechnique*, Vol. 30, No. 3, pp. 224-268.

Sharp, M. K., Dobry, R. and Phillips, R. (1998). "Cone Penetration Modeling in Sand for Evaluation of Earthquake-Induced Lateral Spreading" *Centrifuge '98*, Balkema, Rotterdam, pp. 161-166.

Smith, C.C. (1995). "Cold Regions' Engineering" *Geotechnical Centrifuge Modelling*, (ed. Taylor, R.N.), Blackie Academic & Professional, London, pp. 264-292.

Steedman, R.S. and Zeng, X. (1995). "Dynamics" *Geotechnical Centrifuge Modelling*, (ed. Taylor, R.N.), Blackie Academic & Professional, London, pp. 168-195.

Swinianski, J. and Sawicki, A. (1991). "A Model of Soil-Pile Interaction Owing to Cyclic Loading" *Canadian Geotechnical Journal*, Vol. 28, No. 1, pp. 11-19.

Symes, M.J., Gens, A. and Hight, D.W. (1984). "Undrained Anistrophy and Principal Stress Rotation in Saturated Sand" *Géotechnique*, Vol. 34, No. 1, pp. 11-27.

Tabucanon, I.J., Airey, D.W. and Poulos, H.G. (1995). "Pile Skin Friction in Sands from Constant Normal Stiffness Tests" *Geotechnical Testing Journal*, ASCE, Vol. 18, No. 3, pp. 350-364.

Taylor, R.N. (1995). "Centrifuges in Modelling: Principles and Scale Effects" *Geotechnical Centrifuge Technology*, (ed. Taylor, R.N.), Blackie Academic & Professional, London, pp. 19-33.

Terzaghi, K. and Peck, R.B. (1967), *Soil Mechanics in Engineering Practice*. John Wiley and Sons, New York, 729p.

Terzaghi, K., Peck, R.B. and Mesri, G. (1996), *Soil Mechanics in Engineering Practice, 3rd Edition*. John Wiley and Sons, New York, 549p.

Tomlinson, M.J. (1995), *Foundation Design and Construction, 6th Edition*. New York, John Wiley and Sons, 536p.

Toolan, F.E., Lings, M.L. and Mirza, U.A. (1990). "An Appraisal of API RP2A Recommendations for Determining Skin Friction of Piles in Sand" *Offshore Technology Conference*, Vol. 4, OTC 6422, pp. 33-42.

Turner, J.P. and Kulhawy, F.H. (1992). "Strength Changes in Sand Following Cyclic Shear" *Geotechnical Testing Journal*, ASCE, Vol. 15, No. 3, pp. 295-299.

Turner, J.P. and Kulhawy, F.H. (1994). "Physical Modelling of Drilled Shaft Side Resistance in Sand" *Geotechnical Testing Journal*, ASCE, Vol. 17, No. 3, pp. 282-290.

Uesugi, M., Kishida, H. and Tsubakihara, Y. (1989). "Friction Between Sand and Steel Under Repeated Loading" *Soils and Foundations*, Vol. 29, No. 3, pp. 127-137.

Vesić, A.S. (1967). "Ultimate Loads and Settlements of Deep Foundations in Sand" *Bearing Capacity and Settlement of Foundations*, (ed. Vesić, A.S), Duke University, Durham, North Carolina, 150p.

Zhu, F. (1998), *Centrifuge Modelling and Numerical Analysis of Bearing Capacity of Ring Foundations*, Ph.D. Thesis, Memorial University of Newfoundland, St. Johns, Canada, 219p.